

**LANTHANUM COMPLEXES AS THERAPEUTIC AGENTS FOR THE TREATMENT
OF BONE RESORPTION DISORDERS**

by

David Michael Weekes

M.Chem. (Hons.), The University of Newcastle Upon Tyne, 2011

A THESIS SUBMITTED IN PARTIAL FULFILLMENT OF
THE REQUIREMENTS FOR THE DEGREE OF

DOCTOR OF PHILOSOPHY

in

THE FACULTY OF GRADUATE AND POSTDOCTORAL STUDIES
(Chemistry)

THE UNIVERSITY OF BRITISH COLUMBIA
(Vancouver)

July 2016

© David Michael Weekes, 2016

Abstract

Lanthanum naturally targets and binds skeletal tissue in living systems, wherein it has the potential to treat bone resorption disorders by invoking a biological response that counteracts an imbalanced bone remodeling cycle. Because lanthanum is very poorly absorbed, the key to realizing this potential is through rational chelator design, and in this regard, a number of lanthanum complexes have been designed, synthesized, and tested in an effort to develop an orally-active drug. Previously, past group members Dr. Cheri Barta and Dr. Yasmin Mawani had identified *tris*-(1,2-dimethyl-3-oxypyridin-4-one) lanthanum(III) (**La(dpp)₃**) and bis-[[bis(carboxymethyl)amino]methyl]phosphinate lanthanum(III) (**La(XT)**) as lead drug candidates, and – after tailoring the synthetic procedures to access large quantities of each – these compounds were tested for their thermodynamic and kinetic interactions with synthetic hydroxyapatite (HAP) by isothermal titration calorimetry (ITC) and solution depletion studies, respectively. The systems were also tested for the first time *in vivo* (healthy Sprague Dawley rats) by measuring lanthanum biodistribution from single-dose intravenous (IV), acute IV, and short-term IV and oral administration of either compound. Overall, it was found that La(XT) was a more viable candidate than La(dpp)₃, primarily due to higher thermodynamic stability which led to better oral uptake. Four new compounds (**H₂dpa**, **H₃cedpa**, **H₄pedpa**, and **H₇alenpa**) and three of their lanthanum complexes (all but H₇alenpa) were also synthesized, and tested for ligand binding kinetics with HAP (solution depletion studies), thermodynamic stability of the lanthanum complexes (potentiometric and NMR titrations), and lipophilicity of both the ligands and the metal complexes (partition coefficient measurements). It was found that [**La(pedpa)**]⁻ exhibited the most favourable overall profile for a potential drug candidate, but requires further testing before *in vivo* trials. Crystal structures for [La₄(pedpa)₄(H₂O)₂] and [La(dpp)₃(H₂O)₂]·11.75H₂O were also obtained.

Preface

Chapter 1 is an adaptation of published work, and is reproduced in part from D. M. Weekes and C. Orvig; Harnessing the bone-seeking ability of Ca(II)-like metal ions in the treatment of metastatic cancer and resorption disorders, *Chem. Soc. Rev.* **2016**, *45*, 2024-2031, Copyright 2016 The Royal Society of Chemistry. I was responsible for researching and writing the review article, with input and editing from Dr. Chris Orvig.

Some portions of **Chapter 2** and **Chapter 3** have been adapted from published work, and have been reproduced in part from J. F. Cawthray, D. M. Weekes, O. Sivak, A. L. Creagh, F. Ibrahim, M. Iafrate, C. A. Haynes, K. M. Wasan and C. Orvig; *In vivo* study and thermodynamic investigation of two lanthanum complexes, La(dpp)₃ and La(XT), for the treatment of bone resorption disorders, *Chem. Sci.* **2015**, *6*, 6439-6447, Copyright 2015 The Royal Society of Chemistry. The article was co-authored by myself and Dr. Jacqueline Cawthray, with input from Dr. Charles Haynes and Dr. Kishor Wasan, and input and editing from Dr. Chris Orvig. I was responsible for performing the scaled-up syntheses of La(dpp)₃ and La(XT). Isothermal titration calorimetry (ITC) experiments were carried out at the Michael Smith Laboratories (University of British Columbia). All solutions were made by myself, titrations and data processing were carried out by Dr. Louise Creagh, and the results interpreted with input from Dr. Louise Creagh, Dr. Charles Haynes, and Dr. Jacqueline Cawthray. I was responsible for the design and execution of the solution depletion studies, with assistance from Madeline Iafrate during her undergraduate placement in our group. All ICP-MS analyses throughout this thesis were carried out by me at the Pacific Centre for Isotopic and Geothermal Research (PCIGR), Earth and Ocean Sciences (EOS), UBC, under the supervision of Dr. Vivian Lai and Dr. Marghaleray Amini.

The animal studies presented in **Section 3.2.1** and **Sections 3.2.2** have been published in the above stated manuscript (*Chem. Sci.* 2015), and were carried out at the University of British Columbia. The protocols were approved by the UBC Animal Care and Use Program (ACUP) (approval certificate #A11-0135) and performed in accordance with the guidelines outlined by the Canadian Council on Animal Care (CCAC). All drug candidates used were synthesized by me. Pharmacokinetic data was collected and interpreted by Dr. Fady Ibrahim and Dr. Olena Sivak. The acute dosing regime was coordinated by Dr. Olena Sivak. Organ harvesting, homogenization, and preparation of ICP-MS analysis was carried out by myself, Dr. Jacqueline Cawthray, and Christina Chen (Biomaterials group, Faculty of Applied Science, UBC) under the direction of Dr. Sivak.

The animal studies presented in **Section 3.2.3** have not been published. These studies were carried out primarily at the University of Saskatchewan (U.Sask), and the protocols were approved by the University Animal Care Committee (UACC) Animal Research Ethics Board (approval certificate # 20150060) and performed in accordance with the guidelines outlined in by the CCAC. The short-term oral and IV studies were coordinated and executed by Dr. Jacqueline Cawthray. Drug candidates were synthesized by me, and formulations of $\text{La}(\text{dpp})_3$ were made by Dr. Ellen Wasan (U.Sask). Soft-tissue organs were harvested, homogenized, and prepared for ICP-MS under the direction of Dr. Cawthray, and sent to UBC for analysis, which was undertaken by me. Bones were harvested by Dr. Cawthray and sent to UBC, where I was responsible for cleaning and preparation for ICP-MS. All results were interpreted by myself and Dr. Cawthray, with input from Dr. Chris Orvig and Dr. Kishor Wasan. K-edge subtraction imaging was performed by Dr. Arash Panahifar at the Canadian Light Source (CLS, Saskatoon, SK).

The work presented in **Chapter 4** has not been published. The original H_2dpa ligand was first realized and characterized by Dr. Lisa Murphy as an unwanted side-product during the

synthesis of a different compound. I was responsible for deriving the rational synthesis of H₂dpa, as well as all other compounds and lanthanum complexes presented in Chapter 4. Two undergraduate students, Madeline Iafrate and Jay Chi, aided in optimizing the synthesis of H₄pedpa. All partition coefficient measurements and HAP kinetic binding studies were carried out by myself. All potentiometric titrations were carried out by Dr. Maria de Guadalupe Jaraquemada Peláez. The ¹H and ³¹P NMR titrations were carried out by myself and Dr. Peláez with assistance from Thomas Kostelinik, a graduate student in our group. Dr. Peláez performed the data fitting and obtained the stability constants and speciation diagrams. All solid-state X-ray structures were collected and solved by Dr. Brian Patrick. The project was supervised by Dr. Chris Orvig.

Table of Contents

Abstract.....	ii
Preface.....	iii
Table of Contents	vi
List of Tables	xi
List of Figures.....	xiii
List of Symbols and Abbreviations	xxi
List of Schemes	xxviii
List of Equations	xxix
Acknowledgements	xxx
Chapter 1: Introduction	1
1.1 Bone structure, function, and disease	1
1.2 Bone as a target for metal ions.....	2
1.3 Radiometals for metastatic bone cancer	5
1.3.1 Bone metastases	5
1.3.2 Samarium-153.....	6
1.3.3 Radium-223.....	8
1.3.4 Other radiometals.....	10
1.4 Treatments and therapies for osteoporosis.....	11
1.4.1 Osteoporosis.....	11
1.4.2 Prevention and treatment	12
1.4.3 Bisphosphonates	13
1.4.4 Strontium ranelate.....	15

1.5	Lanthanum compounds for osteoporosis	17
1.5.1	Lanthanum carbonate.....	17
1.5.2	A question of concentration.....	18
1.5.3	Increasing bioavailability.....	19
1.6	Thesis overview	21
Chapter 2: Thermodynamic and kinetic investigations into the interaction between two lead compounds – La(dpp)₃ and La(XT) – and hydroxyapatite.....		24
2.1	Introduction to previous work.....	24
2.1.1	Hydroxypyrones and hydroxypyridinones.....	24
2.1.2	La(XT): Towards higher denticity	26
2.2	Thermodynamic and kinetic studies with HAP	29
2.2.1	Isothermal titration calorimetry of La ³⁺ complexes with HAP.....	29
2.2.2	Solution depletion kinetics with La ³⁺ complexes and HAP.....	31
2.3	Results and discussion	32
2.3.1	Crystal structure of [La(dpp) ₃ (H ₂ O) ₂] • 11.75H ₂ O	32
2.3.2	ITC results and discussion	35
2.3.3	Results and discussion for solution depletion studies.....	41
2.4	Conclusion of HAP binding studies.....	45
2.5	Experimental.....	46
2.5.1	Synthesis of La(dpp) ₃ and La(XT).....	46
2.5.1.1	Materials and reagents for synthetic procedures.....	46
2.5.1.2	Instruments.....	46
2.5.1.3	Synthesis of La(dpp) ₃	47

2.5.1.4	Synthesis of La(XT).....	48
2.5.2	General experimental for HAP studies	50
2.5.2.1	Experimental for ITC.....	51
2.5.2.2	Experimental for solution depletion studies	51
Chapter 3: <i>In vivo</i> biodistribution of La(dpp)₃ and La(XT).....		53
3.1	Introduction.....	53
3.2	Results and discussion	54
3.2.1	Plasma clearance and soft-tissue distribution from single IV dose	54
3.2.2	Biodistribution from multiple IV doses	57
3.2.3	Biodistribution from short-term oral and IV doses.....	59
3.3	Elemental mapping of La ³⁺ in bone using K-edge subtraction imaging.....	65
3.4	Conclusions.....	67
3.5	Experimental.....	69
3.5.1	General experimental for <i>in vivo</i> studies	69
3.5.2	Drug preparation	69
3.5.3	Drug administration protocol.....	70
Chapter 4: Lanthanum complexes of dipicolinic acid (dpa)-ligands for the treatment of resorption disorders: Design, synthesis, and preliminary studies.....		72
4.1	Introduction and motivation.....	72
4.1.1	The “pa” family of ligands as acyclic chelators for radiometals	73
4.1.2	The H ₂ dpa scaffold	75
4.2	Results and discussion	77
4.2.1	Synthesis of the dpa ligands.....	77

4.2.2	Solution depletion studies of dpa ligands with HAP	82
4.2.3	La(III) complexes of the dpa ligands	87
4.2.3.1	Synthesis and characterization of the La(III)-dpa complexes.....	87
4.2.3.2	Crystal structure of [La ₄ (pedpa) ₄ (H ₂ O) ₂].....	89
4.2.4	Speciation plots and thermodynamic stability constants of La(dpa) and La(pedpa)	94
4.2.5	Lipophilicity measurements of dpa compounds and their lanthanum complexes ..	101
4.3	Conclusions.....	103
4.4	Experimental.....	104
4.4.1	Materials and reagents	104
4.4.2	Instruments.....	105
4.4.3	Synthesis of the dpa-containing compounds.....	106
4.4.3.1	Methyl 6-(bromomethyl) picolinate (3) (Scheme 4.1).....	106
4.4.3.2	6,6'-[Azanediylbis(methylene)] dipicolinic acid (H ₂ dpa) (Scheme 4.2).....	107
4.4.3.3	6,6'-{[(Carboxymethyl)azanediyl]bis(methylene)} dipicolinic acid (H ₃ cedpa) (Scheme 4.3)	109
4.4.3.4	6,6'-{[(2-Phosphonoethyl)azanediyl]bis(methylene)} dipicolinic acid (H ₄ pedpa) (Scheme 4.4)	110
4.4.3.5	6,6'-{[(4-Hydroxy-4,4-diphosphonobutyl)azanediyl]bis(methylene)} dipicolinic acid (H ₇ alenpa) (Scheme 4.5)	111
4.4.4	Solution depletion studies	112
4.4.5	General synthesis of La(III)-dpa complexes (Scheme 4.6)	113
4.4.6	Solution thermodynamics	114
4.4.7	Determination of octanol-water partition coefficients	115

Chapter 5: Conclusions, ongoing studies, and future directions	116
5.1 Conclusions.....	116
5.2 Ongoing studies	118
5.2.1 Expanding the dpa series (part I): Adding lipophilic functionality	118
5.2.2 Spatial mapping of La in bone by laser ablation ICP-MS	120
5.2.3 Ongoing <i>in vivo</i> studies.....	122
5.3 Future studies	123
5.3.1 Further <i>in vitro</i> experiments with La(XT) the dpa compounds	123
5.3.2 Expanding the dpa series part (II): A larger binding cavity.....	124
5.3.3 Other potential ligands.....	126
References.....	128
Appendices.....	138
¹ H NMR spectra for Hdpp and H ₅ XT.....	138
Lanthanum ICP-MS calibration plot.....	140
X-ray crystal structures of dipicolinic acid ligands	141
¹ H NMR spectra for H ₂ dpa and La(dpa).....	143
¹ H NMR spectra for H ₃ cedpa and La(cedpa).....	144
¹ H NMR spectra for H ₄ pedpa and La(pedpa) ⁻	145
H ₄ pedpa pH-dependent ³¹ P{ ¹ H} NMR spectra	146
¹ H NMR spectrum for La(dpa) ₂	147
Molar extinction coefficients of dpa ligands and La complexes	148

List of Tables

Table 1.1 Comparison of two approved drugs, Quadramet and Xofigo, for the treatment of metastatic bone cancer. ²⁷	9
Table 2.1 Crystallographic data.	34
Table 2.2 Comparison of thermodynamic data from ITC analysis of free La ³⁺ (from Reference 11) and La ³⁺ with Hdpp measured at 37 °C and pH 5.0.....	37
Table 3.1 Pharmacokinetic parameters derived from non-compartmental analysis ($n = 6$; mean \pm std. dev.) of the data presented in Figure 3.1 using Phoenix software (Ver. 1.3).....	56
Table 4.1 Summary of the range of the ways in which H ₂ dedpa (Figure 4.2) can be modified to either target specific <i>in vivo</i> functionality (upper), or to bind radiometals other than gallium-67/68 (lower).....	75
Table 4.2 Comparison of the chemical shifts (δ) and coupling constants (2J) of the backbone methylene protons in the lanthanum complexes of the three dpa ligands.	89
Table 4.3 Crystallographic data.	92
Table 4.4 Selected bond lengths and angles.....	92
Table 4.5 Stepwise ($\log K_a$) and cumulative ($\log \beta$) protonation constants for dpa and pedpa determined by potentiometric titrations (298 K, [L] = 1.0 x 10 ⁻³ M, I = 0.16 M NaCl) performed by Dr. Jaraquemada-Peláez at UBC.....	96
Table 4.6 Comparison of the complex formation constants ($\log K_{LaL}$ and $\log \beta_{LaHL}$) and pLa values for lanthanum with dpa, pedpa, and XT (from ref. 68).....	99
Table 4.7 Experimentally determined $\log P_{o/w}$ values. ^a	102
Table A.1 Crystallographic data.....	142

Table A.2 Experimentally measured molar extinction coefficients (ϵ) and absorbance maxima (λ_{max}) for all compounds for which concentration was determined by UV-Vis. Measurements were performed at ambient temperature in a background solution of HEPES buffer (50 mM, $I = 0.16$ M) at a path length of 1 cm..... 148

List of Figures

Figure 1.1 The remodeling cycle, mediated by bone building osteoblasts (green) and bone resorbing osteoclasts (blue).....	1
Figure 1.2 The structure of hydroxyapatite, as viewed along the <i>c</i> -axis. ⁸	4
Figure 1.3 Postulated structure of samarium-153-ethylenediamine- <i>N,N,N',N'</i> -tetrakis(methylene phosphonic acid) (¹⁵³ Sm-EDTMP), routinely used for the treatment of bone metastases.....	7
Figure 1.4 The radioactive decay cascade of radium-223; the safe use of Xofigo has been attributed to the short-live half-lives of its α -emitting daughter nuclides.	10
Figure 1.5 A comparison healthy bone (left) and osteoporotic bone with low mineral density (right). ²⁹	12
Figure 1.6 Structure of the pyrophosphate (left) moiety found in living systems and bisphosphonate (right), incorporated in molecular structures to act as a bone-seeking agent.....	13
Figure 1.7 The structures of four approved bisphosphonates for the treatment of osteoporosis (from left to right): alendronate; risedronate; zoledronate; ibandronate.....	14
Figure 1.8 The structure of strontium(II) ranelate, an approved drug for the treatment of osteoporosis.....	16
Figure 1.9 Tuning the ligand environment to include more lipophilic functionalities is a strategy that has been used by medicinal chemists in order to improve the oral bioavailability of metal-based drugs.....	20
Figure 1.10 The structures of two compounds which became leads in the search for an orally active lanthanum complex for treating osteoporosis: a) La(dpp) ₃ ; and b) K ₂ [La(XT)]. ⁶⁷⁻⁶⁹	22
Figure 2.1 General structure of a) 3-hydroxy-4-pyrone and b) 3-hydroxy-4-pyridinone, metal complexes of which have been explored for a number of medical applications. ⁷⁰	24

Figure 2.2 Cell uptake in Caco-2 cells of LnL₃ determined by ICP-MS. La(dpp)₃ is the only system to exhibit greater uptake than La₂(CO₃)₃ (Fosrenol). Reproduced from reference 67..... 26

Figure 2.3 Cell uptake of La(III) in Caco-2 cells in the presence of various ligand systems, as measured by ICP-MS. La(XT)²⁻ shows the greatest uptake, corresponding to the highest GI tract absorption. Reproduced from reference 69..... 28

Figure 2.4 The raw ITC plot (upper) of La³⁺ (10 μL injections, 3.15 mM) into HAP (0.1 mM) at pH 5.0 (100 mM piperazine) and 37 °C, and the integrated data (lower) giving $n = 2.4(1)$; $K_{app} = 2.4(2) \times 10^6$; $\Delta H = -6.61(8)$ kcal/mol; $T\Delta S = 2.45$ kcal/mol; $\Delta G = -9.06$ kcal/mol. Reproduced from reference 11..... 31

Figure 2.5 ORTEP diagram of the crystal structure of La(dpp)₃(H₂O)₂·11.75H₂O showing the network of hydrogen bonded water molecules (left), and, for clarity, only the water molecules bonded directly to the La³⁺ centre (right). 33

Figure 2.6 Representative data for ITC analysis of ligand and metal/ligand binding to HAP at 37°C, pH 5.0 (100 mM piperazine). A: Raw titration data (upper) for 10 μL injections of Hdpp (9.8 mM) into HAP (0.9 mM) and the integrated data (lower). B: Raw titration data (upper) for 10 μL injections of La³⁺ (2.5 mM) in the presence of Hdpp (10 mM) into HAP (0.1 mM) and the integrated data (lower) with best fit line to a one-site bimolecular binding model. C: Raw titration data (upper) for 10 μL injections of H₅XT (80 mM) into HAP (1.5 mM) and the integrated data (lower) with best fit line to a one-site bimolecular binding model. D: Raw titration data (upper) for 10 μL injections of La³⁺ (80 mM) in the presence of H₅XT (90 mM) into HAP (1.5 mM) and the integrated data (lower). 36

Figure 2.7 Speciation plots for typical ITC conditions for a) syringe concentrations (2.5 mM La³⁺ and 10 mM Hdpp) and b) conditions in the reaction cell after the first injection (0.018 mM La³⁺ and 0.071 mM Hdpp). 38

Figure 2.8 ITC analysis data of H₅XT into HAP at 37°C, pH 7.4 (100 mM HEPES). Raw titration data (upper) for 10 µL injections of H₅XT (30.4 mM) into HAP (1.1 mM) and the integrated data (lower) fitted to a one-site bimolecular binding model. 39

Figure 2.9 Speciation plots for typical ITC conditions in the reaction cell over the course of a single experiment. 40

Figure 2.10 The depletion of La³⁺ over 24 hours measured in solution by ICP-MS at 37 °C and pH 7.4 (100 mM HEPES buffer) as a percentage of [La³⁺] in solution at time zero (*n* = 3). A: The plot for La(dpp)₃, also showing the percentage of Hdpp measured by UV-Vis. B: The plot for K₂[La(XT)]. 43

Figure 2.11 The depletion of La³⁺ over 3 minutes measured in solution by ICP-MS at 37 °C and pH 7.4 (100 mM HEPES buffer) as a percentage of [La³⁺] in solution at time zero (*n* = 3). A: La(dpp)₃. B: K₂[La(XT)]. 44

Figure 2.12 Synthesis of La(dpp)₃ from Hdpp and lanthanum nitrate hydrate and pH adjustment in aqueous conditions at room temperature. 47

Figure 2.13 Synthesis of H₅XT as the HCl salt in a one-pot Mannich reaction from commercially available starting materials. 48

Figure 2.14 Synthesis of La(XT) from the HCl salt of H₅XT and lanthanum nitrate hexahydrate using pH adjustment under aqueous conditions at room temperature. 49

Figure 3.1 Plasma lanthanum concentration time (h) profile following single IV dose (1 mg kg⁻¹) of La(dpp)₃ in SD rats (*n* = 6). 55

Figure 3.2 Soft-tissue distribution of La^{3+} after 5 days following single IV dose (1 mg kg^{-1}) of $\text{La}(\text{dpp})_3$ ($n = 6$; mean \pm std. dev.).....	55
Figure 3.3 Biodistribution of La^{3+} from the complexes $\text{La}(\text{dpp})_3$ and $\text{La}(\text{XT})$ following multiple IV dose administrations at $1 \text{ mg kg}^{-1} \text{ day}^{-1}$ for 5 days in SD rats ($n = 6$; mean \pm std. dev.).....	58
Figure 3.4 Distribution of lanthanum within the femur from the complexes $\text{La}(\text{dpp})_3$ and $\text{La}(\text{XT})$ after multiple doses of $1 \text{ mg kg}^{-1} \text{ day}^{-1}$ for 5 days in SD rats ($n = 6$; mean \pm std. dev.).....	59
Figure 3.5 Biodistribution of La^{3+} from the complexes $\text{La}(\text{dpp})_3$ and $\text{La}(\text{XT})$ following multiple IV dose administrations at $1 \text{ mg kg}^{-1} \text{ week}^{-1}$ for 4 weeks in SD rats ($n = 4$; mean \pm std. dev.)..	62
Figure 3.6 Biodistribution of La^{3+} from the complexes $\text{La}(\text{dpp})_3$ (two formulations) and $\text{La}(\text{XT})$ following multiple oral dose administrations at $50 \text{ mg kg}^{-1} \text{ day}^{-1}$ for 4 weeks in SD rats ($n = 4$; mean \pm std. dev.).....	62
Figure 3.7 Distribution of lanthanum within the femurs of SD rats from oral administration with either $\text{La}(\text{dpp})_3$ (CMC or Gelucire formulation), or $\text{La}(\text{XT})$ after dosing at $50 \text{ mg kg}^{-1} \text{ day}^{-1}$ for 4 weeks; and IV administration with either $\text{La}(\text{dpp})_3$ or $\text{La}(\text{XT})$ after multiple doses of $1 \text{ mg kg}^{-1} \text{ week}^{-1}$ for 4 weeks ($n = 4$; mean \pm std. dev.).....	63
Figure 3.8 Expansion of the distribution of lanthanum within the femurs of SD rats showing only the results from oral administration ($50 \text{ mg kg}^{-1} \text{ day}^{-1}$) for 4 weeks with either $\text{La}(\text{dpp})_3$ (two formulations) or $\text{La}(\text{XT})$ ($n = 4$; mean \pm std. dev.).....	63
Figure 3.9 Elemental mapping of lanthanum (red) in a cross-section of lower lumbar spine from a SD rat treated with $\text{La}(\text{XT})$ by IV administration ($1 \text{ mg kg}^{-1} \text{ week}^{-1}$) for 4 weeks. The image was obtained by KES method at the CLS at a resolution of $13 \mu\text{m}$ from a tunable monochromatic X-ray source, which can be adjusted to the K-edge of lanthanum (39 keV).	66

Figure 4.1 General structure of H₂dpa, where R is a functional group designed to enhance metal chelation and/or bone targeting..... 73

Figure 4.2 The H₂dedpa scaffold, which forms the basis for a number of acyclic dipicolinic acid-based chelators which can be modified to tailor both *in vivo* targeting and radiolabelling properties (see Table 4.1)..... 74

Figure 4.3 The names and structures of the four picolinic acid-containing ligands explored in this chapter..... 77

Figure 4.4 Solution depletion plots showing the [ligand] remaining in solution (unbound to HAP) over 48 hours as a % of [ligand] at time = 0 hours (*n* = 3). Conditions for all experiments: 37 °C, pH 7.4, *I* = 0.16 M (NaCl), agitation at 220 rpm. A: H₂dpa; B: H₃cedpa; C: H₄pedpa; D: H₇alenpa. 83

Figure 4.5 A plot of the natural log (red) and the inverse (yellow) of [H₄pedpa] vs. time derived from the data presented in Figure 4.4 C. The data suggest an order dependence on [H₄pedpa] between 1 and 2. 85

Figure 4.6 A plot of the natural ln [H₇alenpa] *versus* time, giving an approximately linear plot and a first order rate constant *k* = 0.1017 h⁻¹. 86

Figure 4.7 Portion of ¹H NMR spectrum showing the typical upfield shift and diastereotopic splitting of the methylene protons (marked) observed upon chelation of the dpa ligands to lanthanum (400 MHz, D₂O, 298 K). The full ¹H NMR spectra are presented in Appendix..... 88

Figure 4.8 ORTEP diagram of the crystal structure of tetrameric [La₄(pedpa)₄(H₂O)₂] solved by direct methods by Dr. Brian Patrick (UBC) and modeled without lattice solvent, showing the asymmetric unit (upper) and the complete unit cell (lower) consisting of two asymmetric units. All

hydrogen atoms (with the exception of those on water bound to La₂) omitted for clarity, as well as the C-H groups of the pyridine rings in the unit cell diagram. 91

Figure 4.9 ChemDraw representation of the facial binding mode and acute N-La-N bond angle adopted by the dpa cavity in the solid-state structure of [La₄(pedpa)₄(H₂O)₂]. 93

Figure 4.10 Speciation plots for dpa (left) and pedpa (right). Protonation constants are reported in Table 4.5. Relative ³¹P{¹H} NMR chemical shifts as a function of pH are superimposed on the plot for pedpa (right) (see Appendix). 95

Figure 4.11 Upper: A portion of the ¹H NMR spectra for the La³⁺-dpa system in D₂O (400 MHz, 298 K, [La]:[dpa] ~ 1:1.6). Lower: Speciation plot for the same system ([La]:[dpa] = 1:1, 298 K, *I* = 0.16 M NaCl). 97

Figure 4.12 A portion of the ¹H NMR spectra for the La³⁺-dpa system in D₂O (400 MHz, 298 K). [La]:[dpa] ~ 1:1.6. 98

Figure 4.13 Upper: A portion of the ¹H NMR spectra for the La³⁺-pedpa system in D₂O (400 MHz, 298 K, [La]:[pedpa] ~ 1:1.4). Lower: Speciation plot for the same system ([La]:[pedpa] = 1:1, 298 K, *I* = 0.16 M NaCl). 98

Figure 5.1 A proposed expansion to the dpa scaffold – d-MeO-pa – incorporating lipophilic methoxy moieties. 118

Figure 5.2 An epoxy-mounted rat femur suitable for analysis by LA ICP-MS. The puck was manufactured by cleaning the bones manually of soft flesh, followed by fixing in freshly-made epoxy and allowing hardening for 24 hours. The bone surface was then prepared by sanding, followed by mechanical polishing with progressively finer polishing gels (6 μm, 3 μm, and 1 μm) leaving a shiny exposed flat surface. The red arrow shows the path traced by the laser during LA ICP-MS analysis, and gives an indication of the spatial resolution that could be obtained. 121

Figure 5.3 Literature examples of possible chelators for La^{3+} ions. H_8EDTMP = ethylenediamine tetrakis(methylene phosphonic acid);²⁰ H_{10}DTPP = diethylenetriamine pentakis(methylene phosphonic acid);¹²⁹ H_8CDTP = 1,6-cyclohexyldiamine tetrakis(methylene phosphonic acid);¹²⁸ H_8DMPDTP = 1,3-diamino-2-isopropylpropane tetrakis(methylene phosphonic acid).¹³⁰ 127

Figure A.1 ^1H NMR spectrum for Hdpp (D_2O , 298 K, 300 MHz). 138

Figure A.2 ^1H NMR spectrum for H_5XT (D_2O , 298 K, 300 MHz). 139

Figure A.3 A typical ICP-MS calibration plot for lanthanum with 10 ppb rhodium as an internal standard. 140

Figure A.4 Solid-state X-ray structures for crystals of $\text{H}_2\text{dpa}\cdot\text{H}_2\text{O}$, obtained by Dr. Lisa Murphy (upper), of $\text{H}_3\text{cedpa}\cdot\text{H}_2\text{O}$, obtained by Dr. Caterina Ramogida (middle), and of $\text{H}_4\text{pedpa}\cdot 3\text{H}_2\text{O}$ (lower). All measurements were made on a Bruker X8 APEX II diffractometer, and the data were collected and integrated using Bruker SAINT software. The structures were solved by Dr. Brian Patrick by direct methods. All non-hydrogen atoms were refined anisotropically. All N-H and O-H hydrogen atoms were located in difference maps and refined isotropically. All other hydrogen atoms were placed in calculated positions. Crystallographic data is presented in Table A.1..... 141

Figure A.5 ^1H NMR spectra for H_2dpa (upper) and $\text{La}(\text{dpa})$ (lower) in D_2O (300 MHz) at ambient temperature. 143

Figure A.6 ^1H NMR spectra for H_3cedpa (upper) and $\text{La}(\text{cedpa})$ (lower) in D_2O (300 MHz) at ambient temperature..... 144

Figure A.7 ^1H NMR spectra for H_3pedpa (upper) and $\text{La}(\text{pedpa})^-$ (lower) in D_2O (300 MHz) at ambient temperature..... 145

Figure A.8 The $^{31}\text{P}\{^1\text{H}\}$ NMR spectra (298 K, 162 MHz) for H_4pedpa recorded at various pH levels and used to calculate the first $\text{p}K_a$ for the compound (Figure 4.10) using the HypeNMR2008 and Hyss programs.¹¹³ 146

Figure A.9 ^1H NMR spectrum of a 2:1 mixture dpa:La in D_2O at pD 12.3 (400 MHz) at 298 K. 147

List of Symbols and Abbreviations

°	degrees
°C	degrees Celsius
[]	concentration
©	copyright
®	registered trademark
Å	Angstrom
α	alpha (emissive particle)
β	beta (emissive particle)
γ	gamma (emissive ray)
δ	chemical shift (ppm)
Δ	change
ϵ	molar extinction coefficient
θ	angle
λ_{\max}	absorbance maxima
μ	micro (10^{-6})
Ω	ohm(s) (resistance)
2D	2-dimensional
3D	3-dimensional
AA	atomic absorption
ACS	American Chemical Society
ACUP	Animal Care and Use Program
adsorp.	adsorption

Anal.	analytical
Ar	aryl
AU	asymmetric unit
AUC _{0-∞}	area under curve
AUMC _{0-∞}	area under first moment curve
approx.	approximately
BEC	blank equivalent concentration
BET	Brunauer-Emmett-Teller (surface area analysis)
BP	bisphosphonate(s)
br	broad (NMR)
C ₀	initial concentration
Caco-2	human colon adenocarcinoma-derived cell line
cal	calories
Calc'd	calculated
CCAC	Canadian Council on Animal Care
CLS	Canadian Light Source
Cl	total body clearance
CMC	carboxymethyl cellulose
CN	coordination number
CRM	certified reference material
CT	computed tomography
d-MeO-pa	di-(4-methoxy)picolinate
d	day(s); doublet (NMR)

DCM	dichloromethane
dd	doublet of doublets (NMR)
DFT	density functional theory
DI	deionized
DL	detection limit
DMSO	dimethyl sulfoxide
dpa	dipicolinic acid
DRESS	drug rash with eosinophilia and systemic symptoms
dt	doublet of triplets (NMR)
E_0	standard electrode potential
EA	elemental analysis
EC ₅₀	half-maximal effective concentration
EDTA	ethylenediamine- <i>N,N,N',N'</i> -tetraacetic acid
EDTMP	ethylenediamine- <i>N,N,N',N'</i> -tetrakis(methylene phosphonate)
en	ethylenediamine
EOS	Earth and Ocean Sciences
ESI-MS	electrospray ionization mass spectrometry
ESRD	end-stage renal disease
eV	electronvolt(s)
EXAFS	extended X-ray absorption fine structure
FDA	Food and Drug Administration
FTIR	Fourier transform infrared
g	gram(s)

<i>G</i>	Gibbs free energy
G°	standard Gibbs free energy
Gelucire	Gelucire 44/14 and Peceol formulation
Gelucire 44/14	surfactant composed of PEG-esters, glyceride, and free PEG
GI	gastrointestinal
h	hour(s)
<i>H</i>	enthalpy
HAP	hydroxyapatite
HD	high definition
HEPES	4-(2-hydroxyethyl)-1-piperazineethanesulfonic acid
HPLC	high-pressure liquid chromatography
HR	high resolution
Hz	hertz (frequency)
<i>I</i>	ionic strength (molarity)
IC ₅₀	half-maximal inhibitory concentration
ICP-MS	inductively coupled plasma mass spectrometry
ICP-OES	inductively coupled plasma optical emission spectrometry
IR	infrared
ITC	isothermal titration calorimetry
IV	intravenous
<i>J</i>	coupling constant (NMR)
k	kilo (10 ³)
<i>K</i> _a	acid association constant

K_{app}	apparent equilibrium constant of association
K_{el}	elimination rate constant
K_{ML}	formation constant (metal-ligand)
K_w	the water ion product
KES	K-edge subtraction
L	litre; ligand
LA	laser ablation
lexidronam	<i>see</i> EDTMP
$\log \beta$	cumulative formation constant
L_n	lanthanide
m/z	mass to charge ratio
m	metre(s); milli (10^{-3})
min(s)	minute(s)
M Ω -cm	water resistivity (purity measure)
M	molarity (mol/L); mega (10^6)
MDP	methylenediphosphonate
MG-63	human osteosarcoma-derived cell-line
mol	moles
MQ	Milli-Q
MRI	magnetic resonance imaging
MRT	mean residence time
MTT	3-(4,5-dimethylthiazol-2-yl)-2,5-diphenyltetrazolium bromide
n	nano (10^{-9})

<i>n</i>	stoichiometric ratio; number of trials
NI	nitroimidazole
NIST	National Institute of Standards and Technology
NMR	nuclear magnetic resonance
Nosyl	2-nitrobenzenesulfonamide
ORTEP	Oak Ridge Thermal-Ellipsoid Plot Program
OVX	ovariectomised
<i>P</i>	partition coefficient
<i>P</i> _{o/w}	1-octanol-water partition coefficient
pa	picolinic acid
PCIGR	Pacific Centre for Isotopic and Geothermal Research
pH	potential hydrogen, -log [H ⁺]
Peceol	vehicle for use in self-emulsifying lipid formulations
PEG	polyethylene glycol
PET	positron emission tomography
ppb	parts per billion
ppm	parts per million
ppt	parts per trillion
Py	pyridine
R	gas constant
<i>R</i>	right-handedness (Cahn-Ingold-Prelog priority rules)
R ²	curve fit
rpm	revolutions per minute

RT	room temperature
s	second(s); singlet (NMR)
S	entropy; left-handedness (Cahn-Ingold-Prelog priority rules)
SD	Sprague-Dawley
SERM	selective estrogen receptor modulator
SPECT	single-photon emission computed tomography
SRM	standard reference material
std. dev.	standard deviation
t	triplet (NMR)
t _½	half-life
T	temperature
TGA	thermogravimetric analysis
THF	tetrahydrofuran
TLC	thin layer chromatography
Tween-80	polyoxyethylenesorbitan monooleate (polysorbate 80)
UACC	University Animal Care Committee
UV-Vis	ultraviolet-visible
Ver.	version
V _{ss}	volume of distribution at steady state
w/w	weight by water
wt.	weight
XAS	X-ray absorption spectroscopy
XRD	X-ray diffraction

List of Schemes

Scheme 4.1 Synthetic route to the alkylating agent methyl 6-(bromomethyl) picolinate (3). ^a	78
Scheme 4.2 Synthetic route to H ₂ dpa as the HCl salt. ^a	79
Scheme 4.3 Synthetic route to H ₃ cedpa as the HCl salt. ^a	79
Scheme 4.4 Aza-Michael addition mechanism and synthetic route to H ₄ pedpa as the HCl salt. ^a	80
Scheme 4.5 Synthetic route to H ₇ alenpa as the HCl salt. ^a	80
Scheme 4.6 General procedure for the synthesis of the 1:1 lanthanum complexes of three dpa-based ligands.	87
Scheme 5.1 Previously reported synthetic route to the alkylating agent methyl (6-bromomethyl)-4-methoxypicolinate (17). Reported cumulative yield: 31%. ⁹²	119
Scheme 5.2 Proposed synthetic route to H ₆ dipedpa.	125
Scheme 5.3 Proposed synthetic route to H ₅ XTdpa.	126

List of Equations

Equation 2.1 Relationship between Gibb's free energy and apparent equilibrium association constant.....	30
Equation 4.1 Differential rate law for the binding of H ₇ alenpa to hydroxyapatite.....	85
Equation 4.2 Lanthanum-ligand association constant, K_{LaL}	99
Equation 4.3 Protonation constant for the lanthanum-ligand complex, K_a	99
Equation 4.4 Cumulative formation constant β_{LaLH}	99
Equation 4.5 Octanol-water partition coefficient $P_{o/w}$	102

Acknowledgements

My thanks, first and foremost, goes to my Mum, Shelagh, who has selflessly supported me in every major decision I have made throughout my adult life, including moving to Canada five years ago to pursue this degree. Your unwavering wisdom, love, optimism, and positive attitude have always been – and will continue to be – an inspiration to me, and I’ve learnt more from you than you will ever know.

To the friends I have made in Vancouver, who are the foundation for the incredible life I get to live here, thank you for being such an awesome, diverse, and fun-loving group of people, and for keeping me balanced and always feeling young. And to my friends back in the UK, thank you for reminding me to come home once in a while.

Thank you to all the wonderful people I have worked with at UBC, including Yasmin Mawani who guided me through the first few months of this project; Madeline Iafrate and Jay Chi for their hard work (and entertainment provided) during their undergraduate projects; and to all other group members past and present. The list of names – from collaborators, to staff members, to instructors – that I need to thank could go on for pages, but in particular I must thank Jacquie Cawthray, who has helped me on so many fronts throughout my degree. She has made a colossal contribution to this project, and is integral to its ongoing success.

Finally, to my supervisor, Chris Orvig, to whom I owe the greatest of thanks for your support, trust, and intellectual guidance throughout my Ph.D. You are a role model both at work and on the ski hill, and your wholehearted dedication to your students is felt by everyone who has been in your group. I feel privileged to have been able to call you “The Boss”.

Chapter 1: Introduction

1.1 Bone structure, function, and disease

The human skeleton, comprising over 200 individual bones, is the internal framework that supports and maintains the distinctive shape of our bodies, providing protection to underlying soft tissues and organs, as well as acting as a storage mechanism for the regulation of hormones and minerals. The most evident property of bone which enables the skeleton to carry out these vital functions is hardness, which can be attributed to the densely packed mineral matrix in cortical bone which makes up around 80% of all bone tissue.¹

Contrary to intuition, bone is a highly dynamic living tissue. It is constantly undergoing a remodeling cycle of resorption and formation, tightly controlled by a number of systemic and local pathways, and kept in balance through a homeostasis. In a simplified schematic, the primary cell groups involved in this turnover cycle are osteoblasts – responsible for bone building, and osteoclasts – responsible for bone resorption (Figure 1.1). During periods of growth and development, bone formation is dominant until adulthood is reached and the two processes occur more or less consistently across the skeleton. Bone turnover may be upregulated at sites of high stress such as the joints, or act as a repair mechanism for damaged bone.²

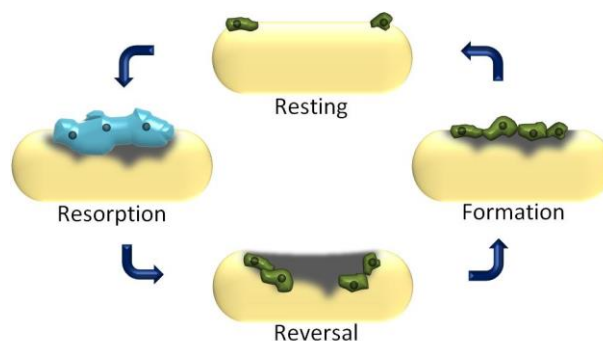


Figure 1.1 The remodeling cycle, mediated by bone building osteoblasts (green) and bone resorbing osteoclasts (blue).

When the bone turnover cycle becomes uncoupled and therefore imbalanced, skeletal diseases occur. A common example is osteoporosis (discussed further in section 1.4) in which the rate of resorption outweighs that of formation leading to bones with decreased mineral density, increased brittleness, and a heightened susceptibility towards damage and fracture.³ Another skeletal disorder is Paget's disease of the bone, in which both resorption and formation rates are augmented and new bone is deposited in a highly disordered fashion leading to abnormal growth, localized pain, and weakened bone.⁴ As well as these specific conditions, perturbations to the bone cycle often arise in cancer patients when metastatic tumour cells migrate to osseous tissues. In these cases, disruptions can come about in a number of ways including uncontrolled proliferation of pre-differentiated osteoblasts, inhibition of cell apoptosis, and blocking of various signal pathways leading to deregulated and chaotic growth or mineral depletion.⁵

In spite of these numerous causes of skeletal disorders, they all share a few unifying aspects: they are challenging to diagnose, particularly at early stages; they are painful and debilitating; and there are a very limited number of safe and effective pharmaceutical agents available to treat them. Because of a special relationship between metal ions and osseous tissues, inorganic drugs play a crucial role in this area, and it is often the goal of medicinal chemists to exploit this relationship to design tools for both therapy and diagnosis of bone diseases.

1.2 Bone as a target for metal ions

Metal ions play a vital role in medicinal chemistry. A few metals are considered essential, such as copper, iron, and zinc, and are actively incorporated into our diet in order to maintain a good state of health. The remaining "non-essential" metals have historically been considered exclusively toxic; however, that notion has been increasingly confronted as the field of medicinal inorganic

chemistry has grown. The unique electronic properties, variable oxidation states, flexible coordination numbers, and in some cases radiochemical properties of metal ions present both challenges and opportunities in drug design, with emphasis often placed on developing reliable dose-response data, and rational ligand design in order to improve target specificity and drug efficacy.⁶ The skeleton is a natural sink for metal ions which are absorbed by the body. Those which are not excreted eventually accumulate in the bone matrix, where retention times can be in excess of several years. Often, a key aspect to any metallodrug design paradigm is preventing the natural tendency for metal ions to gravitate towards bone, since the fixing of metals in skeletal tissue limits their bioavailability, and therefore hinders activity towards an intended target. The retention of metals in hard tissues has also proven crucial in an archaeological sense, where trace metal analysis of bones from various eras has unearthed information about environment, pollution, and human health and behaviour from multiple generations.⁷

Biological bone mineral bears a close resemblance to hydroxyapatite (HAP), a naturally occurring calcium phosphate with the formula $[\text{Ca}_5(\text{PO}_4)_3\text{OH}]_n$, crystallised in a hexagonal lattice and stacked in a plate-like fashion with two distinct calcium(II) environments, one seven coordinate and one nine coordinate (Figure 1.2).⁸ The skeleton's propensity to attract and retain metal ions is often attributed to the vast number of potential binding interactions present within the HAP-like matrix, as well as its ability to undergo both cationic and anionic substitution without incurring significant structural alterations.⁹ Multiple studies have therefore used HAP as a model for trying to predict the mechanistic intricacies of metal ion substitution in bone tissue, and the physiological impact this has.^{10,11}

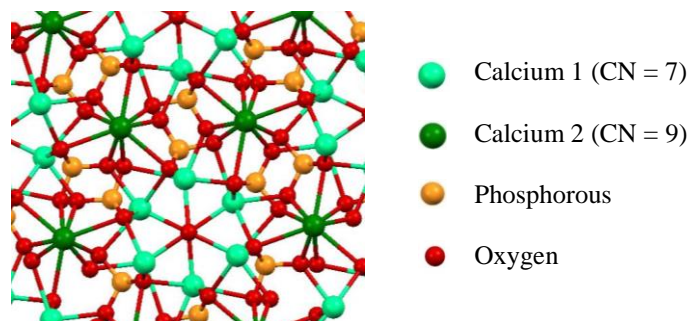


Figure 1.2 The structure of hydroxyapatite, as viewed along the *c*-axis.⁸

This relationship between metals and bones is particularly important in the case of the 4f transition metals – referred to as the lanthanide (Ln) series – which include the 15 elements from lanthanum to lutetium. These elements have a wide number of applications, and in a medicinal context alone they have found uses as antimicrobials, treatments for burn wounds, cancer imaging and therapy agents, and renal disease treatments.¹² In aqueous solution the lanthanides tend to form stable 3+ ion complexes and differ only slightly in their chemical behaviour across the series, with ionic radii for coordination numbers between 6 and 9 ranging from approximately 1.06 Å for La(III) to 0.85 Å for Lu(III), similar to Ca(II) which has a radius 0.99 Å.¹³ Their exceptionally high affinity for bone tissue is easily explained by their preference for hard donor ligands and coordination numbers ranging from 7 to 10, which render them highly suited for substitution into HAP's phosphate-rich matrix.¹¹

In synthetic HAP, the predicted mechanism for isomorphous trivalent lanthanide incorporation into the mineral matrix includes surface sorption followed by diffusion into the crystal lattice, with cationic Ln(III)-Ca(II) substitution preferentially taking place at nine coordinate Ca2 sites, and the degree of substitution directly dependent on the similarity in ionic radius between Ca(II) and the guest ion;¹⁴ however, in living systems there is added complexity

from glycoproteins, collagen, and other amorphous calcium phosphate phases, rendering *in vivo* mechanistic predictions at the molecular level extremely challenging.¹⁵ As a result the interaction between the f-elements and bone tissue is an ongoing subject of interest and relevance, in order that their biochemistry and toxicology can be better understood.¹⁶

In some situations, medicinal chemists have attempted to take advantage of the skeleton's natural tendency for metal ion uptake by designing drugs in which diseased or damaged bone tissue is the intended target organ, and the properties of the metal ion (lanthanide or otherwise) are such that a desirable therapeutic or diagnostic effect could be invoked. Rarely is this a trivial task, and the considerations required and challenges involved go far beyond the basic interaction between the metal and bone mineral. One area which has seen repeated success in terms of approved pharmaceuticals is the use of radiometals for the treatment of metastatic bone cancer, and in the following section we will highlight these key cases.

1.3 Radiometals for metastatic bone cancer

1.3.1 Bone metastases

Metastatic bone tumours occur by the migration of cancerous cells from an existing lesion to skeletal tissues. For patients with malignant forms of cancer, it is an alarmingly common and disheartening occurrence, affecting more than 2 in 3 sufferers of prostate and breast cancer, and more than 1 in 3 sufferers of lung, thyroid, and kidney cancer.¹⁷ Lesions resulting from bone metastases can cause spinal-cord compressions, disruptions to musculoskeletal function, atypical fractures, and deregulated bone turnover. From a patient perspective the result is often pain and discomfort, loss of mobility, a reduced quality of life, and in many cases diminished life expectancy.¹⁸

Metal-based radiopharmaceuticals play a vital role in the treatment of bone metastases. Depending on the chemical and radioactive properties of the element selected, they have found applications in imaging and diagnosis of skeletal tumours, management and palliation of bone pain, and as therapeutic tools for the ablation of bone-based lesions. In all cases, it is the metal ion's affinity for bone tissue – particularly in areas of augmented turnover – that enable site specific treatment to take place.¹⁹⁻²⁶

1.3.2 Samarium-153

Under the trademark name Quadramet®, the samarium-153 complex of ethylenediamine-*N,N,N',N'*-tetrakis(methylene phosphonic acid) (¹⁵³Sm-EDTMP or ¹⁵³Sm-lexidronam, Figure 1.3) is one of the most well-known clinically approved drugs for treating bone metastases. Samarium is a relatively cheap and abundant lanthanide element, and it accordingly forms stable 3+ cations with a high affinity for bone mineral.¹¹ The clinical relevance of the ¹⁵³Sm isotope is due to a number of reasons: it has a short radioactive half-life of 47 h, which allows for fractional dosing and limits undesirable exposure times; it decays primarily by β-emission; however, also produces a γ signal enabling facile *in vivo* detection by conventional imaging techniques; it clears rapidly from the blood after injection, allowing efficient uptake in the target tissue; and it is relatively easy to produce by irradiation of enriched ¹⁵²Sm₂O₃.¹⁹

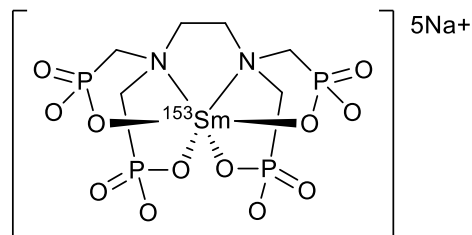


Figure 1.3 Postulated structure of samarium-153-ethylenediamine-*N,N,N',N'*-tetrakis(methylene phosphonic acid) (^{153}Sm -EDTMP), routinely used for the treatment of bone metastases.

Nitrate and citrate salts of ^{153}Sm have been briefly studied as more general tumour imaging agents; however, their biodistribution was inconsistent and unpredictable.²⁰ It was noted that chelation with EDTA led to increased skeletal uptake, which prompted investigation by Goeckeler *et al.* into a series of phosphonate-containing ligands with ^{153}Sm , with the aim of producing a single-species complex in which the ligand would contribute to both complex stability and bone targeting properties.²⁰ The afore-mentioned 1:1 ^{153}Sm -EDTMP compound successfully met these criteria, and progressed to animal studies where it was shown that the radionuclide accumulated preferentially in bone tumours as opposed to healthy bone, rationalized by the augmented rates of tissue turnover in skeletal lesions.¹⁹ These uptake results were emulated in human trials, along with rapid clearance from non-osseous tissues.²¹ This eventually led to drug approval by the FDA in the late 1990s, and since then ^{153}Sm -EDTMP has been continually scrutinized in various studies and reviews for its toxicity and efficacy. Most crucially – and from a clinical perspective – it appears that in most patients with bone metastases a partial-to-excellent degree of pain palliation results from samarium-153 β -emission particles.²² Alleviation occurs rapidly (within a few days) and can last up to 6 weeks after injection, leading to increased mobility, better sleep, and improved quality of life.

Interestingly, in spite of the vast amount of clinical and biochemical research that has been performed on ^{153}Sm -EDTMP, an X-ray crystal structure of the complex with the stable Sm(III) isotope has never been obtained. It was only in 2015 that Yang, Pushie *et al.* were able to use a variety of spectroscopic and computational methods, including extended X-ray absorption fine structure (EXAFS), DFT, FTIR, and NMR, to give the first characterization of Sm-EDTMP at atomic resolution.²³ The coordinating environment observed for Sm(III) was in good agreement with the atomic arrangement that has long been hypothesized (Figure 1.3), and this refinement in structural resolution allows a better understanding of the drug's *in vivo* behaviour, and enables well-guided modifications that could lead to an improvement in efficacy.

1.3.3 Radium-223

In May 2013 the drug Xofigo® (Radium-223 dichloride, $^{223}\text{RaCl}_2$) was approved by the FDA in the United States for the treatment of metastatic bone cancer originating from prostate cancer. Similar to Quadramet, an injected dose clears efficiently from the blood and accumulates preferentially in areas with metastatic bone lesions or osteosarcomas due to high bone turnover in these regions.²⁴ Unlike samarium, radium is an alkaline earth metal – the same group as calcium – and as the 2+ ion it targets bone tissue *in vivo* almost exclusively and without a carefully designed ligand system.²⁴

The most significant differences between the two drugs can be inferred by their radioactive properties (summarized in Table 1.1). The ^{223}Ra isotope decays via emission of α -particles, which are heavier, of higher energy, and inherently more damaging than β -particles. This is advantageous as it induces a greater cytotoxic effect towards bone tumour cells, effectively enabling site-specific radioactive ablation of cancerous tissue from inside a patient. Moreover, since α -particles can only

penetrate a fraction of the distance from their origin compared to β -particles, the amount of unwanted damage to neighbouring bone marrow is minimized, and the localization of the radiation that is delivered is improved.²⁵ This results not only with fast and effective pain palliation, but a marked improvement in life expectancy for sufferers of metastatic bone cancer.²⁶

Table 1.1 Comparison of two approved drugs, Quadramet and Xofigo, for the treatment of metastatic bone cancer.²⁷

Trademark name	Quadramet	Xofigo
Radionuclide	¹⁵³ Sm	²²³ Ra
Ligand environment	EDTMP	Chloride
Emitted particle	β	α
Half-life (days)	1.9	11.4
Particle range (μm)	>500	50-100
Gamma imaging	Yes	Yes
Pain palliation	Yes	Yes
Prolonged survival	None evidenced	Yes

This is not the first time that researchers have attempted to exploit the ablative properties of α emitters in radiotherapy. In fact, in the early twentieth century a different radium isotope, radium-226, was also used for the treatment of bone cancer, but it was eventually declared unsuitable as its decay pathway leads to the gaseous α -emitting daughter nuclide radon-222 which can diffuse away from its origin over a long half-life ($t_{1/2} = 3.8$ days) and impose severe unwanted damage on neighbouring tissues.²⁵ Conversely, the decay cascade of ²²³Ra (Figure 1.4) leads initially to radon-219 which decays much more rapidly ($t_{1/2} = 4.0$ seconds), preventing the undesirable dispersion of radiation. It is this “safe” decay pathway associated with ²²³Ra that makes it one of the few α -emitters considered suitable for internal therapy.^{25,26}

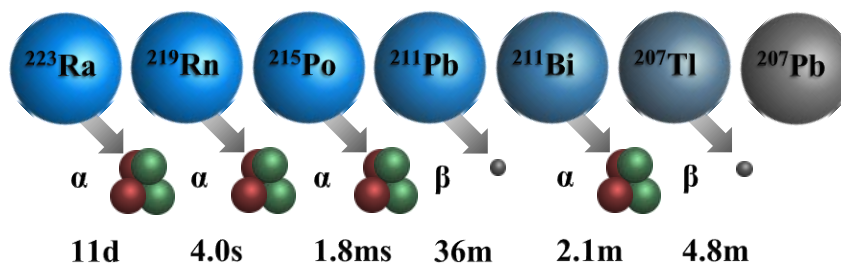


Figure 1.4 The radioactive decay cascade of radium-223; the safe use of Xofigo has been attributed to the short-lived half-lives of its α -emitting daughter nuclides.

1.3.4 Other radiometals

Radium and samarium are two elements radioisotopes of which have been applied in the successful development of drugs for treating bone metastases due to their exceptionally high affinity for bone mineral, and in particular their high uptake in cancerous regions where turnover rates are high in preference to healthy bone. As mentioned previously, several other metals in the periodic table also have a strong tendency to be retained by osseous tissues, and considering the chemical tuning that can be achieved with ligand design the scope for drug development is vast. An example of another radiometal – which has proved vital in a diagnostic sense – is technetium-99m, which when combined with the ligand methylenediphosphonate (MDP) is routinely used in the clinic as an agent for the detection of bone metastases.²⁷ MDP enhances the specific uptake of ^{99m}Tc in bone lesions, where the metal is retained and its emitting properties allow for SPECT imaging. Other radiometals investigated to varying degrees of success in the treatment or diagnosis of cancerous bone include strontium-89, yttrium-90, tin-117m, holmium-166, thulium-170, lutetium-177, rhenium-186 and rhenium-188.²⁸

It should be noted that, in spite of the benefits discussed thus far of applying radioactive metals as medicinal agents, they come with the invariable drawback of exposing healthy tissues to

harmful radiation. This is especially true when dosing is elevated to invoke a therapeutic response, as is the case for both Quadramet and Xofigo. Common side-effects associated with radioactive therapies include nausea, vomiting, diarrhoea, and, in particular for drugs intended for targeting bone, aching of the joints and a reduced white blood cell count. The use of such drugs is only justifiable in the case of bone metastases due to the poor prognosis associated with malignant cancers that are resistant to other types of non-radioactive therapy. That being said, such is the strong relationship between metals and the skeleton, that inorganic drugs are continually being explored as therapies for metastatic bone cancer.

1.4 Treatments and therapies for osteoporosis

1.4.1 Osteoporosis

As stated briefly at the beginning of this chapter, one of the most common diseases of the skeleton is osteoporosis. The disease predominantly impacts women who have reached menopause; however, osteoporotic type symptoms can arise from a number of factors such as malnutrition, hormonal imbalance, or adverse drug reactions. The disease is characterized by low bone mineral density (Figure 1.5), and occurs when osseous tissue is resorbed faster than it is being rebuilt, leading to bones that are highly susceptible to damage and fracture. The most common sites of fracture are the hip, spine, wrist or shoulder, and one of the most alarming characteristics of osteoporosis is the tendency for sufferers to be asymptomatic until a serious fracture occurs – a phenomenon that has led to osteoporosis being dubbed “the silent thief.”

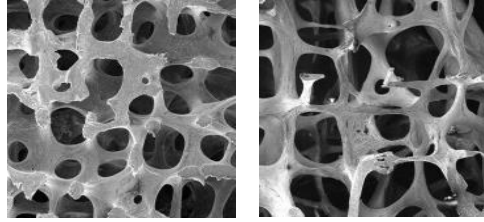


Figure 1.5 A comparison healthy bone (left) and osteoporotic bone with low mineral density (right).²⁹

Although osteoporosis can happen at any age, it predominately affects the elderly, with 1 in 3 women and 1 in 5 men over the age 50 likely to suffer an osteoporotic fracture.²⁹ There is a clear cost to the individual, manifested in pain, disfigurement, reduced mobility, and loss of independence, as well as a significant cost to healthcare systems, with an estimated \$2.3 billion per year since 2010 spent by Canadian healthcare on treating osteoporosis and related fractures.²⁹ Undoubtedly, as the population ages, this cost will continue to rise.

1.4.2 Prevention and treatment

No one single cause has been identified for osteoporosis; however, there are several risk factors that have been recognized and are easily targeted in the prevention of bone mineral loss throughout one's lifetime, including maintaining a healthy diet, exposure to sunlight, regular physical activity, minimizing alcohol intake, and eliminating smoking.³⁰ These factors are also the first line of defense in treating osteoporosis, preferential to pharmacological intervention or hormonal replacement therapy, with certain aspects known to improve bone mass such as calcium and vitamin D dietary supplementation, or specific weight-bearing exercises.³¹

For women who have reached menopause, the risk of developing osteoporosis is more prevalent due to diminished estrogen levels. The result of this hormonal alteration is a substantial

increase in the overall rate of bone turnover; however, in spite of a rise in both formation and resorption rates, the latter dominates, resulting in a net loss of bone mineral.³² Consequently, therapies such as estrogen replacement and selective estrogen receptor modulators (SERMs) are often used to treat postmenopausal osteoporosis. Other approved hormonal therapies include calcitonin and teriparatide, which target parathyroid hormone-modulated serum calcium levels, and have been shown to be effective in reducing fracture rates in osteoporosis sufferers.³³ The drawbacks associated with these types of therapies are varied and significant, including increased risk of stroke, breast cancer, pulmonary embolism, and dementia.^{33,34} Physiological responses to a disruption in natural hormonal balance also vary from person to person, so quantifying these risks is often challenging.

1.4.3 Bisphosphonates

Bisphosphonates (BPs) have been of extreme importance in the development of medicinal agents for treating a number of bone diseases. In living systems, they have the ability to target osseous tissue with very high specificity by mimicking the pyrophosphate network in the HAP-like mineral matrix of bone mineral (Figure 1.6), and by including BP moieties into molecular designs they have been applied as delivery systems for anti-cancer agents, antimicrobials, and various functional proteins.³⁵



Figure 1.6 Structure of the pyrophosphate (left) moiety found in living systems and bisphosphonate (right), incorporated in molecular structures to act as a bone-seeking agent.

In themselves, BPs have the ability to suppress bone resorption due to preferential binding at remodeling sites and the prevention of osteoclastic differentiation *via* various enzymatic pathways.³⁶ This restores balance to a disrupted remodeling cycle, allowing bone mineral to be preserved and replenished which in turn can reduce the risk of osteoporotic fractures. Their potency, bone binding strength, bone distribution, and clearance can be fine-tuned through R group modification, and in Canada there are currently three approved and routinely prescribed BP-containing drugs for treating osteoporosis: alendronate, risedronate, and zoledronate (ibandronate is also approved in the US).³⁷ There are some structural similarities between all these drugs (Figure 1.7): one of their side chains is an OH group, which greatly enhances bone binding ability;^{35,38} and the other side chain's functionality contains a nitrogen, which enhances their inhibitory effect towards osteoclasts, thereby increasing their potency.^{37,38}

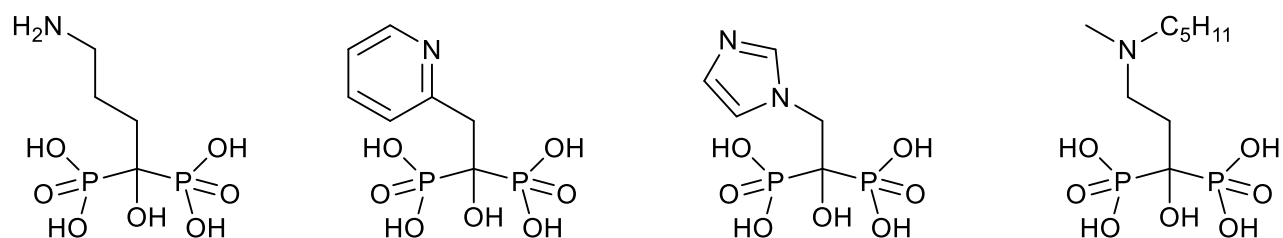


Figure 1.7 The structures of four approved bisphosphonates for the treatment of osteoporosis (from left to right): alendronate; risedronate; zoledronate; ibandronate.

For the most part, BPs are administered orally in order to aid patient acceptance and reduce clinical costs; however, BPs have extremely poor oral bioavailability due to low intestinal absorption, and in order to circumvent this orally administered BP drugs require very high dosing levels relative to intravenous. For context, alendronate – one of the most extensively studied BPs

– is dosed at either 10 mg per day or 70 mg per week for patients suffering from osteoporosis, compared to zoledronate which requires a single annual intravenous dose of 4 mg in order to be effective.^{38,39} As a result, there are a number of quite intense and stringent guidelines for taking oral BPs aimed at minimizing gastrointestinal (GI) upset and to circumvent slow traverse of the drug through the GI tract. These include an overnight fast prior to taking the drug, and remaining standing for at least 30 minutes after a dose, a potentially arduous task for someone suffering from osteoporosis. Because of these guidelines, oral BPs are regularly met with poor patient compliance, for reasons including GI upset and nausea, and severe musculoskeletal pain.⁴⁰

Of greater concern for those prescribed BPs are the potential long-term side effects that have been associated with their use. These include osteonecrosis of the jaw, esophageal cancer, atypical femur fractures, and atrial fibrillation.⁴⁰ In addition, their long term efficacy has been called into question, with a number of reports suggesting that after prolonged use they are no longer effective in preserving bone mineral density, but still allow for all the risks of possible side-effects.⁴¹

1.4.4 Strontium ranelate

Marketed as Protelos®, the strontium(II) salt of ranelic acid (Figure 1.8) is an example of an inorganic drug that has been approved for the treatment of osteoporosis. Strontium is a group II metal, and as such exhibits a strong affinity for calcium sites *in vivo*, rapidly accumulating in the HAP-like bone mineral matrix of developing bones after administration.⁴² Through various pathways (some of which are not yet fully understood), strontium has the simultaneous effect of promoting bone formation by osteoblasts, and inhibiting bone resorption by osteoclasts, both of which help to restore perturbations to the bone remodeling cycle caused by osteoporosis.⁴²

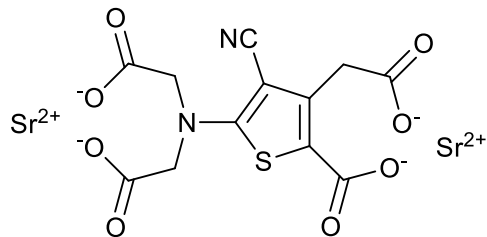


Figure 1.8 The structure of strontium(II) ranelate, an approved drug for the treatment of osteoporosis.

In keeping with the treatments for bone resorption disorders presented thus far, there are significant side effects that have been associated with the use of strontium ranelate. The most prominent of these is a strong link to adverse cardiovascular events, resulting in an increased risk-of-death for those taking the drug, and consequently the prescription of Protelos has been restricted to patients only with severe and established osteoporosis, at high risk of fracture, and with no history of cardiovascular malfunction.⁴³ Additionally there have been a few rare – yet extremely severe – reports of adverse skin reactions to Protelos, including drug rash with eosinophilia and systemic symptoms (DRESS),⁴⁴ and toxic epidermal necrolysis.⁴⁵

As the average age of the population continues to rise (particularly in the developed world), the number of cases of osteoporosis will rise too. Clearly, given the apparent limitations and negative side-effects associated with currently approved treatments, there is a strong precedent for developing alternatives. In this context, an intriguing link between trivalent lanthanum and the bone remodeling cycle has drawn attention from both researchers and drug companies, the details of which will be discussed in the remainder of this introduction, which in turn will reveal the scope for this thesis.

1.5 Lanthanum compounds for osteoporosis

1.5.1 Lanthanum carbonate

The history of the relationship between lanthanum and osteoporosis is a curious one, as it begins with a drug that was intended for a different purpose entirely. Lanthanum carbonate ($\text{La}_2(\text{CO}_3)_3$), patented by Shire Pharmaceuticals and marketed as Fosrenol®, is a routinely prescribed treatment that reduces elevated serum phosphate levels – or hyperphosphatemia – in patients suffering from end-stage renal disease (ESRD). When taken orally, lanthanum acts as a scavenger for excess phosphates in the GI tract that cannot be processed by the kidneys of ESRD sufferers, allowing them to be safely excreted as stable La(III) compounds.

Fosrenol primarily owes its effectiveness to two main principles: firstly, that trivalent lanthanum rapidly and preferentially binds phosphate ligands across a broad pH range;⁴⁶ secondly, that the absolute oral bioavailability of La(III) is extremely low – estimated to be as low as 0.0012% – which allows for safe chronic administration with minimal concern for intestinal absorption and subsequent bioaccumulation.⁴⁷ This is certainly preferential to other phosphate binders such as aluminum or calcium salts, which are more readily absorbed in the gut and carry with them a number of proven toxic side-effects.⁴⁸⁻⁵⁰

With that being said, since lanthanum is a non-essential rare-earth element, and little was known about its toxicity at the time of Fosrenol's approval, much of the concern surrounding the drug was focused on the fate of the lanthanum that was minimally – but demonstrably – absorbed.⁵⁰ Not surprisingly, given the aforementioned similarity in biochemical and biophysical characteristics between La(III) and Ca(II) (Chapter 1.2), uptake and retention in bone tissue was observed, with evidence that lanthanum readily exchanged with calcium in the mineral matrix, and could persist in osseous tissues for upwards of 3 years.⁵¹

Less predictable was the physiological impact that lanthanum bioaccumulation appeared to have on bone histology, with reports suggesting that – at certain concentrations – a similar effect to strontium ranelate takes place, with the promotion of osteoblast differentiation and the suppression of bone resorbing osteoclasts. In principle, this leads to an enhancement in bone formation and bone mineral density, invoking a positive impact on osteoporosis sufferers.⁵²

1.5.2 A question of concentration

Although the initial discovery dates back to 2001,⁵² the evidence that lanthanum could be used in a therapeutic context for treating resorption disorders is, at present, far from conclusive. A 2004 study from Behets *et al.* reported no observed toxicity towards osteoblasts in rats with either chronic renal failure or normal renal function after multiple oral dosing with $\text{La}_2(\text{CO}_3)_3$, but did note abnormal bone mineralization in the group administered with the highest dose (1000 mg kg^{-1} per day).⁵³ In 2008, Wang *et al.* published findings from an *in vitro* study which suggested that osteoblast differentiation was enhanced due to the presence of LaCl_3 ;⁵⁴ however, one year later a report from the same group demonstrated a suppressive effect *in vivo* from the same La(III) source *via* a different pathway.⁵⁵ Various other *in vitro* studies suggest that osteoblastic response to trivalent lanthanide ions is dose-dependent, but out of the context of a living system it is difficult to draw definitive conclusions.⁵⁶

This uncertainty is also emphasized in a 2004 memorandum within the FDA (available as part of the FDA's online Drug Approval Package for Fosrenol)⁵⁷ regarding approval recommendations for $\text{La}_2(\text{CO}_3)_3$, which states: “*Although there are clearly signals that lanthanum could alter bone metabolism, there is insufficient evidence that it does.*” The memorandum highlights this by referencing experiments which show an increase in osteoblastic differentiation

at *in vitro* bath concentrations of $>100 \text{ ng mL}^{-1}$ lanthanum carbonate, but an inhibition in differentiation at concentrations over 5000 ng mL^{-1} . On the other hand, bone formation is activated at concentrations of 5000 to 15000 ng mL^{-1} lanthanum carbonate, suggesting that, although there is a clear dose-dependent metabolic response to the presence of lanthanum ions, it is not as straightforward as a direct impact on the cell groups responsible for building bone. Furthermore, it is difficult to translate these findings into meaningful values which reflect the concentration and distribution of lanthanum ions *in vivo* as a result of oral dosing with $\text{La}_2(\text{CO}_3)_3$.⁵⁷

1.5.3 Increasing bioavailability

In 2012, a study from von Rosenberg and Wehr presented evidence for an improvement in bone composition and formation due to the oral administration of lanthanum carbonate in small animal models with induced post-menopausal osteoporotic-type symptoms (OVX rats).⁵⁸ In this case, the animals were administered $\text{La}_2(\text{CO}_3)_3$ chronically over a 6-month period, and bones were subsequently analyzed for their structure and composition *via* micro-CT, bone-specific biomarkers in serum (osteocalcin), and general bone mass and elemental content relative to a control (untreated) group.⁵⁸ The results corroborated the hypothesis that lanthanum salts could exhibit bone-protecting effects when administered orally; however, it did not address the extremely low intestinal absorption of La(III) as the carbonate. Fosrenol is already known to have adverse effects towards the GI tract,⁵⁹ so presumably elevating the dose as a method to increase the quantity of lanthanum absorbed in order to treat osteoporosis would be met with extremely poor patient compliance.

As previously discussed, properties of metallodrugs such as bioavailability and toxicity are often governed and tuned through the judicious choice of specific chelating ligands.⁶⁰ In this light,

one can rationalize that by modifying the ligand environment around lanthanum to include lipophilic functionalities, a more orally active lanthanum compound could be developed which is effective in enhancing bone formation at lower doses than lanthanum carbonate. This is by no means a novel strategy: platinum(IV)-based compounds modified with lipophilic carboxylate ligands have been explored in the quest for orally-active cancer treatments;⁶¹ *N*-substituted 2-pyridinecarbothioamides were applied to target a similar effect for ruthenium(II) and osmium(II), also in cancer treatment;⁶² and oxovanadium(IV) complexes with maltol and ethylmaltol have been investigated in order to reduce the effective oral dose of vanadium required in the treatment of type-2 diabetes (Figure 1.9).⁶³

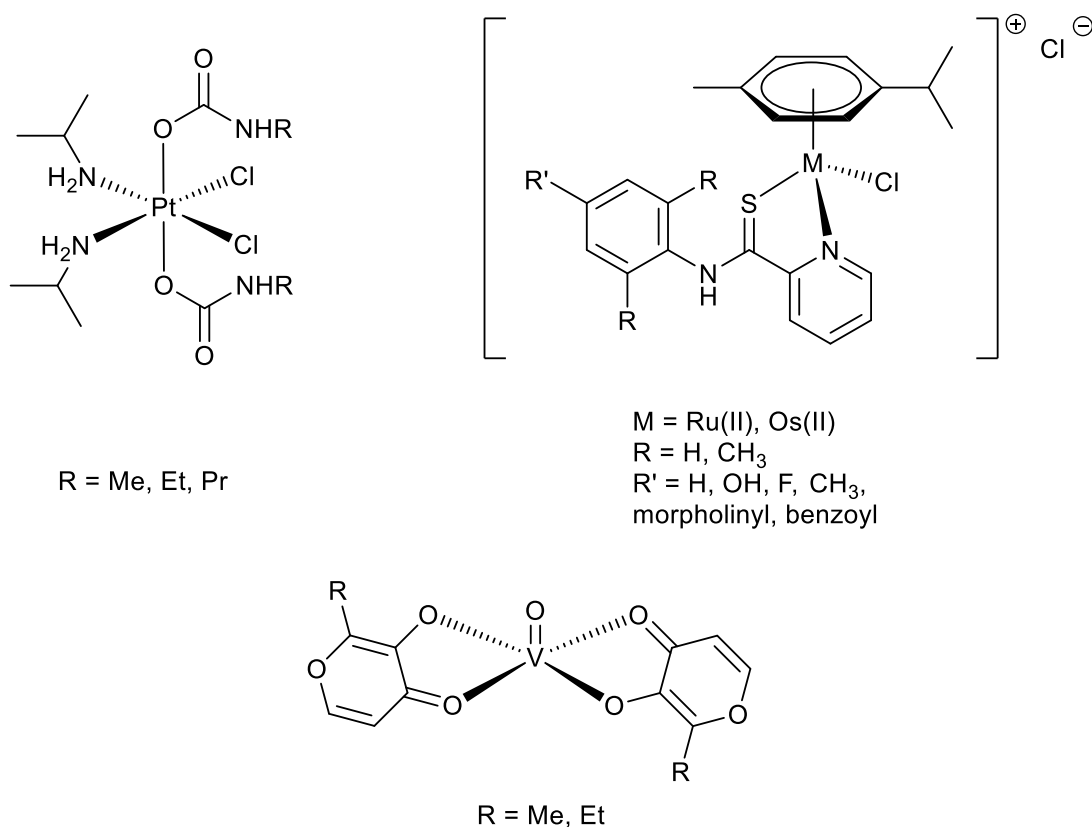


Figure 1.9 Tuning the ligand environment to include more lipophilic functionalities is a strategy that has been used by medicinal chemists in order to improve the oral bioavailability of metal-based drugs.

One method of assessing the oral activity of potential drug targets is through a measurement of the partition coefficient ($\log P$) which is the log of the ratio of distribution of a compound in a biphasic system (usually 1-octanol and water), essentially giving a measure of affinity for a lipophilic environment, which pertains to the ability to cross an intestinal membrane. According to Lipinski's Rule of Five for determining "drug likeness", the ideal $\log P$ range for an orally active compound is between -0.5 and 5;⁶⁴ however, there are an increasing number of examples of drugs which do not conform to these rules.⁶⁵ Certainly for metal-based drugs, in which there is added complexity from metal-ligand interactions, these rules should only guide drug design, rather than dictate it.

An additional concern associated with increasing the oral bioavailability of lanthanum is that of unknown long-term toxicity, which remains a subject of debate amongst biochemists and physicians.^{15,16,47} Even with approved phosphate binders such as lanthanum carbonate, there are research efforts dedicated to further reducing the already minimal absorption of lanthanum in an effort to eliminate any potential risk of toxic side-effects.⁶⁶ With this in mind, an idealized system for targeting bone diseases may only require a marginal increase in bioavailability relative to lanthanum carbonate.

1.6 Thesis overview

The work presented herein focuses on the design, synthesis, and testing procedures undertaken in the quest for a chelating ligand which increases the oral bioavailability of trivalent lanthanum such that its *potential* to improve bone formation in osteoporosis sufferers can be thoroughly investigated. As well as oral activity, design considerations include synthetic accessibility,

toxicity, and specificity towards bone tissue *in vivo*. The subsequent two chapters are dedicated to expanding on previous work done within the Orvig group, investigating two compounds which emerged as leads after the efforts of two past Ph.D. students: Dr. Cheri Barta and Dr. Yasmin Mawani. The first is the *tris*-La(III) complex of 1,2-dimethyl-3-hydroxypyridin-4-one (La(dpp)₃, Figure 1.10a), which emerged from a series of bidentate pyrone and pyridinone *tris*-complexes as having the most improved uptake relative to La₂(CO₃)₃ in a cell model for GI tract permeability.⁶⁷ The second is the 1:1 La(III) complex with bis-[[bis(carboxymethyl)amino]methyl]phosphinate (H₅XT, Figure 1.10b),⁶⁸ a phosphinate-containing EDTA-type complex with higher inherent denticity than the pyrones or pyridinones, which also exhibited good GI tract permeability and a favourably low cytotoxicity profile.⁶⁹

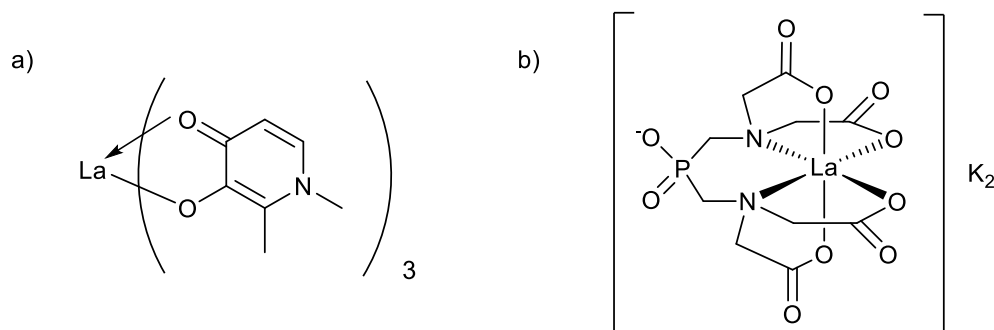


Figure 1.10 The structures of two compounds which became leads in the search for an orally active lanthanum complex for treating osteoporosis: a) La(dpp)₃; and b) K₂[La(XT)].⁶⁷⁻⁶⁹

Chapter 2 examines how these systems interact with bone by applying synthetic hydroxyapatite as an *ex vivo* model for mineralized osseous tissue. Chapter 3 describes preliminary preclinical studies using small animal models to investigate lanthanum biodistribution, as well as spatially resolved distribution within bone tissue itself.

In the fourth chapter of this thesis a new ligand design is presented based on a dipicolinic (dpa) binding motif, which aims to incorporate tunable functionalities as well as desirable attributes from both the previous lead systems. The full synthesis and characterization of this new family of chelating ligands is presented, as well as the La(III) complexes, and preliminary testing protocols to probe lipophilicity and bone binding properties. Finally, in chapter 5, ongoing work and conclusions will be discussed.

Chapter 2: Thermodynamic and kinetic investigations into the interaction between two lead compounds – La(dpp)₃ and La(XT) – and hydroxyapatite

2.1 Introduction to previous work

2.1.1 Hydroxypyrones and hydroxypyridinones

The family of small, 6-membered, *O*- and *N*-heterocyclic compounds, known respectively as the pyrones and the pyridinones, have been extensively studied for a range of applications due to their synthetic accessibility, ease of functionalization, and favourably low toxicity profiles. In an inorganic context, the 3-hydroxy-4-pyrones and -pyridinones are of particular interest due to the *O,O*-bidentate metal binding environment present in the form of an electron-rich ketone and an ortho hydroxyl group (Figure 2.1), and in their deprotonated form they form stable neutral *bis*- and *tris*-complexes with a number of divalent and trivalent metal cations.⁷⁰ Some of these complexes have been explored for their potential applications in medicine, examples including the use of 3-hydroxy-4-pyridinones to bind aluminum(III) in the reduction of Alzheimer's-related Al toxicity;⁷¹ similar compounds of gallium(III) and indium(III) for PET and SPECT imaging;⁷² the incorporation of hydroxypyridonates into multidentate macro-ligands for targeting thermodynamically stable gadolinium(III) MRI contrast agents;⁷³ and the aforementioned lipophilic pyrone complexes of oxovanadium(IV) for treating type-2 diabetes.⁶³

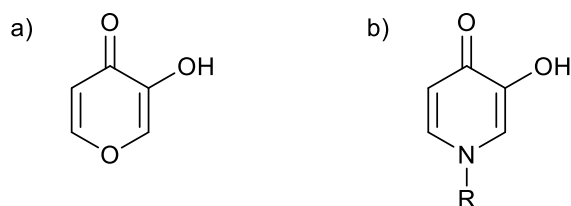


Figure 2.1 General structure of a) 3-hydroxy-4-pyrone and b) 3-hydroxy-4-pyridinone, metal complexes of which have been explored for a number of medical applications.⁷⁰

Prior to the work of Dr. Cheri Barta (Ph.D. 2007, Medicinal Inorganic Chemistry Group, University of British Columbia), *tris*-Ln complexes with various pyrones and pyridinones had been explored, both out of fundamental interest and for biological applications.⁷⁴ Inspired in part by the success of applying 2-alkylated pyrones to improve the oral uptake of oxovanadium compounds, the *tris*-Ln complexes of 2-methyl-3-hydroxy-4-pyrone (Hma), 2-ethyl-3-hydroxy-4-pyrone (Hema), 2-methyl-3-hydroxy-4(1*H*)-pyridinone (Hmpp), and 1,2-dimethyl-3-hydroxy-4-pyridinone (Hdpp) were synthesized, fully characterized, and put through a series of preliminary tests to assess their potential as orally active agents for treating osteoporosis, including cytotoxicity *via* MTT assay; cell uptake and bifunctional transport with Caco-2 cells; and *in vitro* hydroxyapatite binding, a bone-binding model which formed the basis for the experiments discussed later in this chapter.⁶⁷

Up to this point, and owing primarily to investigations into Fosrenol, research on this potential therapy for bone disorders had been limited to lanthanum; however, it was postulated that since the lanthanides share a number of similar chemical and physical characteristics, an alternative 4f element could produce equal or superior results in stimulating the building of bone. That being said, it was the *tris*-La³⁺ complex of Hdpp (La(dpp)₃, Figure 1.10 a) which produced the most significant result in Dr. Barta's work as the only complex to exhibit an increase in metal ion uptake in Caco-2 cells relative to lanthanum carbonate and compared to other compounds tested (Figure 2.2), implying an improvement in oral bioavailability. This result – combined with low cytotoxicity and no apparent impedance of La binding to HAP due to the ligand system – rendered La(dpp)₃ the lead compound from this work.

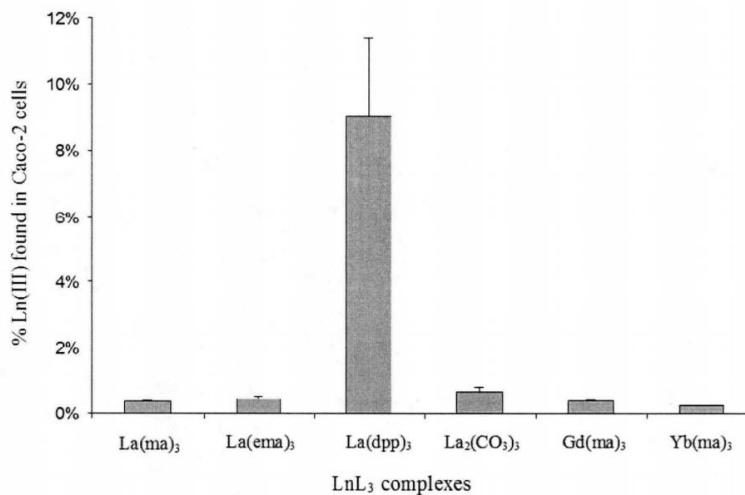


Figure 2.2 Cell uptake in Caco-2 cells of LnL₃ determined by ICP-MS. La(dpp)₃ is the only system to exhibit greater uptake than La₂(CO₃)₃ (Fosrenol). Reproduced from reference 67.

2.1.2 La(XT): Towards higher denticity

Chelating ligands with high inherent denticity (>4) usually invoke a greater thermodynamic stability of their metal complexes compared to low denticity (1-3) alternatives. Considering the prolonged exposure to warm temperatures and variable pH levels an orally delivered drug must be able to tolerate – as well as the presence of numerous other endogenous competing metal-binding groups – there is considerable logic to selecting chelators with greater denticity than the hydroxypyridinones in the context of this project.

In 2001, L. Xu *et al.* probed the chemistry of bis-[[bis(carboxymethyl) amino]methyl]phosphinate (dubbed “H₅XT” in reference to the researchers that performed these studies) with a series of lanthanides.⁶⁸ The ligand contains a phosphinate moiety symmetrically flanked by two bis-carboxylic acid functionalized tertiary amines, invoking a 7-coordinate binding geometry when fully bound to a metal centre. It was found that H₅XT forms fully coordinated

complexes with a number of Ln^{3+} ions, all bearing close structural resemblances to one another across the series (according to IR spectroscopy), and with a slightly improved complex stability compared to EDTA (the non-phosphinate-containing equivalent).⁶⁸ Therefore, in the work of Dr. Yasmin Mawani (Ph.D. 2012, Medicinal Inorganic Chemistry Group, University of British Columbia), the lanthanum, europium, and lutetium complexes of H_5XT were compared alongside a series of functionalized 3-hydroxy-4-pyridinones in order to assess the virtue of higher denticity ligands for the oral delivery of Ln(III) .⁶⁹

At this stage, Dr. Mawani also aimed to fine-tune the 3-hydroxy-4-pyridinone ligand motif by adding functionality to the *N*-position of the heterocycle, including lengthening the alkyl chains in order to further increase lipophilicity and GI uptake, and incorporating phosphonate and bisphosphonate moieties with the aim of enhancing bone targeting.⁶⁹ This rationale for improving tissue specificity also served to supplement the argument for including H_5XT in these studies, which contains the potentially bone-directing phosphinate moiety. As was emphasized with EDTMP and MDP (Chapter 1.3), ligand functionality can play a big role in directing a metal ion to an intended target organ.

In a similar cell uptake study to that performed by Dr. Barta, it was found that the dianionic La(III) complex of H_5XT ($\text{K}_2[\text{La(XT)}]$, Figure 1.10b) exhibited the greatest lanthanum uptake compared to a number of *tris*- La(III) hydroxypyridinones, which was attributed to the thermodynamic stability of La(XT) under physiological conditions (Figure 2.3).⁶⁹ Although the experiments did not directly compare La(dpp)_3 and $\text{La}_2(\text{CO}_3)_3$ with La(XT) , the result was considered significant due to the clear improvement in cellular uptake of the 1:1 heptadentate system relative to all the bidentate ligands tested. Additionally, HAP binding studies and low

cytotoxicity all contributed to a strong case for including La(XT) as a second lead compound for further studies alongside La(dpp)₃.

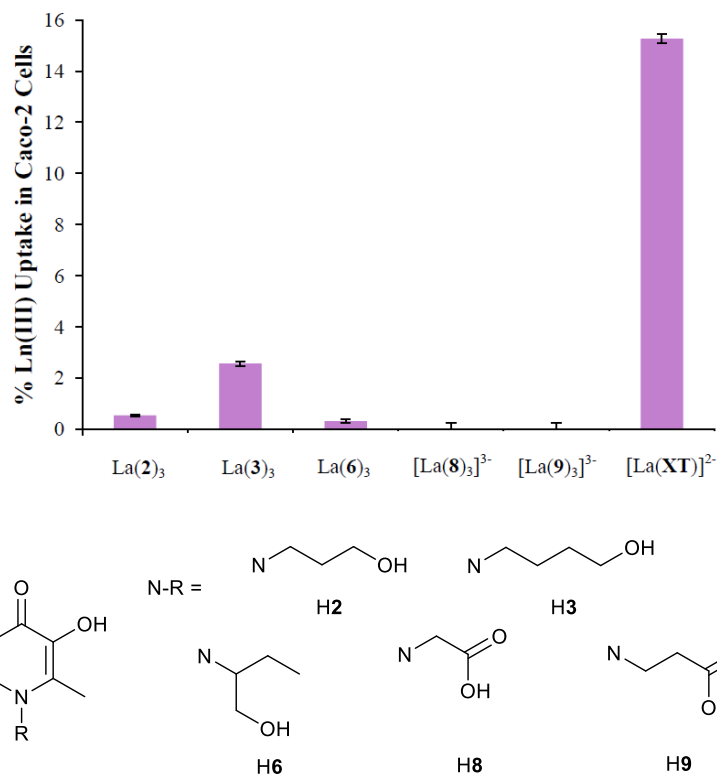


Figure 2.3 Cell uptake of La(III) in Caco-2 cells in the presence of various ligand systems, as measured by ICP-MS. La(XT)²⁻ shows the greatest uptake, corresponding to the highest GI tract absorption. Reproduced from reference 69.

Studies utilizing HAP as an *in vitro* model for bone mineral binding were performed by Dr. Barta and Dr. Mawani for La(dpp)₃ and La(XT) respectively;^{67,69} however, these studies were – for the most part – rudimentary and qualitative, and did not offer a direct comparison of the two lead compounds within the same set of experiments. For the remainder of this chapter we present two studies which probe the thermodynamics and kinetics between La(dpp)₃ or La(XT) and HAP, in an effort to better understand how the ligand environment impacts lanthanum’s interaction with bone mineral. Also included is an updated synthetic procedure for the two lead compounds which

reflect the multigram quantities required to perform multiple *in vitro* and *in vivo* studies, as well as a crystal structure for $\text{La}(\text{dpp})_3$ which had not been previously obtained.

2.2 Thermodynamic and kinetic studies with HAP

2.2.1 Isothermal titration calorimetry of La^{3+} complexes with HAP

Understanding the interactions between biological molecules and potential drugs is fundamental to predicting their behaviour *in vivo*. The thermodynamic parameters which govern these interactions are highly dependent on a number of physical aspects of both the system under scrutiny and its environment. In this regard, isothermal titration calorimetry (ITC) offers one of the most powerful techniques available as it allows direct control of temperature, pH, ionic strength, and analyte concentration. It has proven critical in quantifying the strength and specificity of drug/target interfaces, thereby improving our knowledge of how and why these systems interact in the way that they do.⁷⁵

The principles of ITC have been reviewed extensively in the literature.^{75,76} Briefly, one species (e.g. a potential drug molecule) is titrated in small, precise aliquots into another species (e.g. the intended biological target of the drug) in a reaction cell buffered to a specific pH. When the two mix (aided by rapid mechanical stirring), heat is either given off or taken in, depending on whether there is an exothermic or an endothermic interaction between the two species. The subsequent change in heat associated with maintaining the reaction cell at thermal equilibrium is then measured with respect to a reference cell held within the same adiabatic jacket. This allows direct determination of a number of thermodynamic parameters, including enthalpy change (ΔH), apparent equilibrium constant of association (K_{app}), and the stoichiometric ratio of the two binding species (n). Furthermore, entropy change (ΔS) can be estimated by non-linear regressive curve

fitting, and the Gibbs free energy (ΔG) can be extrapolated from a straightforward thermodynamic relationship (Equation 2.1).

$$\Delta G = \Delta G^\circ + RT \ln K_{\text{app}} = \Delta H - T\Delta S \quad (\text{Equation 2.1})$$

ITC measurements between a number of lanthanide cations and HAP in the absence of a ligand system have been previously reported by our group.¹¹ For all Ln^{3+} tested, the results showed a thermodynamically favourable association between the metal ion and HAP at 37 °C, indicated by negative values (measured in kcal per mole of titrant) for ΔH and ΔG , positive values for $T\Delta S$, and large values of K_{app} (in the order of 10^6). For La^{3+} (Figure 2.4), the stoichiometric binding ratio was found to be approximately 2.4, indicative of the number of binding sites available for the metal ion per formula unit of HAP ($\text{Ca}_5(\text{PO}_4)_3\text{OH}$). Crucially, HAP that was extracted from the ITC cell post-titration was found to be isomorphous with untreated HAP (by solid state ^{31}P NMR and powder X-ray diffraction), implying that binding site saturation with a guest lanthanide ion does not appreciably alter the physical structure of the bone mineral model.¹¹ This is in keeping with previously reported findings that lanthanum can undergo isomorphous exchange with calcium in HAP (see Chapter 1.2).

In an effort to understand the effect of a complexed ligand system on the now well-established binding interaction between La^{3+} and HAP, we expanded upon these studies by performing ITC with both the ligands on their own, followed by the metal complexes. The results and discussion for these experiments are presented in section 2.3.2.

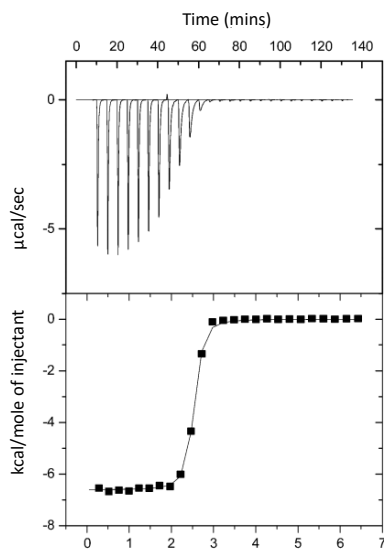


Figure 2.4 The raw ITC plot (upper) of La^{3+} (10 μL injections, 3.15 mM) into HAP (0.1 mM) at pH 5.0 (100 mM piperazine) and 37 °C, and the integrated data (lower) giving $n = 2.4(1)$; $K_{\text{app}} = 2.4(2) \times 10^6$; $\Delta H = -6.61(8)$ kcal/mol; $T\Delta S = 2.45$ kcal/mol; $\Delta G = -9.06$ kcal/mol. Reproduced from reference 11.

2.2.2 Solution depletion kinetics with La^{3+} complexes and HAP

As previously described, in a system containing free La^{3+} ions and HAP (a synthetic model for bone mineral), the guest ion can – under the correct conditions – adsorb onto the mineral surface and undergo isomorphous cationic exchange with Ca^{2+} .^{9-11,14} In solution, ITC is invaluable in quantifying the thermodynamic factors which govern this ion exchange (as well as in the presence of our two ligand systems of interest, Hdpp and H_5XT), but it does not provide kinetic data. Consequently, we sought to further probe the nature of these interactions through solution-depletion studies. The principle behind these experiments is simple: lanthanum concentrations in the supernatant of a solution containing a suspension of excess HAP will decrease with time as the metal ion binds to insoluble HAP and exchanges with calcium. Monitoring the unbound $[\text{La}^{3+}]$

over time will provide information on the kinetic parameters which influence this binding event, and can also be performed in the presence of either ligand system to shed light on their effect on metal-HAP binding. Results and discussion are presented in Section 2.3.3. Experiments akin to these were previously performed by Dr. Barta and Dr. Mawani;^{67,69} however; in those cases, the time intervals at which La^{3+} was measured were not of a sufficient frequency to glean useful kinetic information.

2.3 Results and discussion

2.3.1 Crystal structure of $[\text{La}(\text{dpp})_3(\text{H}_2\text{O})_2] \cdot 11.75\text{H}_2\text{O}$

Structural refinement by X-ray crystallography offers one of the most powerful analytical techniques available for molecular characterization in the solid-state, as it enables both clear visualization and quantification of a number of molecular features, such as bond lengths, coordination geometries, and intramolecular interactions. There are a number of literature examples of trivalent metal ions (predominately group 13) complexed with pyrone- and pyridinone-type ligands that have been characterized in this way, including Al^{3+} and Ga^{3+} with Hdpp;⁷⁷ Ga^{3+} with 2-methyl-3-hydroxy-4-pyranthione (thiomaltol);⁷⁸ and In^{3+} with two functionalized maltol derivatives.⁷⁹

In spite of their similarities to group 13 metals, there are only a handful of published examples of Ln^{3+} with this same type of ligand motif which have been characterized in the solid state.⁸⁰ This can be rationalized by the variable coordination numbers and irregular geometries that the lanthanides can adopt, which renders the acquisition of single crystals of an adequate size and quality for crystallographic characterization especially challenging. This difficulty is increased when the chelating ligands do not fully saturate the metal ion's coordination sphere, and in this

light we were very fortunate to obtain single crystals appropriate for X-ray analysis of $\text{La}(\text{dpp})_3$, which were obtained as colourless prisms by the slow diffusion of a methanol solution of lanthanum nitrate into an aqueous solution of Hdpp pre-buffered to pH 8.5 with 1 M KOH at 2 °C.

The structure was solved by direct methods (Dr. Brian Patrick, Department of Chemistry, University of British Columbia). The material crystallized with two water molecules coordinated to the metal centre, and approximately 12 water molecules forming a two-dimensional hydrogen bonded layer between lanthanum complexes (Figure 2.5). A number of the water molecules (O8, O15, O16, O17 and O18) are disordered and were modeled in two positions. All non-hydrogen atoms were refined anisotropically, and O-H hydrogen atoms were located in difference maps and refined isotropically. All other hydrogen atoms were placed in calculated positions.

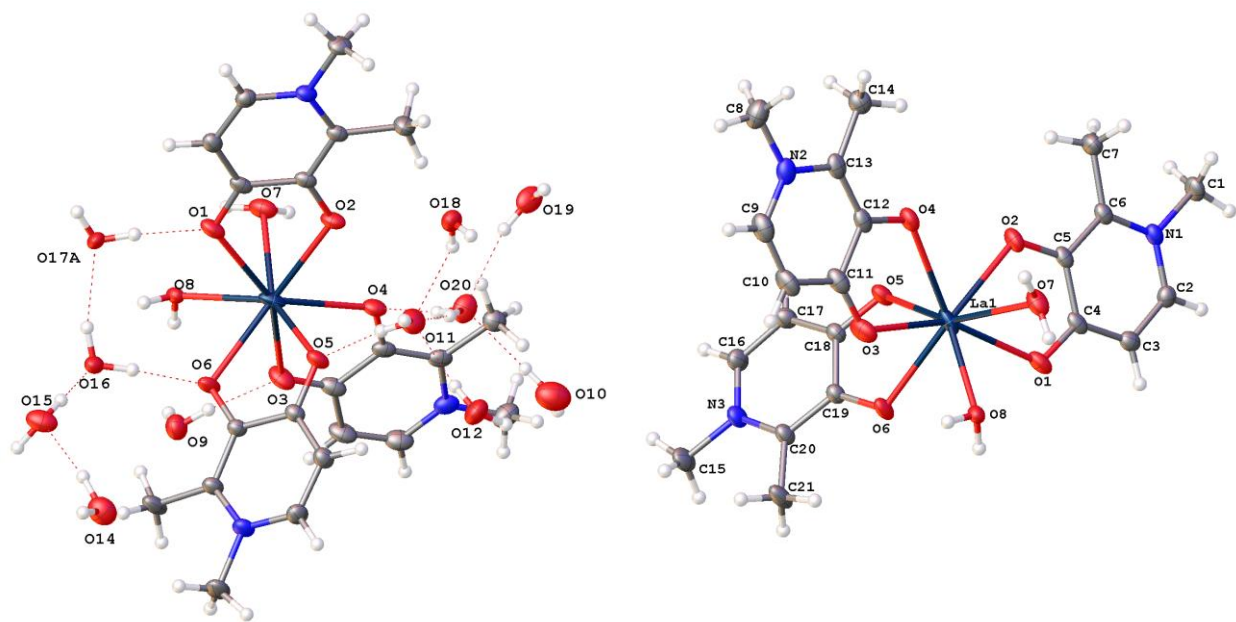


Figure 2.5 ORTEP diagram of the crystal structure of $\text{La}(\text{dpp})_3(\text{H}_2\text{O})_2 \cdot 11.75\text{H}_2\text{O}$ showing the network of hydrogen bonded water molecules (left), and, for clarity, only the water molecules bonded directly to the La^{3+} centre (right).

Interestingly, the solid state structure of Al(dpp)₃ – as well as an isomorphous Ga³⁺ analogue – were both shown to contain an exocathrate-type extended hydrogen bonded network with 12 water molecules per metal complex;⁷⁷ however, in those cases the structures were very highly ordered, allowing much greater precision in atom position refinement than was possible with La(dpp)₃. This is presumably due to the two additional water molecules bonded to the metal centre (not present in 6-coordinate Al or Ga), leading to a distorted 8-coordinate geometry around La and an irregular distribution of water molecules throughout the extended network.

Table 2.1 Crystallographic data.

	La(dpp)₃(H₂O)₂ • 11.75H₂O	
Formula	C ₂₁ H _{51.5} N ₃ O _{19.75} La	
Formula weight	801.06	
Crystal system	Triclinic	
Space group	<i>P</i> -1 (#2)	
Lattice type	Primitive	
Lattice parameters	<i>a</i> = 10.8019(16) Å	<i>α</i> = 73.963(6)°
	<i>b</i> = 11.2323(15) Å	<i>β</i> = 79.565(5)°
	<i>c</i> = 15.296(2) Å	<i>γ</i> = 73.194(4)°
Lattice volume	1697.1(4) Å ³	
<i>Z</i>	2	
<i>D</i> _{calc'd}	1.568 g/cm ³	
<i>F</i> (000)	827.00	
<i>μ</i> (MoKα)	13.40 cm ⁻¹	
Reflections collected	25083	
Unique reflections	9777	
Reflections with <i>I</i> ≥ 2.00σ(<i>I</i>)	8869	
R _{int} ; R ₁ ; wR ₂	0.023; 0.042; 0.080	
GofF on <i>F</i> ²	1.16	

The X-ray crystal structure of La(dpp)₃ presented here provides a unique and informative insight into some intriguing solid-state properties; however, as this compound is intended for use in a pharmaceutical context, it is the solution-based physical and biological properties which will ultimately determine its suitability and effectiveness in its final application. Unfortunately, despite

our best efforts, single crystals of La(XT) suitable for X-ray analysis were not obtained although the Co(II) complex has been characterized crystallographically.⁶⁸

2.3.2 ITC results and discussion

Figure 2.6 shows representative data from ITC analysis of HAP with Hdpp (Figure 2.6 A), La³⁺ in the presence of Hdpp (Figure 2.6 B), H₅XT (Figure 2.6 C), and La³⁺ in the presence of H₅XT (Figure 2.6 D). The plots shown were all performed at pH 5.0 (piperazine buffer) to enable direct comparison to results previously obtained for La³⁺ in the absence of ligand.¹¹ In that instance, the reason for selecting a pH outside of a physiologically relevant range was to prevent the formation of insoluble Ln hydroxides. Titrations with ligand alone and with metal/ligand solutions were also performed at pH 7.4 (HEPES buffer), and a discussion of those results is also included.

There was no evidence of binding between the hydroxypyridinone ligand Hdpp and HAP in the absence of La³⁺ (Figure 2.6 A), indicating no preference for bone tissue targeting at either pH. Titrations of the La³⁺ ion in the presence of Hdpp at pH 5.0 (Figure 2.6 B) shows binding of La³⁺ to HAP through the displacement of Ca²⁺, and the resulting thermodynamic data are very similar to those of the free La³⁺ experiments (Table 2.2). At pH 7.4, a similar plot was recorded but a drop in the apparent binding constant was observed, with $K_{app} = 1.3(3) \times 10^4$, roughly two orders of magnitude less than at pH 5.0.

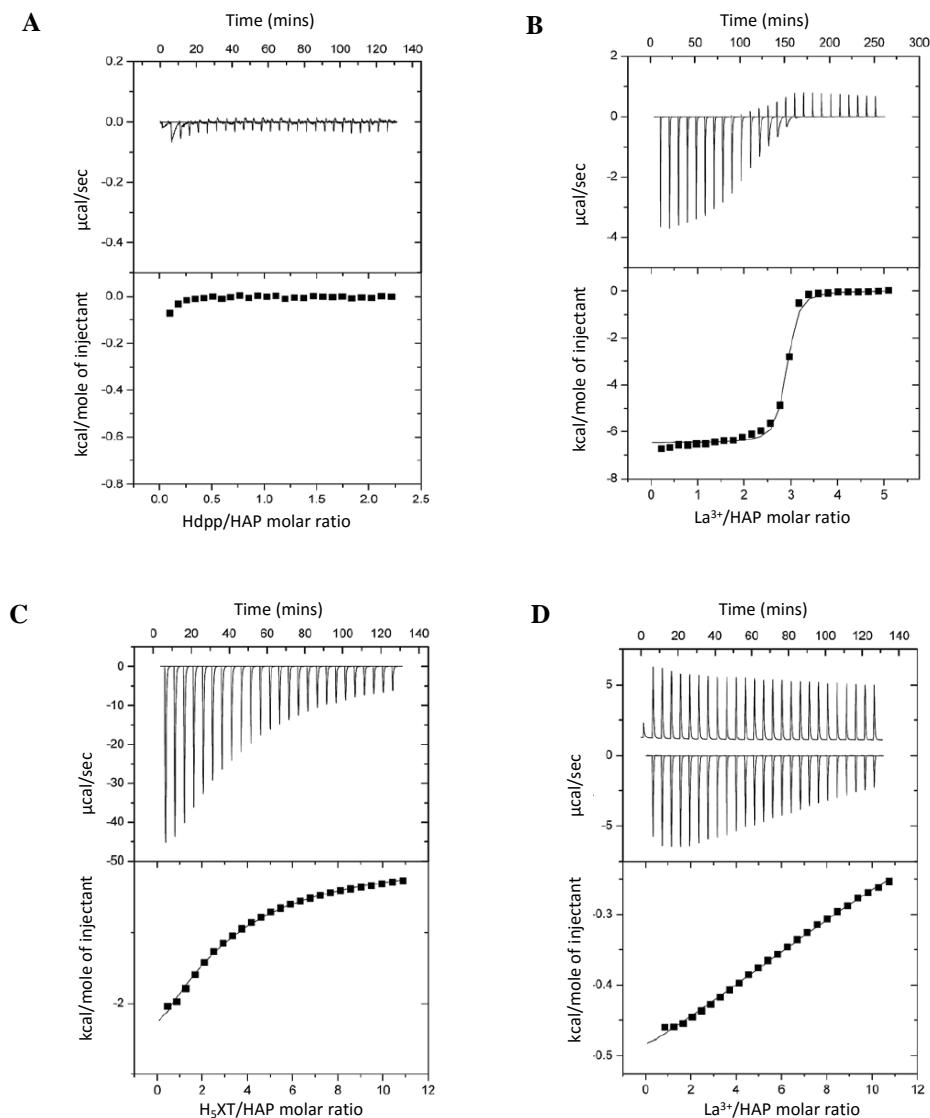


Figure 2.6 Representative data for ITC analysis of ligand and metal/ligand binding to HAP at 37°C, pH 5.0 (100 mM piperazine). **A:** Raw titration data (upper) for 10 μL injections of HdpP (9.8 mM) into HAP (0.9 mM) and the integrated data (lower). **B:** Raw titration data (upper) for 10 μL injections of La^{3+} (2.5 mM) in the presence of HdpP (10 mM) into HAP (0.1 mM) and the integrated data (lower) with best fit line to a one-site bimolecular binding model. **C:** Raw titration data (upper) for 10 μL injections of H_5XT (80 mM) into HAP (1.5 mM) and the integrated data (lower) with best fit line to a one-site bimolecular binding model. **D:** Raw titration data (upper) for 10 μL injections of La^{3+} (80 mM) in the presence of H_5XT (90 mM) into HAP (1.5 mM) and the integrated data (lower).

Table 2.2 Comparison of thermodynamic data from ITC analysis of free La^{3+} (from Reference 11) and La^{3+} with Hdpp measured at 37 °C and pH 5.0.

Species	K_{app} ($\times 10^6$)	ΔG (kcal/mol)	ΔH (kcal/mol)	ΔS (kcal/mol)
La^{3+}	2.4(2)	-9.06	-6.61	2.45
$\text{La}^{3+} + \text{Hdpp}$	1.7(4)	-8.84	-6.42	2.42

A preliminary interpretation of these data could be to argue that the complexation of La^{3+} to Hdpp does not hinder the natural tendency for the metal ion to bind to bone; however, examination of the speciation of La^{3+} and Hdpp under ITC titration solution conditions facilitates understanding of the observed binding events: the species composition of the solution within the ITC syringe (2.5 mM La^{3+} , 10 mM Hdpp) at pH 5.0 shows that approximately 35% of lanthanum exists as the free La^{3+} ion, 60% is in the form of $[\text{La}(\text{dpp})]^{2+}$ and less than 5% is $[\text{La}(\text{dpp})_2]^+$ (Figure 2.7a). Following the first 10 μL injection of titrant, over 95% of the La^{3+} then exists as the free ion within the ITC cell, with $[\text{La}(\text{dpp})]^{2+}$ comprising the small remaining fraction (Figure 2.7b). Over the course of the titration this distribution within the cell gradually shifts to approximately 75% free La^{3+} . Therefore, at pH 5.0, differential heats recorded in each titration essentially represent free La^{3+} binding to HAP, and hence the similarities in thermodynamic data recorded for free La^{3+} .

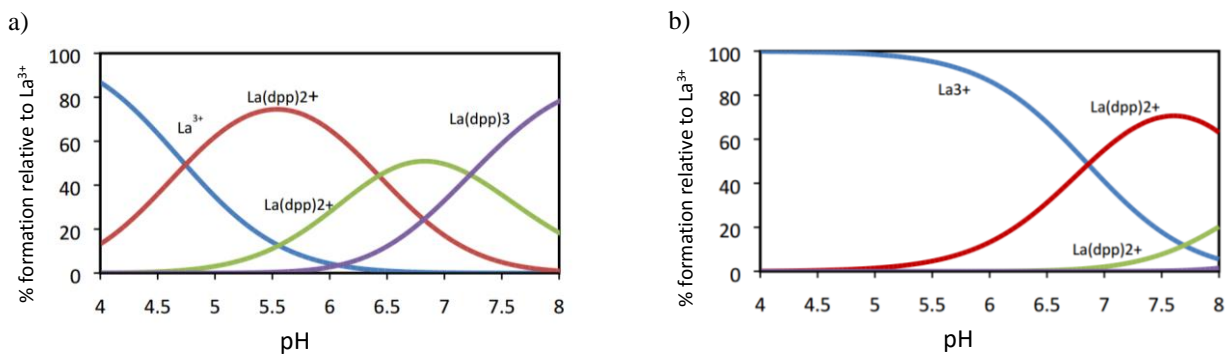


Figure 2.7 Speciation plots for typical ITC conditions for a) syringe concentrations (2.5 mM La³⁺ and 10 mM Hdpp) and b) conditions in the reaction cell after the first injection (0.018 mM La³⁺ and 0.071 mM Hdpp).

At pH 7.4, conditions within the titration syringe mimic much more closely the desired 3:1 system, with approximately 50% of the metal ion existing as La(dpp)₃, 40% as [La(dpp)₂]⁺, and less than 10% as [La(dpp)]²⁺; however, once in the reaction cell (first injection), the conditions are such that the majority of the metal ion exists in the 1:1 form [La(dpp)]²⁺. This phenomenon can be used to explain the apparent drop in K_{app} at the higher pH, as La³⁺ must now overcome the added energetic barrier of shedding the dpp⁻ ligand before it can bind to HAP. Furthermore, as free La³⁺ binds to HAP precipitate, it is essentially being removed from the solution, causing the equilibrium within the cell to favour the formation of free La³⁺ rather than a metal-ligand complex (according to Le Chatelier's principle), and in turn more metal ion binds to HAP.

In contrast to Hdpp, the phosphinate-ETDA derivative H₅XT was found to bind HAP in the absence of La³⁺ at pH 5.0 (Figure 2.6 C) with an apparent binding constant $K_{app} = 1.9(4) \times 10^2$. In the presence of this ligand, binding of La³⁺ to HAP is also observed at pH 5.0, but it is significantly weaker in nature (Figure 2.6 D). Regrettably, in this case, the complex contributions from background binding of the ligand to HAP – as well as the heat of dilution of the ion-loaded

ligand (upper plot in Figure 2.6 **D**) – confounded efforts to regress a K_{app} value for La^{3+} absorption onto HAP in this system.

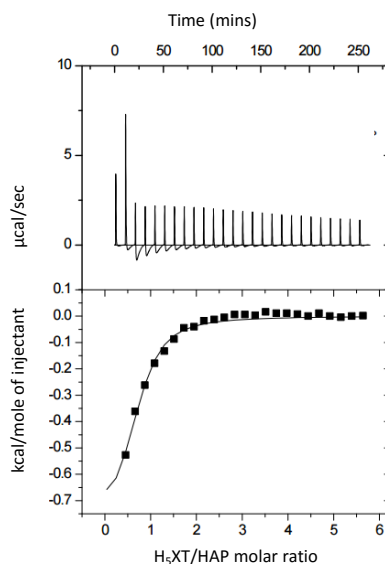


Figure 2.8 ITC analysis data of H₅XT into HAP at 37°C, pH 7.4 (100 mM HEPES). Raw titration data (upper) for 10 µL injections of H₅XT (30.4 mM) into HAP (1.1 mM) and the integrated data (lower) fitted to a one-site bimolecular binding model.

Similar results were obtained at pH 7.4, with the added complication that the binding was considerably slower (resulting in significant titration peak broadening) and, for the case of binding of the H₅XT ligand alone, each titration exhibited an initial endothermic process followed by a slow exothermic event (Figure 2.8). Complex binding of multidentate anionic ligands has been observed before, as evidenced by a 2-site model which has been previously postulated for the binding of bisphosphonates to bone mineral at pH 7.⁸¹ That system is thought to be comprised of a weak, highly populated site where a phosphonate binds into the mineral matrix, and a second higher affinity binding site. Binding at the weaker site results in displacement of one phosphonate

group per molecule, with the energy required to release that group contributing to the binding free energy.⁸¹ For H₅XT, binding to HAP observed by ITC is complex, but relatively weak at pH 5.0, and therefore more consistent with the characteristic of the weaker site described above. As with weak binding phosphonates, H₅XT uptake is therefore likely confounded by relatively high rates of desorption.

Whilst the complex energy landscape of the control experiments prevented the accurate determination of K_{app} value, evidence for weak ion binding of La³⁺ to HAP in the presence of H₅XT was nonetheless observed at pH 5.0 by ITC (lower plot in Figure 2.6 D). Again, one can turn to the speciation plots for explanation (Figure 2.9). The plot shows that no significant fraction of the added lanthanum exists as free metal ion either in the ITC syringe or in the reaction cell at any point during the titration. La³⁺ binding to HAP must therefore overcome the energy required both to shed the XT ligand and to displace a Ca²⁺ bound within HAP. The binding strength of the 1:1 La(XT)²⁻ complex is approximately 5 to 6 orders of magnitude greater than the corresponding La(dpp)²⁺ complex,^{68,69} and as a result the net La³⁺ binding interaction with HAP is expected to be considerably (on the order of 10⁵ times) weaker than that observed for the La³⁺ + Hdpp system. This is in accordance with the very weak binding differential data reported in Figure 2.6 B and Figure 2.6 D.

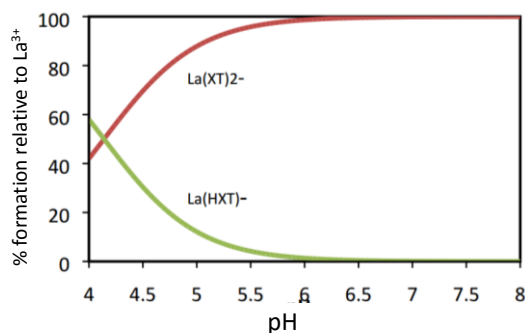


Figure 2.9 Speciation plots for typical ITC conditions in the reaction cell over the course of a single experiment.

The ITC studies, while emphasizing the complexity of the systems under scrutiny, do provide an insight into the manner in which these two complexes could behave *in vivo*. The data clearly show that Hdpp has no affinity for HAP and – due to the thermodynamic stability of the *tris*-complex – readily releases the metal ion under physiological conditions. Conversely, H₅XT incorporates functionality which both provides greater thermodynamic stability of the metal complex, and possesses its own weak affinity for bone mineral as evidenced by ITC.

At this point it is worth stressing that – while clearly a useful technique – ITC has a number of limitations which should be mentioned, particularly in the context of the systems under scrutiny. First is that ITC applies a one-site bimolecular binding model (i.e. a single substrate molecule for a single binding site forming a single overall macromolecule), which is clearly an oversimplification for both La(dpp)₃ and La(XT) with HAP (and the reason why the calculated binding constant *K* is considered “apparent”). Second is the complication that arises from the use of an insoluble mineral (HAP) in the ITC reaction cell, which implies numerous additional variables – such as particle surface area and homogeneity – adding further complexity to the model. Overall, a considerate approach should be taken when applying the above ITC data as a platform for both predicting and interpreting the results of the experiments in living systems (Chapter 3).

2.3.3 Results and discussion for solution depletion studies

Figure 2.10 shows the results of the depletion of La³⁺ ions in solution as the metal binds to HAP in the presence of either Hdpp (Figure 2.10 **A**) or H₅XT (Figure 2.10 **B**) over a 24-hour time period. Also included in the plot for the La(dpp)₃ is the concentration of ligand in solution as measured by UV-Vis spectrometry.

In the case of $\text{La}(\text{dpp})_3$, the data show that the ligand remains unbound while the metal rapidly binds to HAP (less than 20% remaining in solution after the first 15 minutes). This supports the ITC data that shows that only the metal ion exhibits affinity for HAP, and is in keeping with the notion that $\text{La}(\text{dpp})_3$ does not remain as the *tris*-metal complex in solution. In the case of $\text{La}(\text{XT})$, the ICP-MS data show less than 20% of La^{3+} is bound to HAP after 4h, and the La^{3+} sorption process is considerably slower than recorded for the corresponding $\text{La}(\text{dpp})_3$ system. Both findings are consistent with the much higher thermodynamic stability of $\text{La}(\text{XT})^{2-}$ complex (relative to the dominant $\text{La}(\text{dpp})^{2+}$ complex) as was elucidated in ITC studies. Unfortunately, the distribution of H_5XT could not be followed by UV-Vis spectroscopy due to the absence of a chromophore within the ligand.

In an effort to elucidate the rate constants for the binding of La^{3+} to HAP in the presence of either ligand system, the experiment was repeated with multiple measurements taken within the first few time points. It is worth noting that – in the initial 24 h experiments – there were features of both plots which prevented extraction of these values including large error values ($\text{La}(\text{dpp})_3$) and confounding data points ($\text{La}(\text{XT})$). The results for the early time points are shown in Figure 2.11, and shed some light on why these anomalies may exist. The data show that, in the presence of both Hdpp (Figure 2.11 **A**) and H_5XT (Figure 2.11 **B**), there is an initial, rapid association of La^{3+} within the first 30 seconds, followed by a redistribution and a steadier binding consistent with the kinetics of the later time points. This pattern exists, to different extents, for both ligand systems, suggesting that there are (at least) two overlapping kinetic processes occurring which are independent of the ligand present. While this hinders the realization of meaningful rate constant values, the less pronounced La^{3+} fluctuation in the case of H_5XT compared to Hdpp is again

consistent with a ligand system that binds the metal more tightly, allowing fewer ions to bind to HAP.

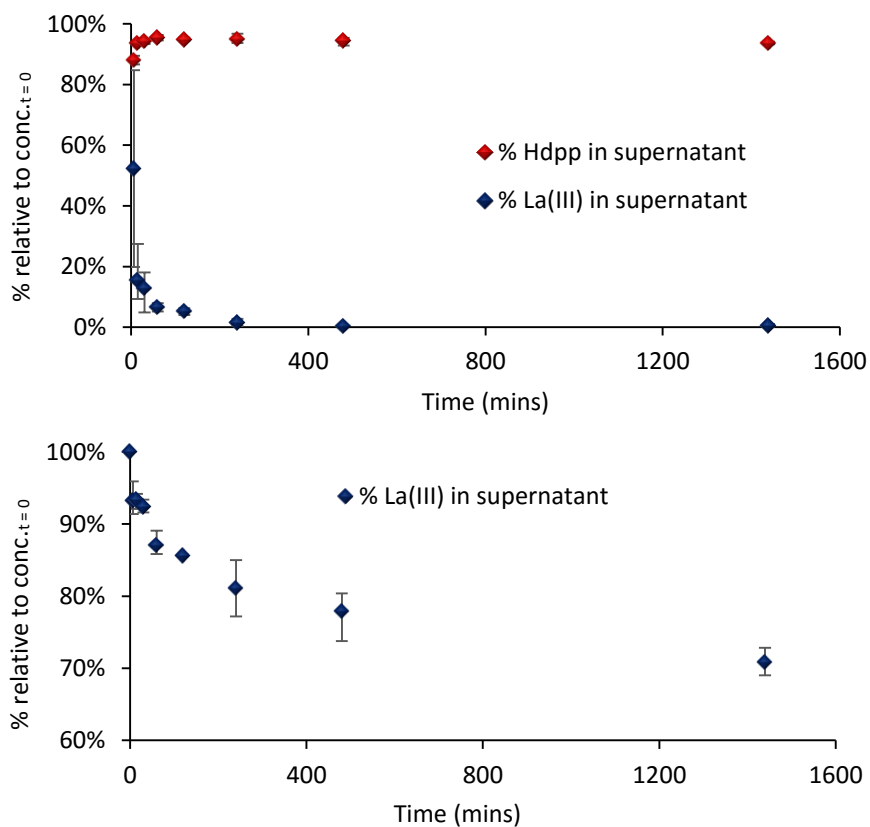


Figure 2.10 The depletion of La^{3+} over 24 hours measured in solution by ICP-MS at 37 °C and pH 7.4 (100 mM HEPES buffer) as a percentage of $[\text{La}^{3+}]$ in solution at time zero ($n = 3$). **A:** The plot for $\text{La}(\text{dpp})_3$, also showing the percentage of Hdpp measured by UV-Vis. **B:** The plot for $\text{K}_2[\text{La}(\text{XT})]$.

The reasons behind the observed phenomena are not immediately clear. As was highlighted in Chapter 1.2, the mechanism for binding of Ln^{3+} ions within the bone mineral matrix is complex and not fully understood, with a number of factors contributing to the kinetics including surface sorption, available surface area, and ion exchange rates. Furthermore, there are two unique Ca^{2+} environments within the HAP matrix that possess differing tendencies for exchange with La^{3+} , and

we hypothesize that this is at the root of the apparent redistribution of metal ions during the experiment. Add to the system two ligands which possess differing affinities for both the ion under investigation and the insoluble mineral, and the mechanism becomes more complicated still.

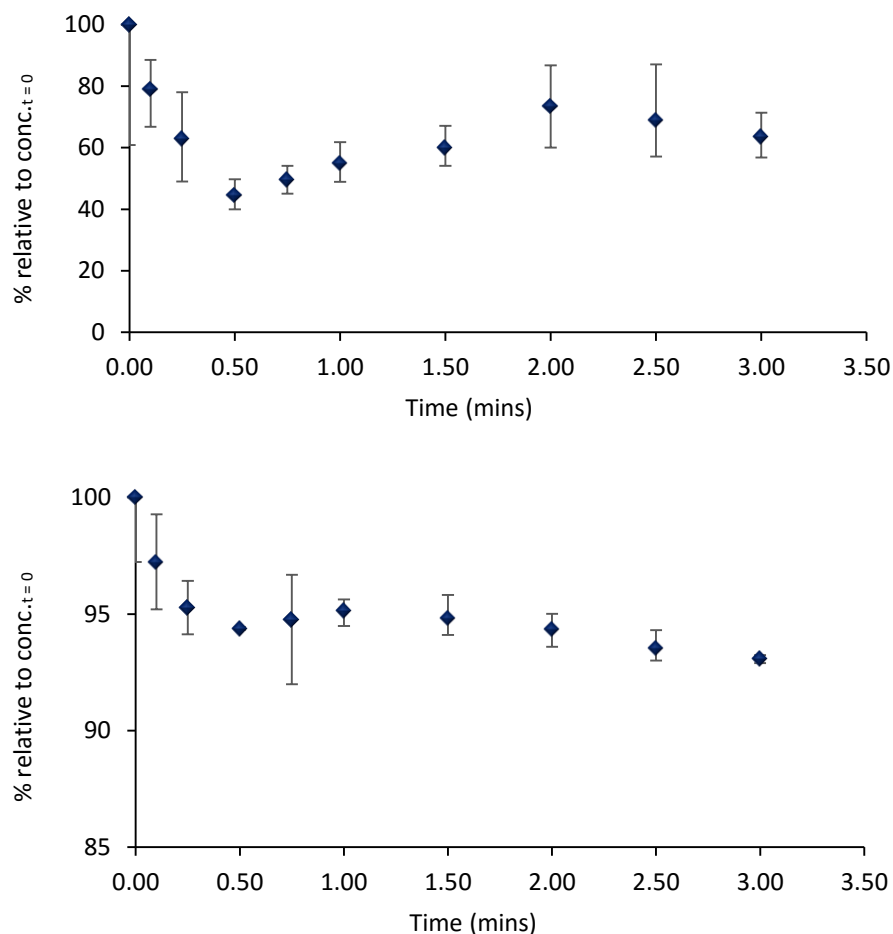


Figure 2.11 The depletion of La³⁺ over 3 minutes measured in solution by ICP-MS at 37 °C and pH 7.4 (100 mM HEPES buffer) as a percentage of [La³⁺] in solution at time zero ($n = 3$). **A:** La(dpp)₃. **B:** K₂[La(XT)].

In all of the solution depletion studies, a vast excess of HAP was used. The reason for this was two fold: first, to eliminate the kinetic dependence of the depletion plots on the mineral component; second, to try and imitate as much as possible a situation *in vivo*, in which bone tissue

will be in vast excess compared to a drug that is introduced. With that being said, it is important to recognize the clear discrepancies that exist between the experimental model and a living system, such as the differences in available binding surface area, chemical make-up, and morphology of true bone vs. HAP; the possible mechanisms of drug delivery; and the possibility for competing binding processes to occur *in vivo*. Overall, although HAP is considered a reasonable synthetic representation for bone mineral, it is unlikely that these results can be used to predict with great certainty the kinetic behaviour of either La(dpp)₃ or La(XT) in the context of real bone in a living system.

2.4 Conclusion of HAP binding studies

The results from ITC analysis and solution depletion studies show how two ligand systems – which are designed to improve the oral uptake of trivalent lanthanum and act as a potential treatment for resorption disorders – influence the binding of La³⁺ to an *in vitro* model for bone mineral (HAP). In the case of the bidentate 3-hydroxy-4-pyridinone Hdpp, the lack of any bone-directing functionality, as well as the thermodynamic instability of the desired 3:1 complex, meant that the ligand did not have a significant impact on the binding of La³⁺ to HAP. An optimistic interpretation of this could be that Hdpp does not hinder the natural strong tendency for La³⁺ to target bone *in vivo*; however, the speciation plots also suggest that the complex may not be stable enough to survive oral ingestion and have any subsequent impact on La³⁺ gastrointestinal uptake compared to a lanthanide salt (such as lanthanum carbonate).

For phosphinate-containing H₅XT – although binding clearly takes place – greater thermodynamic stability of the 1:1 metal complex as well as a HAP-binding moiety within the ligand itself contribute to a convoluted energetics profile between La³⁺ and bone mineral, making

it difficult to quantify this binding with only these results in hand. In this regard, it is quite challenging to assess the biological significance of these results, and so it will be left to *in vivo* studies (discussed in the next chapter) to truly determine the suitability of this system in the context of this project.

2.5 Experimental

2.5.1 Synthesis of La(dpp)₃ and La(XT)

The synthesis of hydrated *tris*-1,2-dimethyl-3-oxy-4-pyridinone lanthanum(III) (La(dpp)₃ • xH₂O) and bis-[[bis(carboxymethyl)amino]methyl]phosphinate lanthanum(III) dipotassium (K₂[La(XT)] • xH₂O) were adapted from previously reported procedures (References 67 and 68) and modified to generate gram scale quantities in single batches.

2.5.1.1 Materials and reagents for synthetic procedures

Water used in all synthetic procedures was deionized (15 MΩ-cm) and obtained from an Elga Purelab Option water purifier. Starting materials 1,2-dimethyl-3-hydroxy-4-pyridinone, iminodiacetic acid, hypophosphorous acid (50% w/w), and formaldehyde (37% w/w) were purchased from Sigma-Aldrich and used without further purification, as were solid potassium hydroxide and hydrochloric acid (37% solution). Lanthanum nitrate was purchased from Alfa Aesar as the hexahydrate.

2.5.1.2 Instruments

NMR spectroscopy was carried out at room temperature using a Bruker AV-300 spectrometer. ³¹P{¹H} NMR was referenced externally to H₃PO₄. Low resolution mass spectra were obtained

using an ESCI ion Waters ZQ spectrometer. High resolution mass spectra were carried out by Derek Smith or Marshall Lapawa (Analytical Services, Department of Chemistry, UBC) using a TOF Waters/Micromass LCT spectrometer. Elemental analysis (EA) was carried out by Derek Smith using a Carlo Erba Elemental Analyser 1108 machine. The X-ray crystal structure of $\text{La(dpp)}_3(\text{H}_2\text{O})_2 \cdot 11.75 \text{ H}_2\text{O}$ was solved by Dr. Brian Patrick (X-ray Crystallography, Department of Chemistry, UBC) using a Bruker X8 APEX CCD diffractometer and Bruker SAINT software.

2.5.1.3 Synthesis of La(dpp)_3

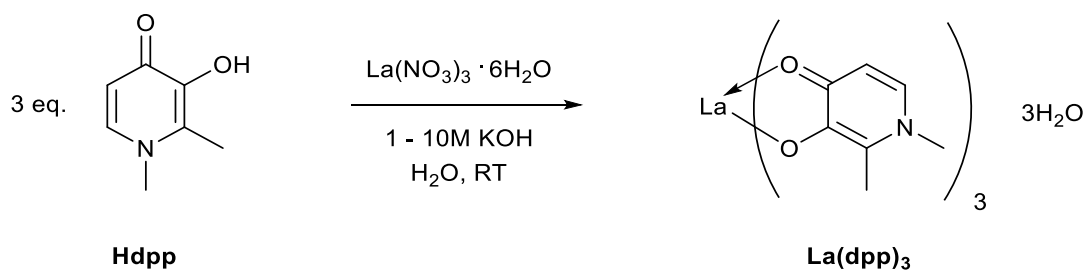


Figure 2.12 Synthesis of La(dpp)_3 from Hdpp and lanthanum nitrate hydrate and pH adjustment in aqueous conditions at room temperature.

Commercially available 1,2-dimethyl-3-hydroxy-4-pyridinone (Hdpp) (25.7 g, 184 mmol) was taken up in doubly distilled water (1 L) and stirred at room temperature until the ligand completely dissolved. Lanthanum nitrate hexahydrate (26.6 g, 61.4 mmol) was added and the pH adjusted, at first with 10 M KOH to approximately pH 6, then very gradually with 1 M KOH to pH 8.5. A white precipitate evolved overnight, which was collected by filtration on a medium frit, and washed several times with cold water followed by cold acetone. Freeze-drying overnight yielded the trihydrate complex of La(dpp)_3 as an off-white solid (22.8 g, 37.5 mmol, 61%). ESI-MS

positive ion mode (m/z): 576.1 $[M + Na]^+$, 554.1 $[M + H]^+$. 1H NMR (D_2O , 300 MHz, RT): δ 7.27 (br, 1H); 6.27 (br, 1H), 3.60 (br, 3H), 2.15 (br, 3H). Anal. Calc'd (found) for $La(dpp)_3 \cdot 3H_2O$ ($C_{21}H_{30}LaN_3O_9$): C, 41.53 (41.39); H, 4.98 (5.00); N, 6.65 (6.92).

2.5.1.4 Synthesis of La(XT)

$H_5XT \cdot HCl$

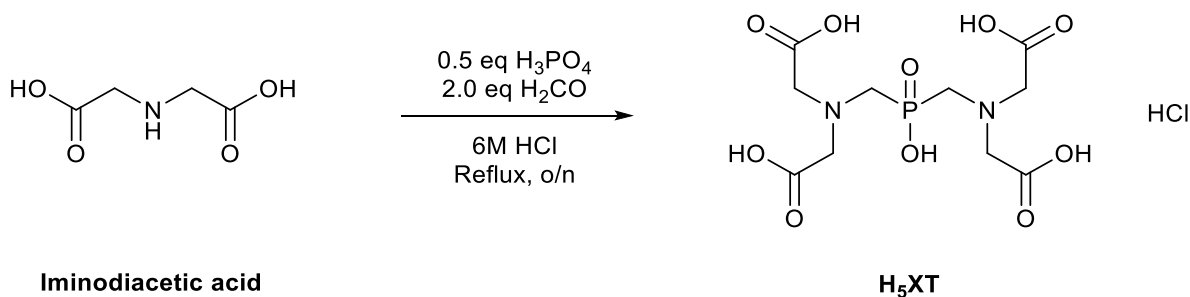


Figure 2.13 Synthesis of H_5XT as the HCl salt in a one-pot Mannich reaction from commercially available starting materials.

Iminodiacetic acid (27.0 g, 203 mmol), a commercially available off-white solid, was taken up in freshly prepared 6 M HCl (40 mL) with hypophosphorous acid (50 % w/w, 11.0 mL, 100 mmol) and heated to reflux, giving a light brown solution. Formaldehyde (37% w/w, 32.0 mL, 408 mmol) was added dropwise over the course of 2 hours, and the reaction mixture was stirred at reflux overnight. The product precipitated as a white solid which was collected on a fine frit, and washed several times with cold methanol followed by cold acetone. The filtrate was concentrated slightly to afford a second crop of precipitate which was washed in the same way and combined with the first crop. Freeze drying overnight gave the product as the HCl salt (21.4 g, 54.4 mmol, 54%). ESI-MS positive ion mode (m/z): 355.3 $[M - H]^-$. 1H NMR (D_2O , 300 MHz, RT): δ 4.10 (s, 8H), 3.52

(d, 4H, $^2J_{HP} = 12$ Hz). $^{31}\text{P}\{^1\text{H}\}$ NMR (D_2O , 121 MHz, RT): δ 17 (s). Anal. Calc'd (found) for $\text{H}_5\text{XT} \cdot \text{HCl}$ ($\text{C}_{10}\text{H}_{18}\text{ClN}_2\text{O}_{10}\text{P}$): C, 30.59 (30.95); H, 4.62 (4.58); N, 7.13 (6.97).

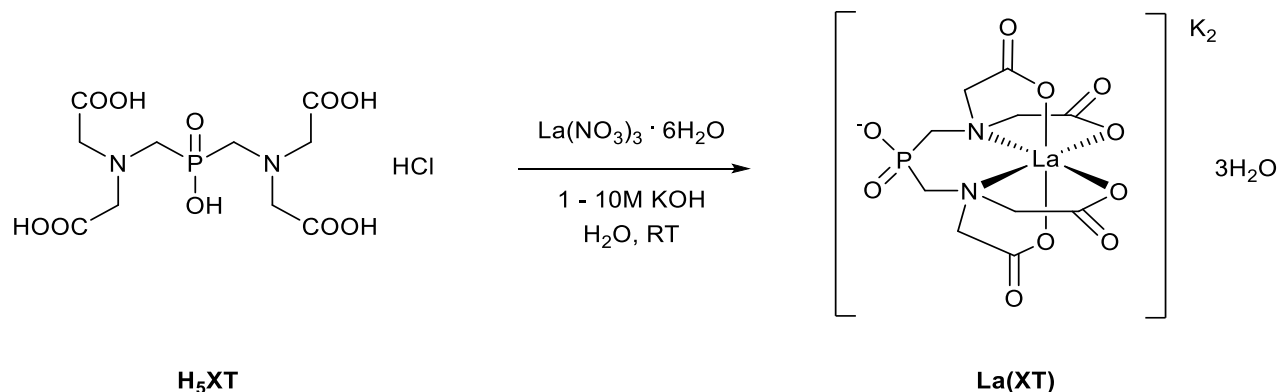
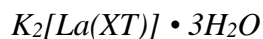


Figure 2.14 Synthesis of $\text{La}(\text{XT})$ from the HCl salt of H_5XT and lanthanum nitrate hexahydrate using pH adjustment under aqueous conditions at room temperature.

$\text{H}_5\text{XT} \cdot \text{HCl}$ (18.8 g, 48 mmol) and lanthanum nitrate hexahydrate (20.8 g, 48 mmol) were taken up in doubly distilled water (500 mL) and stirred at room temperature. Gradual increase of the pH with 10 M KOH initially caused the precipitation of a white solid (pH 1.5 to pH 2.5) which dissolved upon further addition of base (approx. pH 4.0). The pH was subsequently raised with 1 M KOH to pH 8, whereupon the solvent was carefully removed under vacuum. An off-white sticky solid remained which was taken up in the minimum volume of warm water (approx. 4 mL) and precipitated with an equal volume of methanol and excess acetone (approx. 30 mL). The product was collected on a fine frit, and freeze dried overnight to give the trihydrate complex of $\text{K}_2[\text{La}(\text{XT})]$ (23.7 g, 38 mmol, 79%). ESI-MS negative ion mode (m/z): 529.0 $[\text{M} - \text{K}]^-$, 245.2 $[\text{M} - 2\text{K}]^{2-}$. HR-ESI-MS Calc'd (found) for $\text{C}_{10}\text{H}_{12}\text{K}^{139}\text{LaN}_2\text{O}_{10}\text{P}$: $m/z = 528.8936$ (528.8930). ^1H

NMR (D₂O, 300 MHz, RT): δ 3.8-2.8 (m). ³¹P{¹H} NMR (D₂O, 121 MHz, RT): δ 11. Anal. Calc'd (found) for K₂[La(XT)]·3H₂O (C₁₀H₁₈K₂LaN₂O₁₃P): C, 19.30 (19.31); H, 2.92 (2.87); N, 4.50 (4.45).

2.5.2 General experimental for HAP studies

High purity water (MQ, 18.2 M Ω -cm) was obtained from an Elga Purelab Ultra water purifier and used in all experiments. Compounds were either purchased (Hdpp, Sigma-Aldrich) or prepared according to the procedures described in Section 2.4.1. All glassware, vials, Eppendorf tubes, pipette tips etc. were prewashed by soaking overnight in HNO₃ (5%) and thoroughly rinsed with MQ water. HEPES buffer, piperazine buffer, and sodium chloride were obtained from Fisher Scientific. Synthetic hydroxyapatite was purchased from Sigma-Aldrich, and was analyzed for Ca/P molar ratio (1.65) by ICP-OES, and further characterized using TGA, BET analysis and powder-XRD in accordance with previous studies.^{11,69} ITC experiments were performed on a Microcal MSC-ITC by Dr. Louise Creagh (Michael Smith Laboratories, UBC), and all ligand and metal/ligand solutions were prepared on the day of the experiment. Nitric acid Optima and high purity hydrogen peroxide for digestion of ICP-MS samples were purchased from Fisher Scientific. Lanthanum and rhodium standards (1000 μ g/mL in 2% HCl) for standard curve calibration in ICP-MS were purchased from High Purity Standards. ICP-MS was run using an Agilent 7700x quadrupole machine equipped with an auto-sampler under the direction of Dr. Vivian Lai and Dr. Marghaleray Amini (PCIGR, Earth and Ocean Sciences, UBC).

2.5.2.1 Experimental for ITC

ITC experiments in the presence of either ligand (Hdpp or H₅XT) or La³⁺/ligand were carried out at either pH 5.0 (100 mM piperazine) or pH 7.4 (100 mM HEPES). Titrations were performed by injecting consecutive 10 μ L aliquots of ligand (2.5-80 mM) or metal/ligand (1:4 for Hdpp or 8:9 for H₅XT, 2.5-80 mM with respect to the metal ion) solution into the ITC cell (volume = 1.4 mL) containing a hydroxyapatite suspension (0.1-1.5 mM). HAP suspensions were prepared by sonicating the appropriate amount in pre-buffered solution for 5 minutes. The ITC cell was stirred continuously during the titration. Control experiments were carried out by measuring the heats of dilution given off by titrating solutions of either ligand or metal/ligand solution into buffer containing no HAP. Each experiment was performed in triplicate (at least). The error associated with diffusion from the syringe during baseline equilibration prior to the first injection was only 5 μ L, and the associated small heat change was not included in the data analysis.

2.5.2.2 Experimental for solution depletion studies

All time points were collected in triplicate. Samples containing 10 mg of HAP were initially incubated and agitated (37 °C, 220 rpm) with 0.9 mL HEPES buffer (100 mM, pH 7.4 at 37 °C) in 1.5 mL Eppendorf tubes for 24 hours. Stock solutions of either La(dpp)₃ or K₂[La(XT)] (1.0 mM) were prepared in buffer solution from the premade 1:3 or 1:1 complexes respectively. At the outset of the experiment, 100 μ L of either solution was added to a HAP suspension and incubated and agitated for a set period of time. When the end point for that experiment was reached, the supernatant was carefully removed by syringe, taking care not to disturb the residual HAP pellet, and filtered through a 22 μ m frit. An accurately weighed aliquot of this solution (approximately 100 mg) was prepared for ICP-MS by acid digestion (HNO₃ followed by H₂O₂) and evaporation

and analyzed for lanthanum content (see Appendix for ICP-MS calibration). Samples for $\text{La}(\text{dpp})_3$ experiments were also analysed by UV-Vis spectroscopy to determine Hdpp concentrations. Zero time points were simulated by preparing samples containing no HAP. Background La^{3+} levels were corrected for against samples containing no lanthanum complex.

Chapter 3: *In vivo* biodistribution of La(dpp)₃ and La(XT)

3.1 Introduction

In pharmaceutical chemistry, the premise behind almost all testing procedures is to provide the best possible impression of how a drug will behave when it is introduced into a human subject. Thus far, with our two lead compounds La(dpp)₃ and La(XT), we have engaged in rigorous experimentation to demonstrate cytotoxicity on a relevant cell line;^{67,69} permeability towards a GI tract-like cell membrane;^{67,69} and the energetics of the interaction between either of the metal complexes and the intended target organ (Chapter 2). The design of these experiments was such that the results can, to a certain extent, be extrapolated to provide predictions of physiological behaviour; however, such is the myriad of molecular complexity present within living systems – as well as continuously fluctuating physical conditions – that *in vivo* studies are critical to evaluating the viability of either of the two drug candidates.

This chapter describes the first studies performed in small animal models (healthy adult Sprague-Dawley (SD) rats) of lanthanum complexes with specifically designed chelating ligands envisioned for use in the treatment of resorption disorders. Three preliminary studies are presented, which are intended to assess our ability to detect La³⁺ in certain tissues (including bone), and to elucidate the systems' effectiveness in directing the metal towards bone. First is time-dependent plasma clearance and soft-tissue distribution from a single intravenous (IV) dose of La(dpp)₃; second is an acute (5 days) multiple IV dose experiment to show differences in bone and tissue distribution between the two complexes; and finally is a short-term (4 week) multiple oral (and parallel-run IV) dose experiment demonstrating oral uptake and biodistribution. In the final set of experiments, solubility issues with La(dpp)₃ were also addressed by testing two different formulations of the metal complex.

Dose levels are reported as mass of compound *per* mass of the animal *per* unit time (i.e. $\text{mg kg}^{-1} \text{ day}^{-1}$). It is worth noting that, although the compounds differ significantly in their chemical structures, the trihydrate complexes of either system have roughly the same percentage lanthanum content ($\text{La} = 22.9\%$ for $\text{La}(\text{dpp})_3 \cdot 3\text{H}_2\text{O}$ and 22.3% for $\text{K}_2[\text{La}(\text{XT})] \cdot 3\text{H}_2\text{O}$). Thus, equal doses of either complex can be administered and compared directly.

In all cases, results from the experiments are presented as lanthanum concentrations in either soft tissues, bone, or plasma ($\text{ppb} = \text{ng g}^{-1}$ or ng mL^{-1}) as measured by ICP-MS, an extremely sensitive yet incredibly versatile tool for establishing precise levels of single elements in a vast range of background media. The technique is especially useful for lanthanum, which has a single dominant isotope (^{139}La , $>99.9\%$ abundance)⁸² and rarely suffers from any interference from oxide, hydroxide, or chloride artefacts (which can coincide with a desired mass signal and suppress sensitivity).⁸³ Biological matrix effects – which can suppress overall sensitivity – are minimized by referencing all samples to an internal standard (^{103}Rh , 100% abundance).⁸² As a result, and with the use of carefully made calibration standards, detection limits on the order of parts per trillion can be achieved (see Appendix).

3.2 Results and discussion

3.2.1 Plasma clearance and soft-tissue distribution from single IV dose

Figure 3.1 shows a plot of $[\text{La}^{3+}]$ in plasma *versus* time from SD rats ($n = 6$) administered a single IV dose (1 mg kg^{-1}) of $\text{La}(\text{dpp})_3$. The associated non-compartmental pharmacokinetic parameters are given in Table 3.1, and the soft-tissue distribution by ICP-MS 5 days post-injection is shown in Figure 3.2.

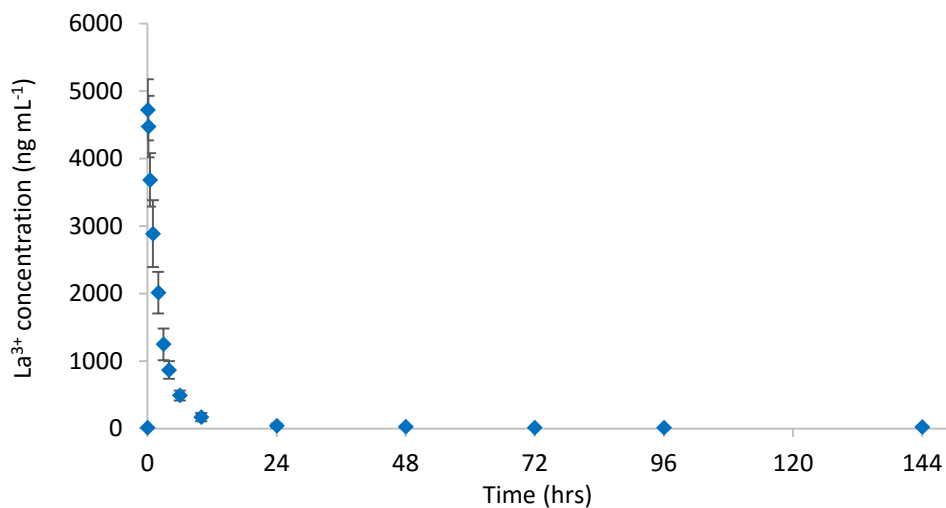


Figure 3.1 Plasma lanthanum concentration time (h) profile following single IV dose (1 mg kg⁻¹) of La(dpp)₃ in SD rats (*n* = 6).

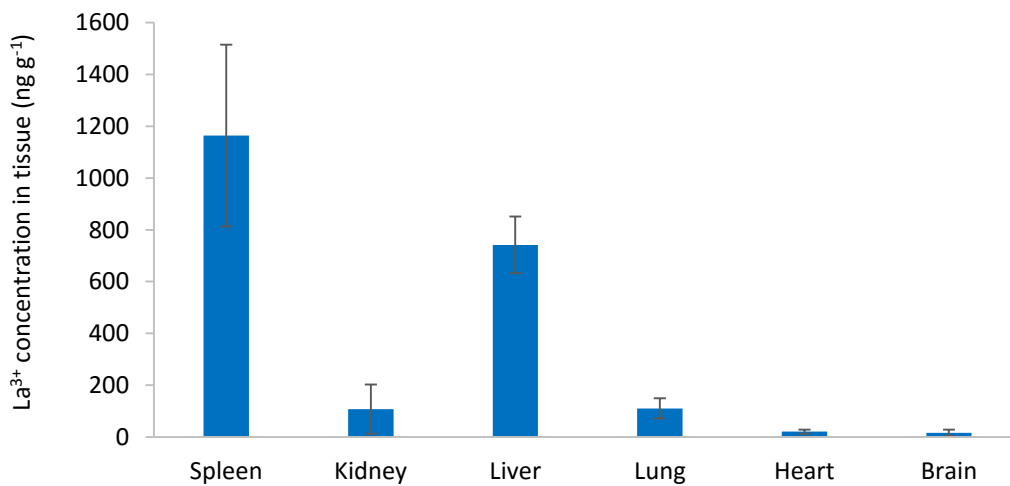


Figure 3.2 Soft-tissue distribution of La³⁺ after 5 days following single IV dose (1 mg kg⁻¹) of La(dpp)₃ (*n* = 6; mean ± std. dev.).

Table 3.1 Pharmacokinetic parameters derived from non-compartmental analysis ($n = 6$; mean \pm std. dev.) of the data presented in Figure 3.1 using Phoenix software (Ver. 1.3).

Parameter	Unit	Mean	Std. dev.
K_{el}	h^{-1}	0.20	0.04
$T_{1/2}$	h	3.61	0.85
C_0	$ng\ mL^{-1}$	4973.09	556.75
$AUC_{0-\infty}$	$h\ ng\ mL^{-1}$	13155.37	1812.52
Cl	$mL\ h^{-1}\ kg^{-1}$	77.24	10.73
$AUMC_{0-\infty}$	$h^2\ ng\ mL^{-1}$	45778.12	12609.75
MRT	h	3.46	0.69
V_{ss}	$mL\ kg^{-1}$	265.41	51.33

When administered as the $La(dpp)_3$ complex, plasma levels of lanthanum show a peak (C_0) of $4973 \pm 557\ ng\ mL^{-1}$ which rapidly decreased to approximately 10% of C_0 within 6 hours, and back to pre-dose concentrations ($<15\ ng\ mL^{-1}$ background levels) within 24 hours. The clearance rate (Cl) of La^{3+} from plasma was $77\ mL\ h^{-1}\ kg^{-1}$ and the steady state volume of distribution (V_{ss}) was $265\ mL\ kg^{-1}$. Lanthanum from $La(dpp)_3$ was not detected in the plasma beyond 10 h, showing a mean residence time (MRT) of less than 4 hours. These data are in keeping with previous studies which examined the clearance of $LaCl_3$ after a single IV dose by non-compartmental analysis,⁸⁴ and show that Hdpp does not interfere with initial clearance of the metal ion from blood.

Although plasma levels of lanthanum above pre-dose concentrations were not detected after 24 h (Figure 3.1), La^{3+} was still detected in soft tissues after the final sampling point at 144 h (Figure 3.2). Heart ($20 \pm 7\ ng\ g^{-1}$) and brain ($15 \pm 12\ ng\ g^{-1}$) lanthanum levels were found to be negligible, exemplifying low residual circulation time and no tendency for penetrating the blood brain barrier; however, it is worth noting the high concentration for the spleen ($1164 \pm 350\ ng\ g^{-1}$) and liver ($741 \pm 109\ ng\ g^{-1}$). This is consistent with previous findings which indicate that the liver

is the main organ for the excretion of lanthanum, and that full elimination can take up to 14 days.^{84,85} This fact also calls into question the legitimacy of a non-compartmental model for the pharmacokinetic analysis since the metal ion is still detected so long after the single injection – which could suggest redistribution back into the blood after initial tissue binding – and it may be prudent to apply a more complex compartmental model in future pharmacokinetic studies.

3.2.2 Biodistribution from multiple IV doses

Tissue distribution of lanthanum in organs and bone in SD rats ($n = 6$) following the administration of five consecutive daily IV doses of either La(dpp)₃ or La(XT) (1 mg kg⁻¹) are shown in Figure 3.3. The first point to note is that the organ distribution of La³⁺ is very similar for both compounds. The highest concentration of La³⁺ was found in the liver (13611 ± 1687 ng g⁻¹ for La(dpp)₃, 16983 ± 1160 ng g⁻¹ for La(XT)) and spleen (7817 ± 3211 ng g⁻¹ for La(dpp)₃, 3854 ± 827 ng g⁻¹ for La(XT)), analogous to the results found for the single IV dose in the previous experiment. Again, the lowest accumulation was in the heart (635 ± 178 ng g⁻¹ for La(dpp)₃, 768 ± 115 ng g⁻¹ for La(XT)) and the brain (101 ± 60 ng g⁻¹ for La(dpp)₃, 112 ± 84 ng g⁻¹ for La(XT)).

Plasma samples were also collected just prior to animal sacrifice immediately after the final injection and were found to contain similar levels of La³⁺ (5517 ± 1188 ng mL⁻¹ for La(dpp)₃, 5999 ± 302 ng mL⁻¹ for La(XT)), but it is worth noting that La(dpp)₃ has a considerably larger inter-animal variability than does La(XT). A possible cause of this may lie with the differences in thermodynamic stability due to denticity, as was outlined in Chapter 2.

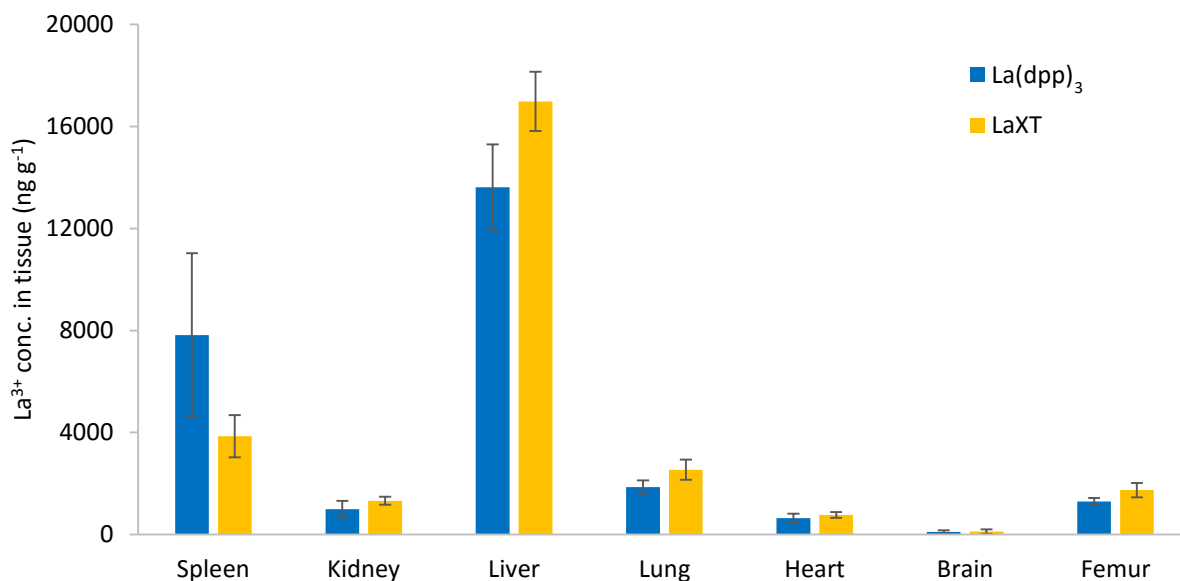


Figure 3.3 Biodistribution of La^{3+} from the complexes $\text{La}(\text{dpp})_3$ and $\text{La}(\text{XT})$ following multiple IV dose administrations at $1 \text{ mg kg}^{-1} \text{ day}^{-1}$ for 5 days in SD rats ($n = 6$; mean \pm std. dev.).

Figure 3.3 also shows La^{3+} distribution in the femurs collected from the experiment ($1294 \pm 134 \text{ ng g}^{-1}$ for $\text{La}(\text{dpp})_3$, $1742 \pm 282 \text{ ng g}^{-1}$ for $\text{La}(\text{XT})$). These bones were sectioned into hip, mid, and knee sections and separately analyzed for lanthanum content, and the results are presented in Figure 3.4. The bone distribution of lanthanum appears slightly greater in animals treated with $\text{La}(\text{XT})$ ($1267 \pm 195 \text{ ng g}^{-1}$, $1200 \pm 131 \text{ ng g}^{-1}$, and $2757 \pm 444 \text{ ng g}^{-1}$ in the hip, mid, and knee sections, respectively) compared to $\text{La}(\text{dpp})_3$ ($904 \pm 130 \text{ ng g}^{-1}$, $995 \pm 92 \text{ ng g}^{-1}$, and 1982 ng g^{-1} in the hip, mid, and knee sections, respectively). We hypothesize that this difference in La uptake is due to the greater thermodynamic stability of the $\text{La}(\text{XT})$ complex, as well as the presence of the phosphinate group in H_5XT which improves bone targeting.

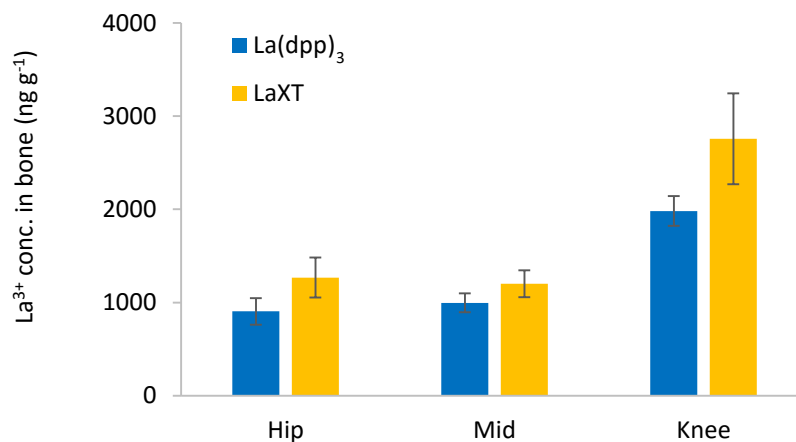


Figure 3.4 Distribution of lanthanum within the femur from the complexes La(dpp)₃ and La(XT) after multiple doses of 1 mg kg⁻¹ day⁻¹ for 5 days in SD rats ($n = 6$; mean \pm std. dev.).

It is also worth noting that consistently greater levels of La³⁺ were detected in the knee section of the femur *versus* the hip and middle sections, suggesting regions of higher bone turnover actively incorporate La³⁺ ions into the bone structure more rapidly. This phenomenon is emphasized in the final set of experiments presented in the next section. Overall, lanthanum is rapidly cleared from the blood after single or multiple intravenous dose administration, with redistribution to the bone as well as certain soft tissues and organs (predominantly the liver and spleen).

3.2.3 Biodistribution from short-term oral and IV doses

Figure 3.5 and 3.6 show the La³⁺ tissue distribution in SD rats ($n = 4$) from IV (1 mg kg⁻¹ week⁻¹) and oral (50 mg kg⁻¹ day⁻¹) dosing, respectively, for 4 weeks with either La(dpp)₃ or La(XT). The IV and oral experiments were conducted in parallel, but due to a high variation in values are shown on different plots. Two formulations of La(dpp)₃ were also tested: carboxymethyl cellulose (CMC)

and Gelucire 44/14 with Peceol (herein referred to as Gelucire). CMC is a carboxymethyl-functionalized cellulose derivative commonly used in food as a viscosity modifier, and it was used here in conjunction with the non-ionic surfactant Tween-80 as a stabilizer. Gelucire 44/14 is a non-ionic water dispersible surfactant composed of PEG-esters, glyceride, and free PEG, used in conjunction with Peceol – an oily vehicle used in lipid formulations, and a known bioavailability enhancer. Both CMC and Gelucire were selected as simple, self-emulsifying formulations aimed at improving solubility and enhancing absorption of La(dpp)₃.

The results from the 4-week IV experiments (Figure 3.5) show a similar – but more pronounced – soft tissue distribution bias to the single dose (Figure 3.2) and 5-day (Figure 3.3) IV experiments. The spleen and the liver again show the highest values, but with La³⁺ levels in spleen for La(dpp)₃ (13608 ± 4607 ng g⁻¹) significantly greater than for La(XT) (710 ± 79 ng g⁻¹). An explanation for this could lie in the lack of thermodynamic stability of the La(dpp)₃ complex, the decomposition of which leads to free 3+ ions in solution, potentially producing a high number of damaged red blood cells which collect in the spleen. This hypothesis should be tested in future studies by collecting and analyzing whole blood as opposed to plasma, as well as a thorough toxicological investigation. Greater uptake in the spleen is not observed with La(XT), nor is it observed for either compound in the liver, for which La³⁺ levels are lower in the 4-week IV study (5882 ± 1748 ng g⁻¹ for La(dpp)₃, 3237 ± 253 ng g⁻¹ for La(XT)) implying active liver clearance. Lanthanum levels detected in all other soft tissues (kidney, lung, heart, brain, stomach, small intestine) after IV dosing were comparatively low (<350 ng g⁻¹) for both La(dpp)₃ and La(XT).

In the femurs, significant lanthanum levels were detected after 4-weeks IV dosing (Figure 3.5) for both compounds (1645 ± 260 ng g⁻¹ for La(dpp)₃, 1478 ± 258 ng g⁻¹ for La(XT)). It is interesting to note that these levels are of a similar magnitude to La³⁺ concentrations detected in

the femurs after the 5-day trial (Figure 3.3), in which the animals were dosed with a comparable quantity of drug over a much shorter period of time. This implies that the metal ion is *retained* in bone, and that the skeleton is a sink for La^{3+} that enables gradual accumulation of the metal ion over time. Knowing this fact will allow for lower dosing over longer time periods in future studies.

Figure 3.6 shows the lanthanum tissue distribution after 4-weeks oral dosing ($50 \text{ mg kg}^{-1} \text{ day}^{-1}$) with either one of the two formulations of $\text{La}(\text{dpp})_3$ (CMC or Gelucire), or $\text{La}(\text{XT})$. In these experiments, lanthanum concentrations in the lung and stomach showed greater-than-expected values and large variation between animals. This is due to gavage-related reflux and is to be expected, and consequently these data points were omitted from the biodistribution plots. Lanthanum levels in all tissues after oral administration of either compound were significantly lower than after IV dosing. For $\text{La}(\text{dpp})_3$, La^{3+} levels detected in all tissues were almost negligible, with no organ measuring more than 50 ng g^{-1} for either formulation; however, it is interesting to note that some of the highest detected levels of La were in the target tissue (femur, $36 \pm 4 \text{ ng g}^{-1}$ for CMC, $46 \pm 10 \text{ ng g}^{-1}$ for Gelucire). This is particularly noteworthy in light of the fact that once lanthanum reaches bone, it will be retained within the tissue.

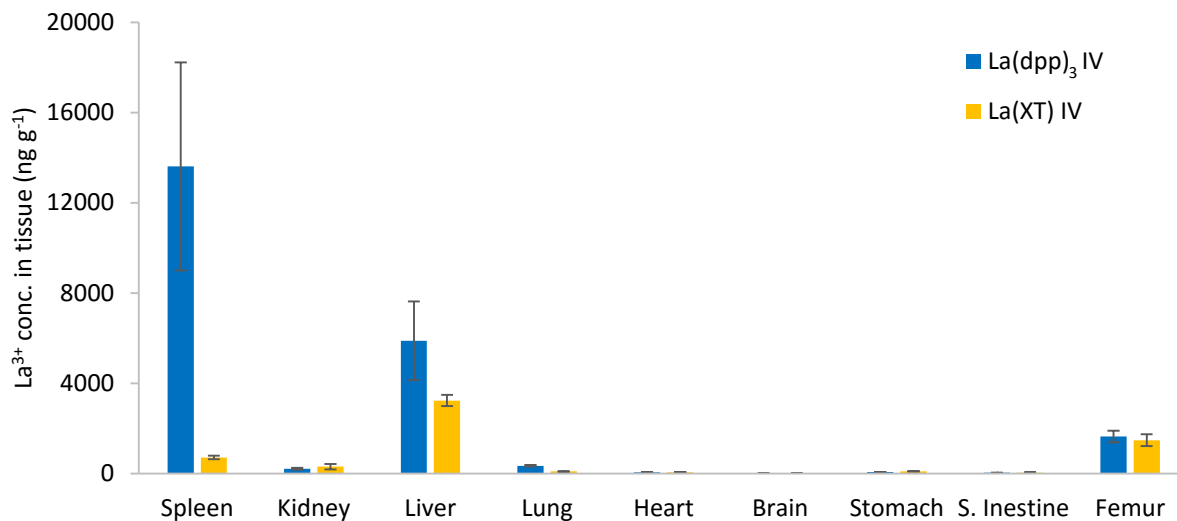


Figure 3.5 Biodistribution of La^{3+} from the complexes $\text{La}(\text{dpp})_3$ and $\text{La}(\text{XT})$ following multiple IV dose administrations at $1 \text{ mg kg}^{-1} \text{ week}^{-1}$ for 4 weeks in SD rats ($n = 4$; mean \pm std. dev.).

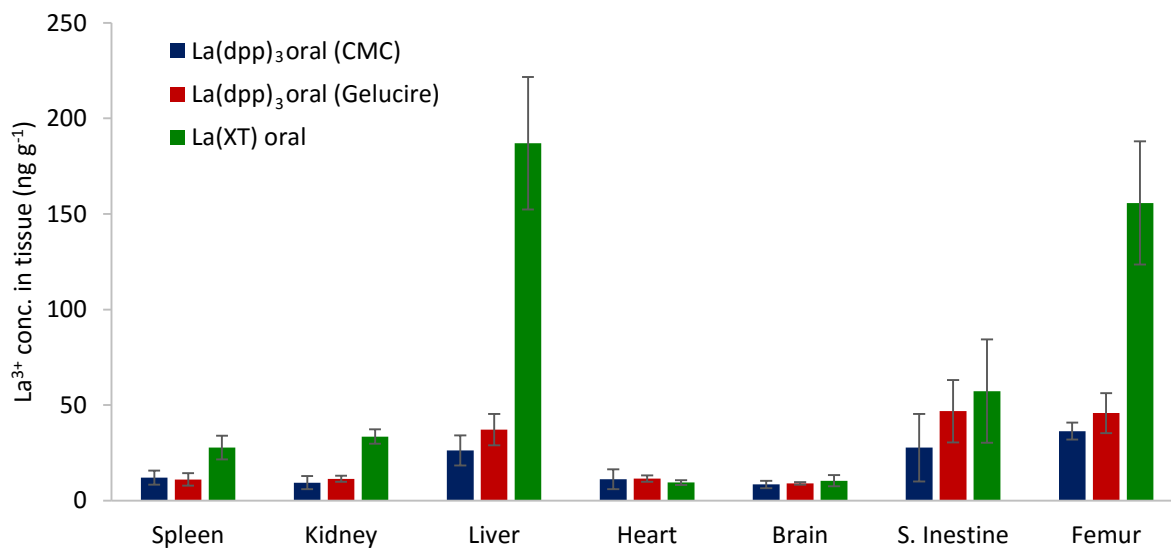


Figure 3.6 Biodistribution of La^{3+} from the complexes $\text{La}(\text{dpp})_3$ (two formulations) and $\text{La}(\text{XT})$ following multiple oral dose administrations at $50 \text{ mg kg}^{-1} \text{ day}^{-1}$ for 4 weeks in SD rats ($n = 4$; mean \pm std. dev.).

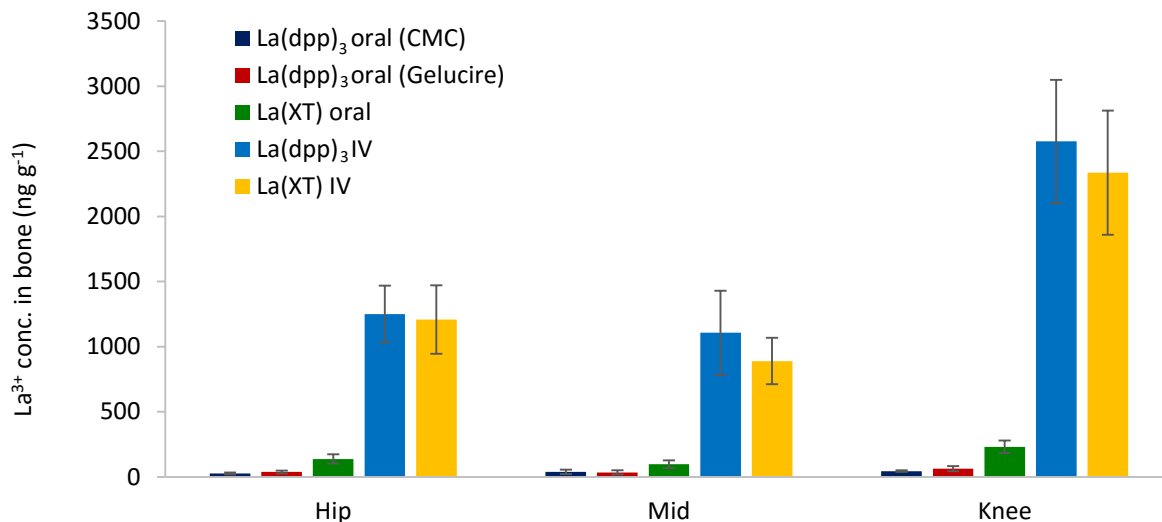


Figure 3.7 Distribution of lanthanum within the femurs of SD rats from oral administration with either La(dpp)₃ (CMC or Gelucire formulation), or La(XT) after dosing at 50 mg kg⁻¹ day⁻¹ for 4 weeks; and IV administration with either La(dpp)₃ or La(XT) after multiple doses of 1 mg kg⁻¹ week⁻¹ for 4 weeks (*n* = 4; mean ± std. dev.).

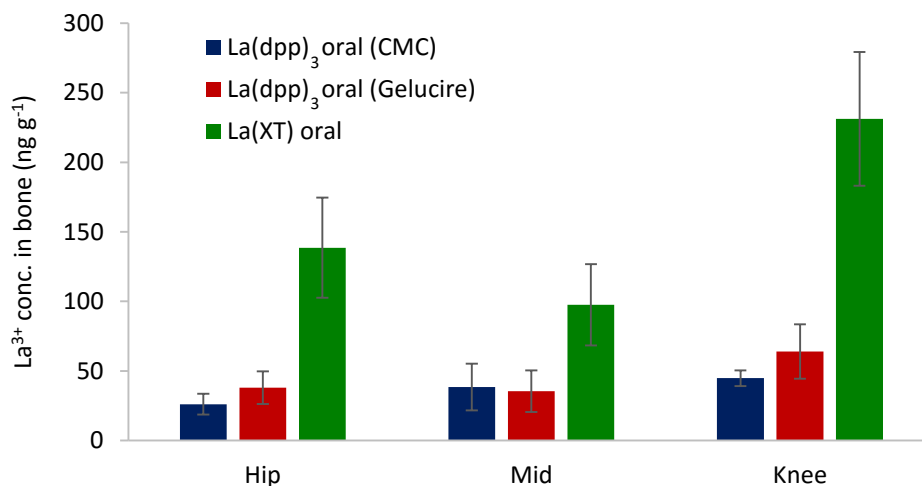


Figure 3.8 Expansion of the distribution of lanthanum within the femurs of SD rats showing only the results from oral administration (50 mg kg⁻¹ day⁻¹) for 4 weeks with either La(dpp)₃ (two formulations) or La(XT) (*n* = 4; mean ± std. dev.).

Lanthanum levels after oral administration with La(XT) (although still substantially lower than for IV dosing) show a distinct improvement in overall uptake compared to La(dpp)₃ (while exhibiting equally negligible La levels in non-target organs, i.e. heart and brain). In particular, La³⁺ levels from La(XT) oral dosing in the spleen ($28 \pm 6 \text{ ng g}^{-1}$), kidney ($34 \pm 4 \text{ ng g}^{-1}$), and liver ($187 \pm 35 \text{ ng g}^{-1}$), which are between 3 to 5 times greater than for either formulation of La(dpp)₃, are indicative of enhanced absorption from the GI tract into the blood stream. Furthermore, absorption is followed by redistribution to bone tissue, with femur lanthanum levels ($156 \pm 32 \text{ ng g}^{-1}$) amongst the highest measured for La(XT) in the oral studies.

Figure 3.7 and shows the La³⁺ distribution after the 4 week trials within femurs partitioned into hip, mid, and knee sections (IV and oral dosing). Analogous to the 5-day IV study (Figure 3.4), lanthanum preferentially accumulates in the knee section after 4-weeks IV dosing with either compound ($2577 \pm 473 \text{ ng g}^{-1}$ for La(dpp)₃, $2336 \pm 476 \text{ ng g}^{-1}$ for La(XT)) rather than the hip or mid sections, highlighting the propensity for lanthanum to be incorporated into regions of bone with higher turnover. With these results, femur uptake is comparable (within error) regardless of which drug is administered.

Figure 3.8 shows the femur distribution data from the 4-week oral dosing experiments only, and emphasises the preferential uptake of lanthanum administered orally as the XT complex rather than the dpp complex (irrespective of which formulation is used). In each of the femur sections, La³⁺ levels from La(XT) dosing are approximately 3 to 4 times greater than for La(dpp)₃ dosing, with the knee again exhibiting the greatest La³⁺ uptake ($44 \pm 6 \text{ ng g}^{-1}$ for La(dpp)₃ (CMC); $64 \pm 20 \text{ ng g}^{-1}$ for La(dpp)₃ (Gelucire); $231 \pm 48 \text{ ng g}^{-1}$ for La(XT)).

3.3 Elemental mapping of La³⁺ in bone using K-edge subtraction imaging

The sectioning of femur bones from SD rats treated with either La(dpp)₃ or La(XT) into hip, mid, and knee sections for solution ICP-MS gives a rudimentary indication of how lanthanum is distributed within hard tissues following drug administration. From the results presented, one can conclude that the knee section – where bone tissue is remodelled more rapidly – shows a greater propensity for La uptake than either the hip or mid sections. This is in keeping with other metal ions which target bone tissue, is somewhat intuitive, and does not shed light on any mechanistic intricacies – or subsequent physiological impact – of metal-ion inclusion into mineralized bone. Of significantly greater value would be the ability to accurately resolve the spatial distribution of lanthanum in bone, without the need to destroy the tissue (as is the case for solution ICP-MS).

X-ray absorption spectroscopy (XAS) is an extremely powerful tool for providing 3D images of biological structures which are compelling, informative, and can be used to map specific elements of interest.⁸⁵ Elemental mapping of lanthanum in bone using a synchrotron X-ray source has been performed previously on fossilized bone.⁸⁶ Furthermore, such is the resolution of XAS analysis that bone can be examined on a micro-architectural level, giving insight into the effects of lanthanum on bone mineral composition, density, and lattice structure.^{87,88} In a preliminary proof-of-concept analysis, the lower lumbar vertebrae from one of the experiments detailed in Section 3.2.3 (4 weeks IV dosing at 1 mg kg⁻¹ week⁻¹ with La(XT)) was evaluated by K-edge subtraction (KES) imaging method from a monochromatic tunable X-ray beam at the Canadian Light Source (CLS, Saskatoon, SK, Canada) under the direction of Dr. Arash Panahifar and Dr. Jacqueline Cawthray (College of Pharmacy and Nutrition, University of Saskatchewan). The image (Figure 3.9) was obtained at a resolution of 13 μm, and shows a representative 2D cross-section of bone with lanthanum mapped in red.

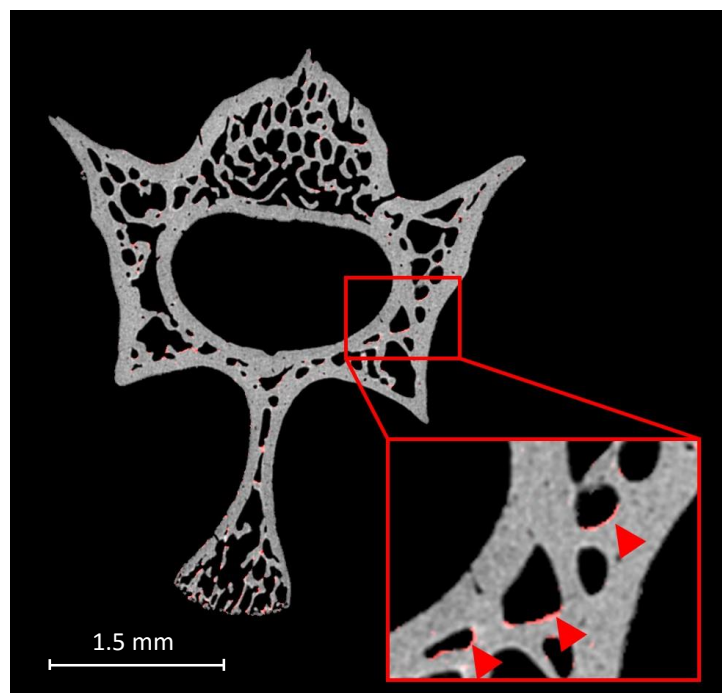


Figure 3.9 Elemental mapping of lanthanum (red) in a cross-section of lower lumbar spine from a SD rat treated with La(XT) by IV administration ($1 \text{ mg kg}^{-1} \text{ week}^{-1}$) for 4 weeks. The image was obtained by KES method at the CLS at a resolution of $13 \text{ }\mu\text{m}$ from a tunable monochromatic X-ray source, which can be adjusted to the K-edge of lanthanum (39 keV).

The image shows extremely sparse distribution of lanthanum around the surface edges of the lumbar vertebra. There is very little penetration into the mineral matrix by the metal ion, which is to be expected for such a short time period of drug administration (1 month). It is worth noting that this instance represents the lower limit of detection for spectral KES analysis, but solution ICP-MS results from this treatment group showed some of the highest lanthanum uptake in bone in that particular set of experiments (4-week IV administration of La(XT) at $1 \text{ mg kg}^{-1} \text{ week}^{-1}$ mean La^{3+} in femur = 1478 ng g^{-1}). With this in mind this particular technique is best reserved for future

experiments in which La drugs are administered chronically (several months), and where the metal ion is expected to have an impact on the physiological and mechanical properties of bone.

3.4 Conclusions

Two systems, La(dpp)₃ and La(XT) – which emerged as lead compounds for this project through thorough systematic physical and *in vitro* investigations – were tested for the first time in animal models to determine the influence of a specifically-designed chelating ligand on the plasma clearance and tissue distribution of trivalent lanthanum in healthy SD rats. Non-compartmental pharmacokinetic data for La(dpp)₃ show rapid and quantitative initial clearance from the blood after a single IV injection; however, due to detectable La³⁺ concentrations across soft-tissue organs 5-days post-injection (Section 3.2.1), a more thorough pharmacokinetic study is required to determine the validity of the non-compartmental model.

Acute (5-day) IV studies with both complexes show similar organ distribution for La(dpp)₃ and La(XT), with the liver and spleen being main sites of La accumulation (Section 3.2.2). These results also show comparable levels of lanthanum in bone tissue (femurs) between the two drug candidates, suggesting that the ligand system does not have a significant influence on IV biodistribution. This is emphasised in the 4-week IV study, (Section 3.2.3, Figure 3.5 and Figure 3.7), which – with the exception of the spleen – show a similar La³⁺ organ and bone distribution for La(dpp)₃ and La(XT). High spleen levels for former are hypothesized to be due to a lack of *in vivo* stability of the *tris* complex, and implore a more thorough toxicological evaluation in future experiments. Comparable femur levels of lanthanum from the two IV dosing regimes (5-days and 4-weeks) imply accumulation and retention of lanthanum in bone. Furthermore, greater uptake in

the knee sections (*versus* hip or mid) in the femurs of all experiments (Figures 3.4, 3.7, and 3.8) suggest that La^{3+} is actively incorporated into regions of higher bone turnover.

The 4-week oral study with the two compounds (Figure 3.6 and Figure 3.8) show that absorption is followed by lanthanum redistribution to the bone. La(XT) exhibits greater overall absorption, irrespective of applying two different formulations to $\text{La}(\text{dpp})_3$ (CMC or Gelucire) in an effort to improve GI uptake and solubility. An explanation for this is the greater thermodynamic stability exhibited by the 1:1 complex compared to the 3:1 complex (emphasised in Chapter 2), which suggests that $\text{La}(\text{dpp})_3$ does not remain stable *in vivo* long enough for the pyridinone ligand system to significantly influence lanthanum absorption. This, along with ongoing solubility issues, hinder the continued use of $\text{La}(\text{dpp})_3$, and as the data obtained do not suggest any benefit of the bidentate ligand over XT (in terms of bone uptake or organ distribution), it will not be used in future *in vivo* studies (see Section 5.2.3). On the other hand, oral dosing with La(XT) leads to partial GI absorption without the need for formulation, with preferential redistribution to the bone, thereby fitting the profile of an ideal lead candidate.

As has been alluded to in this chapter, there are a number of major considerations for future *in vivo* experiments yet to be investigated which are vital to assessing the validity of these potential treatments. First and foremost is toxicity, both in terms of behavioural observations of the treated animals, and a full post-experimental analysis of the non-target organs which show a propensity to accumulate La^{3+} (liver and spleen); second is lanthanum recovery *via* examining excreted materials from treated animals, which is essential to determining the exact route of elimination as well as absolute quantification of the metal ion concentration in tissues; finally, some consideration must be given to the ligands themselves, which both have the propensity to invoke their own biological responses depending on their distribution, toxicity, and pharmacokinetics.

3.5 Experimental

3.5.1 General experimental for *in vivo* studies

All animal studies were carried out at the University of British Columbia or the University of Saskatchewan (Wasan Research Group, College of Pharmacy and Nutrition) and were approved by the respective institutions' University Animal Care Committees (UACC) and performed in accordance with the guidelines outlined by the Canadian Council on Animal Care (CCAC). Sprague-Dawley (SD) rats (200-250 g) were purchased from Charles River Laboratories (Wilmington, MA, USA). All initial drug doses were chosen empirically. Solid sodium carboxymethyl cellulose (NaCMC) and liquid Tween-80 solution ($1 \mu\text{L mL}^{-1}$) were purchased from Sigma Aldrich. Gelucire 44/14 and Peceol stock solutions were gifted from Gattefossé Canada. Nitric acid Optima and high purity hydrogen peroxide for digestion of ICP-MS samples were purchased from Fisher Scientific. Lanthanum and rhodium standards ($1000 \mu\text{g/mL}$ in 2% HCl) for standard curve calibration in ICP-MS were purchased from High Purity Standards. ICP-MS was run using an Agilent 7700x quadrupole machine equipped with an auto-sampler under the direction of Dr. Vivian Lai and Dr. Marghaleray Amini (PCIGR, Earth and Ocean Sciences, UBC). All glassware, vials, Eppendorf tubes, pipette tips etc. were prewashed by soaking overnight in HNO_3 (5%) and thoroughly rinsed with MQ water.

3.5.2 Drug preparation

$\text{La}(\text{dpp})_3$: Solutions for IV administration were prepared as 1 mg mL^{-1} $\text{La}(\text{dpp})_3$ in 10 % DMSO and sterile saline. CMC formulations were prepared as 15 mg mL^{-1} $\text{La}(\text{dpp})_3$ in 5 mL containing 2% NaCMC and 0.1% Tween-80. First, NaCMC (10 mg) was dissolved in 5 mL distilled water. $\text{La}(\text{dpp})_3$ (75 mg) and Tween-80 (5 μL) were then combined in a separate vial and thoroughly

mixed before adding the pre-prepared NaCMC solution, and the complete formulation was sonicated until all components were dissolved. CMC formulations were stored at 4 °C and used within 4 days of preparation. Gelucire/Peceol formulations were prepared as 15 mg mL⁻¹ La(dpp)₃ in 1 mL containing equal parts Gelucire 44/14 and Peceol stock solutions. Both stock solutions were warmed to 45 °C prior to preparation. La(dpp)₃ (15 mg) was vortexed for 2 minutes in 0.5 mL Gelucire 44/14 followed by the addition of 0.5 mL Peceol and vortexed for 5 minutes. The formulation was then sonicated for 5 minutes and mixed vigorously overnight at 45 °C prior to administration.

La(XT): Solutions for IV administration were prepared as 1 mg mL⁻¹ La(XT) in sterile saline. Oral solutions were prepared as 50 mg mL⁻¹ La(XT) in a 10 mL containing 1 mL glycerin and 9 mL sterile water, were thoroughly vortexed to dissolve and stored at 4 °C.

3.5.3 Drug administration protocol

All oral and IV formulations/solutions were adjusted to 37 °C prior to administration. For the single dose experiment, an IV injection of La(dpp)₃ (1 mg kg⁻¹) was administered *via* a pre-fitted jugular vein port. Blood samples (250 µL) were collected by IV catheter, mixed with 0.1 M EDTA (10 µL) and centrifuged for 10 minutes (15,000 rpm) to isolate the plasma, which was analyzed for lanthanum content by ICP-MS. Pharmacokinetic parameters were derived by non-compartmental analysis using Phoenix Software Ver. 1.3. For the acute (5-day) study IV injections of either La(dpp)₃ or La(XT) (1 mg kg⁻¹) were administered *via* a pre-fitted jugular vein port. For the short-term (1-month) study IV injections of either drug were administered *via* tail vein injection. Oral doses were administered *via* oral gavage (50 mg kg⁻¹). Blood samples were

collected directly from the tail vein and similarly prepared using 0.1 M EDTA and centrifugation to isolate the plasma.

At the end of all experiments, the animals were sacrificed and the spleen, liver, kidney, lungs, heart, brain, stomach, small intestine, and bones (left femurs) were collected. Soft organs were homogenized with saline (2 mL per gram of organ). Bones (femurs) were cleaned manually of all soft flesh and sectioned into knee, middle, and hip parts using a ceramic blade. Samples of either plasma, organ homogenate, or bone section were then dried (lyophilisation), accurately weighed, and prepared for ICP-MS analysis by digestion in HNO_3 (2 mL) and H_2O_2 (2 mL), gradually increasing the temperature over 48 hours from 90 °C to 130 °C and evaporating to dryness. The residues were taken up in 2 % HNO_3 containing 10 ppb Rh as an internal standard and analyzed for their lanthanum content (see Appendix for calibration curve).

Chapter 4: Lanthanum complexes of dipicolinic acid (dpa)-ligands for the treatment of resorption disorders: Design, synthesis, and preliminary studies

4.1 Introduction and motivation

Thus far, the lanthanum complexes of two different chelating ligand systems have been thoroughly investigated as potential candidates for oral drugs which deliver La^{3+} to bone tissue *in vivo*, whereupon it has the potential to invoke a positive therapeutic effect on the sufferers of bone resorption disorders. One system, Hdpp, is based on the 3-hydroxy-4-pyridinone scaffold, which forms stable *tris*-metal complexes with La^{3+} . Although $\text{La}(\text{dpp})_3$ appears to suffer from a lack of thermodynamic stability *in vivo*, the scaffold itself has the advantage of being easily modified at the *N*-position to incorporate a range of functionalities without impacting the bidentate metal binding cavity.^{67,69} Conversely, as the 1:1 complex with La^{3+} , H_5XT (the other system under scrutiny) exhibits much greater thermodynamic stability under physiological conditions due to a higher inherent denticity;^{68,69} however, a distinct lack of obvious points of derivatization prevents diversification of this particular design, and therefore limits any potential system optimization.

In an effort to combine favourable attributes of both Hdpp and H_5XT , a new-generation system based on a dipicolinic acid (dpa) motif is proposed (Figure 4.1). The ligand scaffold consists of two picolinic acid (pa) groups connected *via* methylene bridges at the 6-position of each pa to a central *N*-atom, resulting in a metal binding cavity that is inherently 5-coordinate (N_3O_2). The central nitrogen offers a convenient handle for functionalization, which allows tuning and optimization of a number of key properties of the ligand, including the ability to target bone mineral, lipophilicity, and thermodynamic stability of the lanthanum complex.

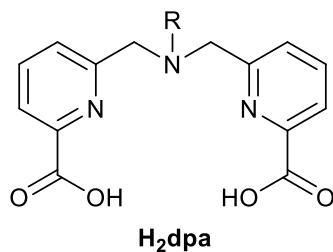


Figure 4.1 General structure of H₂dpa, where R is a functional group designed to enhance metal chelation and/or bone targeting.

4.1.1 The “pa” family of ligands as acyclic chelators for radiometals

The inspiration for the design presented in Figure 4.1 originates from previous work within our group, in which acyclic ligands based on a similar dpa binding motif were investigated as bifunctional chelators for a number of radiometals which are used to image, diagnose, and treat cancer.⁸⁹ In those cases, the aim is to closely match the binding cavity of the ligand to a specific radioactive metal, invoking systems that: coordinate the metal rapidly and quantitatively at room temperature; display very high complex thermodynamic stability *in vivo* (even at very low concentrations); and do not surrender the radiometal to endogenous binding species (such as proteins and enzymes).⁸⁹ Much of this work is based upon the *N,N'* dpa-ethylenediamine (en) ligand scaffold H₂dedpa (Figure 4.2), which exhibits favourable coordination properties and high *in vivo* stability as the unfunctionalized (R = H) chelator with both gallium-67 (used in SPECT imaging) and gallium-68 (used in PET imaging).⁹⁰ Substitution of the hydrogen atoms at the two secondary amines can tailor the scaffold to serve a number of specific functions (summarized in Table 4.1), including hypoxic cell and tissue targeting with nitroimidazole (NI) moieties;⁹¹ heart uptake with ethoxylated phenyl residues;⁹² and inclusion of a handle for antibody conjugation with *para*-isothiocyanate benzyl groups.⁹³ Furthermore, by derivatization at that same position with

metal binding moieties, the ligand's inherent denticity and donor environment can be modified to better suit other radiometals of interest. Examples include the *N,N'* carboxylated ligand H₄octapa, shown to be suitable for radiolabelling with ¹¹¹In and ¹⁷⁷Lu;⁹⁴ the benzylated trinitroimidazole functionalized derivative H₂azapa for ⁶⁴Cu radiolabelling;⁹⁵ and the methylphosphonate-based chelator H₆phospa, intended to label ⁸⁹Zr.⁹⁶

While the versatility of these systems is apparent, there are two crucial reasons why the smaller H₂dpa scaffold (Figure 4.1) was selected for this project, and not the larger, more established H₂dedpa scaffold (Figure 4.2). First is the intended function of the system: metal complexes of H₂dedpa and related compounds are designed to exhibit very high *in vivo* thermodynamic stability, and not release the metal to endogenous binding groups; however, an ideal system for this project should be labile enough to relinquish La³⁺ to bone tissue. Second is synthetic accessibility: many of the H₂dedpa derivatives presented in Table 4.1 require multi-step syntheses and tedious purification, leading to compromised yields. While synthetic efficiency should always be a consideration, the quantities required for radiochemical labelling are significantly less than those required for an oral drug. For this reason, we rationalize that the smaller, simpler scaffold H₂dpa will be more suitable, in requiring fewer synthetic steps.

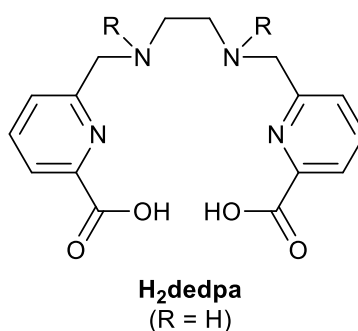
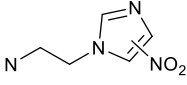
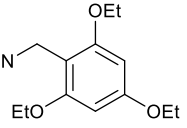
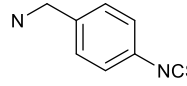
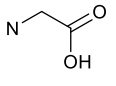
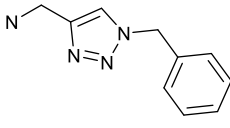
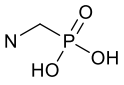


Figure 4.2 The H₂dedpa scaffold, which forms the basis for a number of acyclic dipicolinic acid-based chelators which can be modified to tailor both *in vivo* targeting and radiolabelling properties (see Table 4.1).

Table 4.1 Summary of the range of the ways in which H₂dedpa (Figure 4.2) can be modified to either target specific *in vivo* functionality (upper), or to bind radiometals other than gallium-67/68 (lower).

N-R =	Name	Intended function	Ref.
	<i>N,N'</i> -et-2NI-H ₂ dedpa	Hypoxia imaging	91
	<i>N,N'</i> -me-2,4,6-OEt-Ph-H ₂ dedpa	Myocardial imaging	92
	<i>N,N'</i> - <i>p</i> -SCN-Bn-H ₂ dedpa	Antibody conjugation	93
N-R =	Name	Intended radiometal	Ref.
	H ₄ octapa	¹¹¹ In, ¹⁷⁷ Lu	94
	H ₂ azapa	⁶⁴ Cu	95
	H ₆ phospa	⁸⁹ Zr	96

4.1.2 The H₂dpa scaffold

In a radiopharmaceutical context, studies exploring the suitability of H₂dpa-based ligands for radiolabelling purposes are limited to smaller metal ions such as copper and technetium;⁹⁷ however, primarily thanks to the work of Mazzanti *et al.*, there are a number of literature examples which probe the chemistry of functionalized H₂dpa ligands with trivalent lanthanides, as well as their potential medicinal applications. These include the *tris*(aqua) Gd(III) complex with *N*-carboxylated dpa as an MRI contrast agent;⁹⁸ similar complexes of Eu(III) and Tb(III) as luminescent probes;⁹⁹ and Tb(III)-containing coordination polymers also exhibiting luminescence,

which are formed by self-assembly with divergent *N,N*-bridged dpa ligands.¹⁰⁰ Taking the first case as an example, the ligand 6,6'-{[(carboxymethyl)azamediy]bis(methylene)}dipicolinic acid (abbreviated to H₃dpaa for that study) binds Gd³⁺ in a 1:1 ratio with three bound inner-sphere water molecules, and even though dpaa³⁻ does not fully saturate the coordination sphere of the metal ion, the complex exhibits good stability under physiological conditions.⁹⁸ Furthermore, it was noted that – in spite of being charge neutral – the complex shows high aqueous solubility, which is a desirable property in the context of avoiding the need for oral drug formulation.

Herein, we present a set of *N*-functionalized H₂dpa derivatives (Figure 4.3) – as well as their corresponding La³⁺ complexes – which have been synthesized, characterized, and subjected to a number of testing procedures to assess their suitability as orally-administered chaperones for delivering lanthanum to bone tissue. The functionalized ligands include either a carboxylate (6,6'-{[(carboxymethyl)azamediy]bis(methylene)} dipicolinic acid = **H₃cedpa**), phosphonate (6,6'-{[(2-phosphonoethyl)azamediy]bis(methylene)} dipicolinic acid = **H₄pedpa**), or bisphosphonate (6,6'-{[(4-hydroxy-4,4-diphosphonobutyl)azamediy]bis (methylene)} dipicolinic acid = **H₇alenpa**) moiety. Also included in these studies is the unfunctionalized version (6,6'-[azamediy]bis(methylene)} dipicolinic acid = **H₂dpa**), which enables a calibrated assessment of the effect of each of these functional groups. As well as the synthetic procedures required to access these compounds, we aimed to assess bone targeting ability of the ligands through HAP binding studies (akin to the solution depletion studies presented in Chapter 2); contribution to complex stability of a phosphonate group through potentiometric titrations; and expected cell permeability through lipophilicity measurements (and the effect metal chelation has on these values). In addition to these solution-based studies, the solid-state crystal structure of the 1:1 lanthanum complex of H₄pedpa is described.

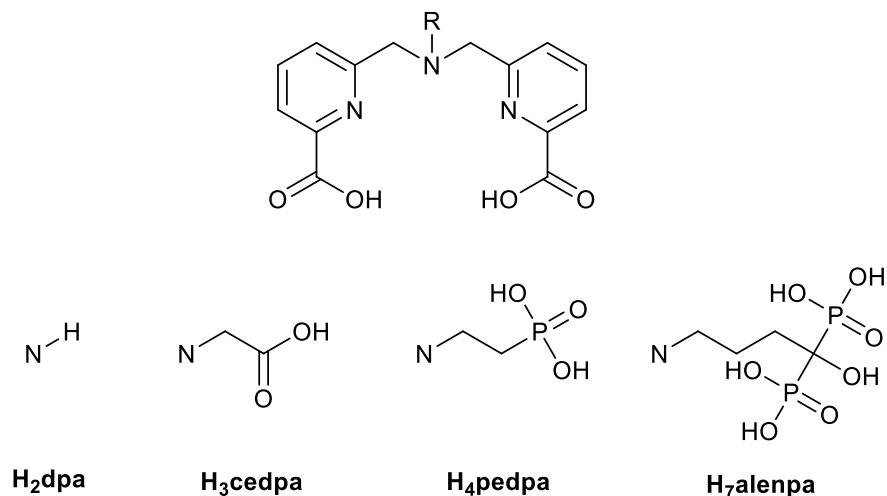


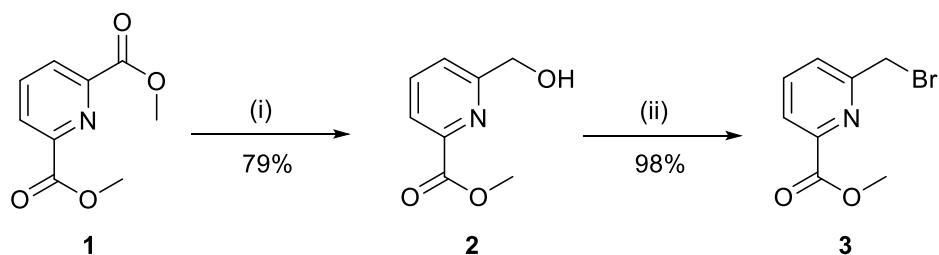
Figure 4.3 The names and structures of the four picolinic acid-containing ligands explored in this chapter.

4.2 Results and discussion

4.2.1 Synthesis of the dpa ligands

The synthetic routes to all four dpa-based compounds – H₂dpa, H₃cedpa, H₄pedpa, and H₇alenpa – rely on the alkylating agent methyl 6-(bromomethyl) picolinate (**3**), which is generated in large quantities and good yields in a two-step process (mono-reduction followed by bromination) *via* a hydroxyl intermediate (**2**) from the relatively cheap commercially available starting material dimethyl pyridine-2,6-dicarboxylate (**1**) (Scheme 4.1). The alkyl-protected ligands are then generated from **3** *via* a double *N*-alkylation of the primary amine synthon that corresponds to the desired compound, followed by a deprotection (for all except H₇alenpa, in which the deprotected product is generated during alkylation) in strong acid to obtain the final ligands as the HCl salts (Scheme 4.2 to 4.5). Because of the quantities that could eventually be required for *in vivo* testing, significant efforts were undertaken to optimize each synthesis to give maximal yields in minimal steps.

Scheme 4.1 Synthetic route to the alkylating agent methyl 6-(bromomethyl) picolinate (**3**).^a

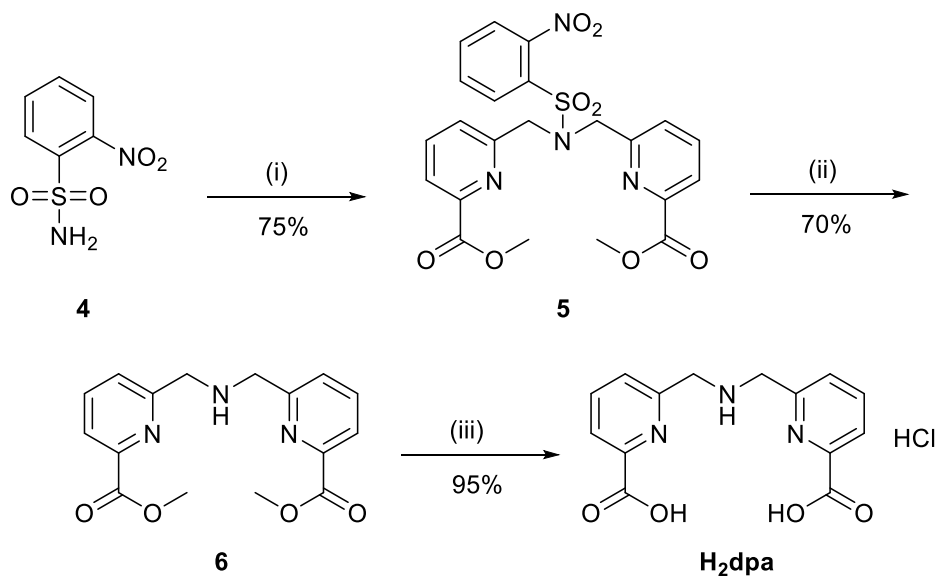


^a Reagents and conditions: (i) NaBH₄ (1.2 eq.), DCM/MeOH (7/3), 2.5 h, 0 °C to RT; (ii) PBr₃ (1.05 eq), CHCl₃, 2 h, 0 °C to RT.

For H₂dpa – since the final product is the secondary amine – an additional 2-nitrobenzenesulfonamide (**4**) (nosyl)-mediated protection-deprotection step is required (Scheme 4.2). This chemistry was optimized by Dr. Eric Price (Ph.D. 2014, Medicinal Inorganic Chemistry Group, UBC) in the syntheses of the larger acyclic chelators H₂dedpa and H₄octapa, and enables good yields and straightforward purification compared to other amine protecting groups.⁹⁴ The synthesis of H₃cedpa is more straightforward as it only requires *N*-alkylation of the commercially available glycine ethyl ester (hydrochloride salt) (**7**) prior to deprotection (Scheme 4.3), and a similar procedure has been previously reported.⁹⁸

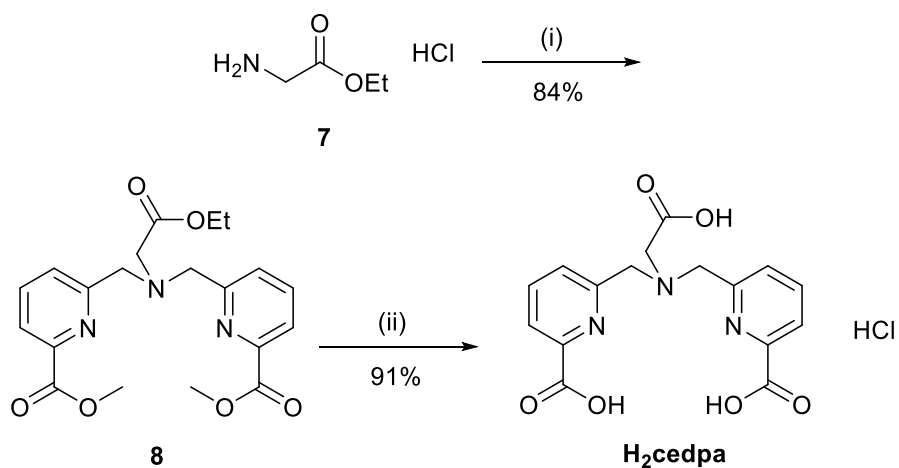
The primary amine synthon (**10**) required to make H₄pedpa is not commercially available, but can be synthesized in a single step and under mild conditions *via* an aqueous-mediated catalyst-free aza-Michael addition of diethyl vinylphosphonate (**9**) with ammonium hydroxide.¹⁰¹ One drawback of this procedure is the tendency for overreaction to occur *via* subsequent 1,4-additions into the vinylphosphonate Michael-acceptor from the more active amines that are formed, resulting in *bis*- and *tris*-phosphorylated by-products (Scheme 4.4 upper); however, this can be minimized by the very gradual addition of **9** into a large excess of ammonium hydroxide solution.

Scheme 4.2 Synthetic route to H₂dpa as the HCl salt.^a



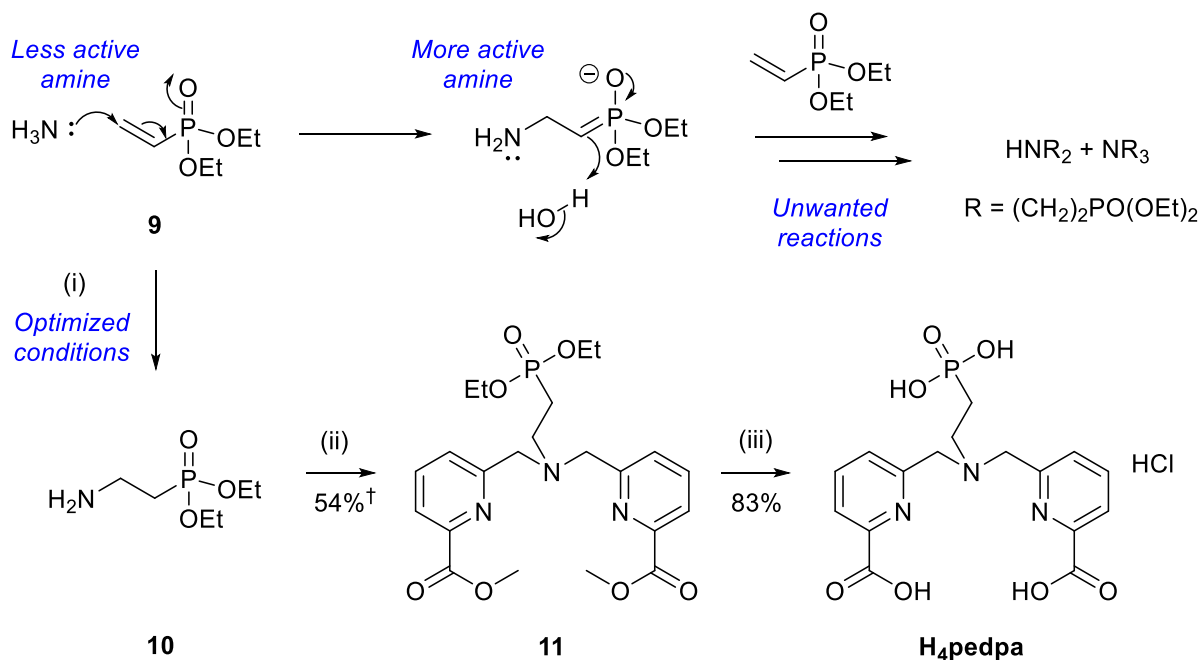
^a Reagents and conditions: (i) **3** (2.1 eq.), K₂CO₃, CH₃CN, 60 °C, 24 h; (ii) PhSH (1.1 eq), THF, 70 °C, 48 h; (iii) 6 M HCl, 110 °C, 12 h.

Scheme 4.3 Synthetic route to H₃cedpa as the HCl salt.^a



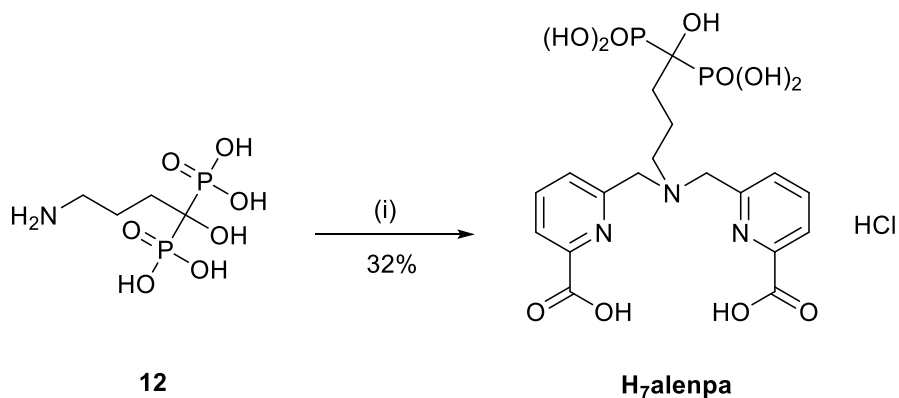
^a Reagents and conditions: (i) **3** (2.1 eq.), K₂CO₃, CH₃CN, 60 °C, 12h; (ii) 6 M HCl, 110 °C, 12 h.

Scheme 4.4 Aza-Michael addition mechanism and synthetic route to H₄pedpa as the HCl salt.^a



^a Reagents and optimized conditions: (i) Excess NH₄OH (aq.), H₂O, 0 °C to RT, 12 h; (ii) **3** (2.1 eq.), K₂CO₃, 60 °C, 12 h; (iii) 12 M HCl, 110 °C, 12 h. † Yield over two steps.

Scheme 4.5 Synthetic route to H₇alenpa as the HCl salt.^a



^a Reagents and conditions: (i) **3** (3.0 eq.), H₂O/THF (3/1), 1 M NaOH (pH 12), 3 d (followed by acid workup).

In spite of the optimized conditions, such is the activeness of the primary amine **10** relative to ammonia, that a small quantity of unwanted by-products invariably form, which – given the oily consistency of the alkyl phosphonates and the absence of a chromophore – are very challenging to separate. This was addressed by directly alkylating the crude reaction mixture from step (i) in Scheme 4.4, followed by column separation to isolate the desired dimethyl picolinate intermediate **11**, which was deprotected in strong acid in a manner similar to that for the other compounds.

Finally, because of difficulties in obtaining the necessary alkyl-protected primary amine synthon, H₇alenpa was accessed in a single step *via* a pH-controlled aqueous reaction of **3** with alendronic acid (**12**). Because of the basicity of the primary amine group of **12** (pK_a 12.7),¹⁰² a pH between 12 and 13 was maintained throughout the course of the reaction by regular dropwise addition of 1 M NaOH. This has the simultaneous effect of removing the alkyl protecting groups of the picolinate arms; however, unwanted bromide hydrolysis prevented the attainment of good yields despite efforts to optimize the reaction conditions. A similar reaction procedure (with high yields) has been previously reported in the synthesis of bone-seeking chelating ligands for ^{99m}Tc, but in those cases the alkylating agent was simply 2-(chloromethyl) pyridine (no carboxylate functionality), which may explain the improved efficiency.¹⁰³

All four compounds were characterized by ¹H and ¹³C NMR spectroscopy, low and high resolution mass spectrometry, and elemental analysis. The phosphorous-containing compounds were further characterized by ³¹P{¹H} NMR spectroscopy, and crystals suitable for solid-state X-ray analysis for H₂dpa·H₂O, H₃cedpa·H₂O (respectively Dr. Lisa Murphy and Dr. Caterina Ramogida, Medicinal Inorganic Chemistry Group, UBC), and H₄pedpa·3H₂O were obtained as zwitterions and the structures were solved by Dr. Brian Patrick (Appendix). The full synthetic procedures and associated analyses are presented in the experimental section of this chapter.

4.2.2 Solution depletion studies of dpa ligands with HAP

In Chapter 2.4.3, solution depletion studies with HAP and either La(dpp)₃ or La(XT) were presented. In those cases, the aim was to determine how the presence of either ligand system influenced the natural tendency for La(III) to exchange with Ca(II) in bone mineral by following the concentration of lanthanum in solution over time by ICP-MS. The fate of the ligand was of less concern, particularly since the interaction of either ligand system with bone mineral had already been demonstrated by ITC (with Hdpp showing a negligible interaction with HAP, and H₅XT showing a weak interaction with HAP). It was also shown that attempting to observe multiple possible overlapping kinetic events in a single experiment of this nature led to results that were quite convoluted, and challenging to interpret.

With the new dpa-based ligands in hand, a similar (but more straightforward) set of experiments were performed in which the influence of the R-appendage on bone mineral targeting and binding was examined by performing solution depletion studies with each of the four ligands in the absence of a chelated metal ion. Ligand solutions (0.1 mM) buffered to pH 7.4 were incubated and agitated (37 °C and 220 rpm) with a suspension of synthetic HAP (in 200-fold excess), and at fixed time points over the course of 48 hours the concentration of ligand remaining in solution (not bound to HAP) was determined by UV-Vis spectrometry. Although this analytical technique does not offer the same level of accuracy or sensitivity as ICP-MS does for La(III), it is vastly cheaper and significantly quicker to perform. The results (Figure 4.4) are plotted as % [ligand] remaining in solution relative to [ligand]_{t=0} *versus* time in hours.

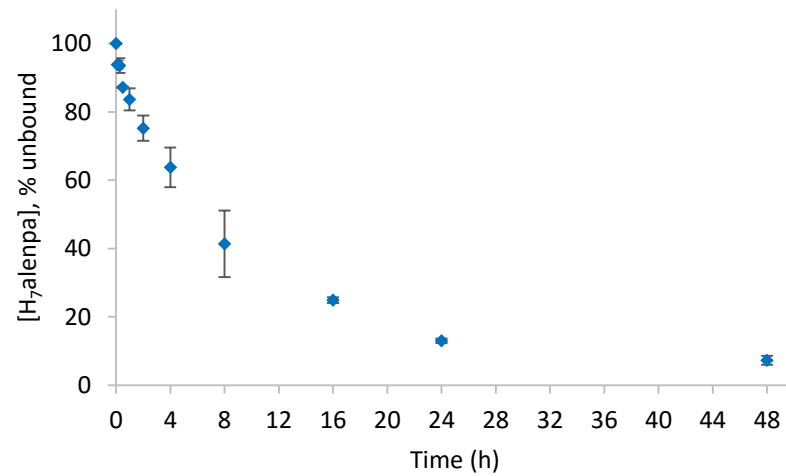
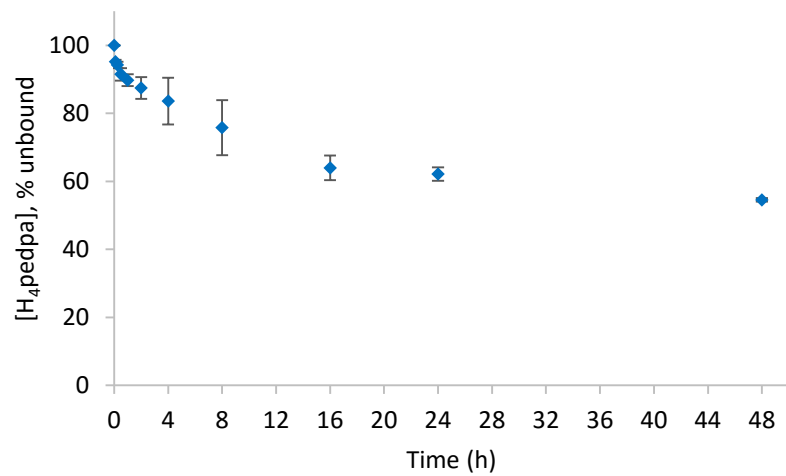
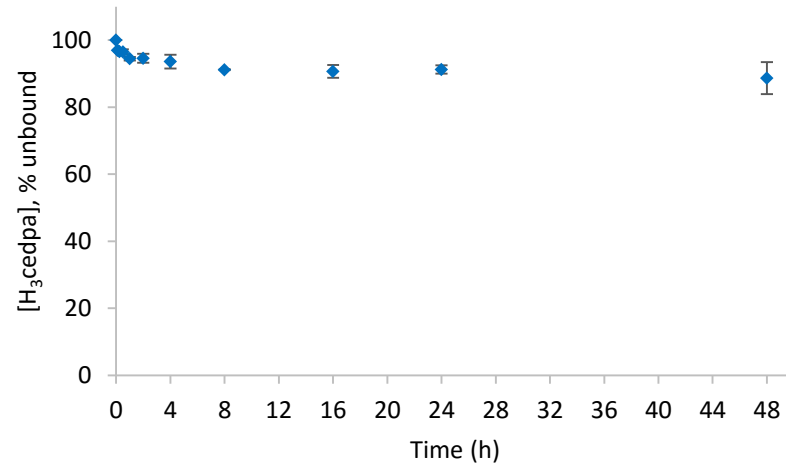
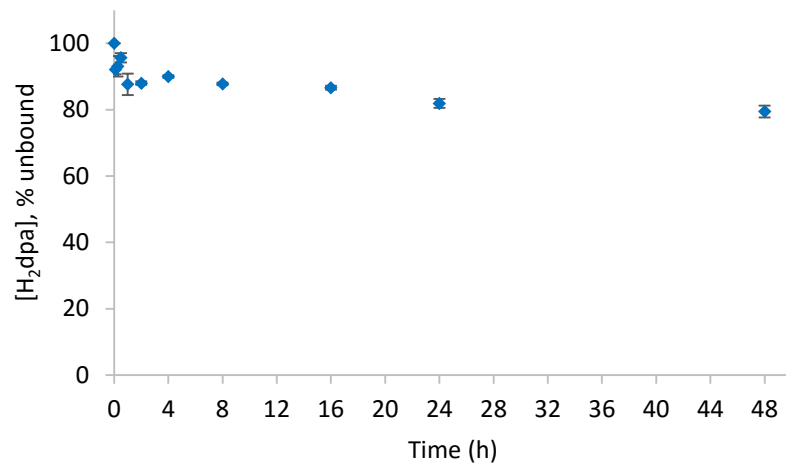


Figure 4.4 Solution depletion plots showing the [ligand] remaining in solution (unbound to HAP) over 48 hours as a % of [ligand] at time = 0 hours ($n = 3$). Conditions for all experiments: 37 °C, pH 7.4, $I = 0.16$ M (NaCl), agitation at 220 rpm. **A:** H₂dpa; **B:** H₃cedpa; **C:** H₄pedpa; **D:** H₇alenpa.

Figure 4.4 **A** shows the disappearance of H₂dpa (R = H) from solution to an approximate minimum of [H₂dpa] = 80% after 48 h, with the other 20% presumably bound to HAP. Although there is very little error associated with the data, the first few time points are erratic and incoherent from a kinetic point of view, and this – coupled with the fact that the majority of the compound remains in solution – infers that there is little to no chemical attraction between H₂dpa and HAP. This is consistent with other compounds which do not contain specific bone binding groups (such as a phosphonate or bisphosphonate), and the minimal disappearance from solution that is observed is likely due to physisorption in the form of weak van der Waals interactions between solvated H₂dpa and suspended HAP particles.

A similar argument can be made to explain the results for H₃cedpa (Figure 4.4 **B**), which also does not contain any functionality that specifically binds to bone mineral. As with H₂dpa, a slight depletion from solution is observed to a minimum [H₃cedpa] of approximately 85% after 48 h, which is again likely due only to physical adsorption onto the surface of HAP particles.

The observed depletion profile changes significantly with the introduction of the phosphonate moiety in H₄pedpa (Figure 4.4 **C**). In this case, the concentration of the ligand in solution disappears in a smooth and coherent manner to a minimum [H₄pedpa] in solution of around 55% after 48 h. This is indicative of a process involving chemical absorption, consistent with the ability of phosphonates to bind to HAP with moderate strength.¹⁰⁴ An effort was made to extract a rate equation for this binding process; however, neither the first nor second order rate plots exhibited clear linearity (Figure 4.5). This suggests an overall order dependence on H₄pedpa of between 1 and 2, and is possibly indicative of a process in which both chemisorption and physisorption occur simultaneously, and to a similar degree.

With H₇alenpa (Figure 4.4 **D**), the compound binds rapidly to HAP and is almost undetectable in solution (<10% remaining) after 48 h. This follows the notion that bisphosphonate-based systems exhibit very high affinity for bone mineral by mimicking the pyrophosphate network found in HAP (see Section 1.4.3), and of the four systems tested, H₇alenpa is best suited to target bone. A plot of the natural log of % [H₇alenpa] *versus* time gives a near-linear plot ($R^2 = 0.996$, Figure 4.6) indicative of a *pseudo*-first order adsorption process. The slope of the plot gives a rate constant $k = 0.1017 \text{ h}^{-1}$, and the overall differential rate law is given in equation 4.1. While the lack of concise kinetic data from the other three compounds renders it challenging to contextualize this information quantitatively, it is clear that there is a marked increase in affinity for bone mineral as one goes from carboxylic acid, to phosphonate, to bisphosphonate.

$$Rate_{(\text{adsorp.})} = 0.1017[\text{H}_7\text{alenpa}] \quad (\text{Equation 4.1})$$

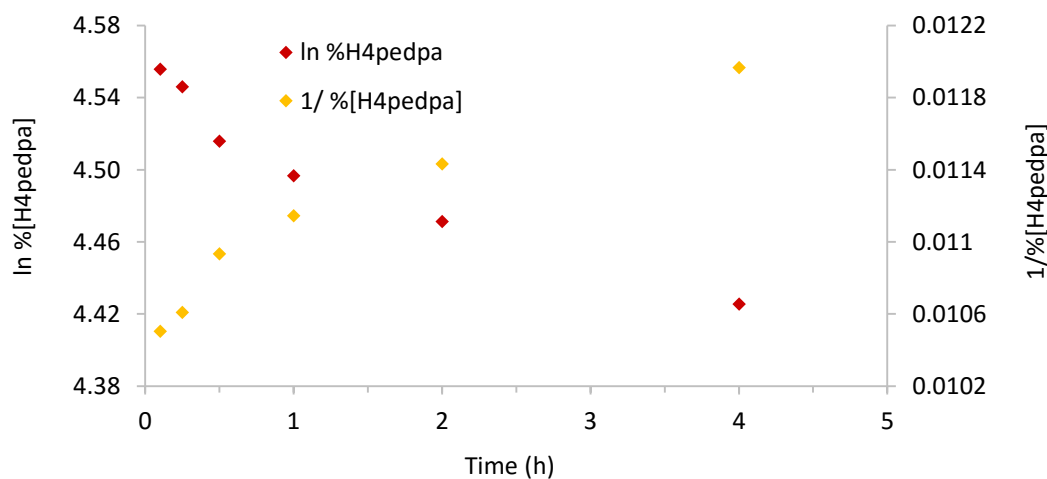


Figure 4.5 A plot of the natural log (red) and the inverse (yellow) of [H₄pedpa] vs. time derived from the data presented in Figure 4.4 C. The data suggest an order dependence on [H₄pedpa] between 1 and 2.

From these results – and from previous studies³⁵ – it is clear that BP containing compounds have some of the greatest bone-directing capability of any organic moiety; however, one of the major cautions associated with the use of BP-based pharmaceuticals is their tendency to become incorporated into newly mineralized tissue, where they can be retained with an elimination half-life exceeding 10 years.¹⁰⁵ This long-term retention is often cited as the reason for some of the major side-effects associated with chronic oral administration of BPs,⁴⁰ and serves as one of the arguments for why alternative treatments (e.g. lanthanum-based compounds) should be explored. For this reason, the weakly bone-directing mono-phosphonate compound H₄pedpa may – in the context of the new set of ligands – present a more viable option for facilitating the inherent bone-targeting ability of La(III), without itself impacting bone histology through long-term ligand accumulation.

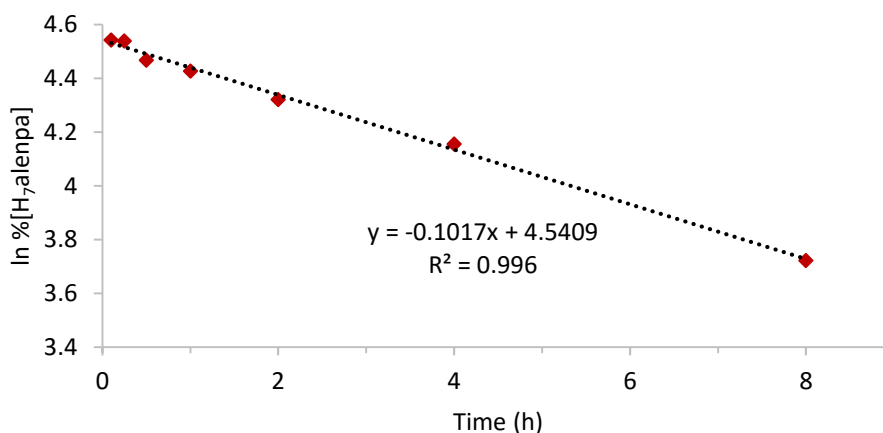


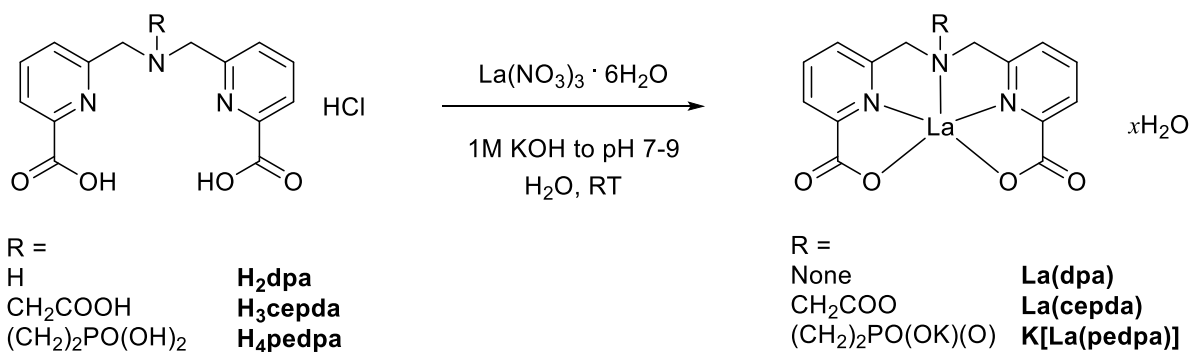
Figure 4.6 A plot of the natural ln [H₇alenpa] *versus* time, giving an approximately linear plot and a first order rate constant $k = 0.1017 \text{ h}^{-1}$.

4.2.3 La(III) complexes of the dpa ligands

4.2.3.1 Synthesis and characterization of the La(III)-dpa complexes

The 1:1 lanthanum complexes of H₂dpa, H₃cedpa, and H₄pedpa were successfully synthesized by adjusting the pH of an equimolar mixture of either of the ligands and lanthanum nitrate hexahydrate in water using 1 M KOH (Scheme 4.6). As the HCl salts, the compounds themselves were soluble in water and resulted in a pH between 1 and 2. After the addition of lanthanum nitrate, the pH was raised very gradually (taking care to allow the pH of the solution to fully equilibrate before the addition of further base) in order to discourage the formation of insoluble lanthanum hydroxides. When a basic pH was obtained, the solutions were concentrated and the complexes precipitated by the progressive addition of methanol and acetone, and collected by filtration before thoroughly drying under vacuum. Attempts to perform an analogous synthesis with H₇alenpa invariably resulted in the formation of a precipitate at low pH levels, which was challenging to analyze due to poor solubility. This is likely due to the high affinity and multiple possible binding modes between the bisphosphonate moiety and trivalent lanthanum as well as the intended chelate cavity (divergent to the BP moiety), which leads to the incoherent and irregular formation of various polymeric structures rather than the intended 1:1 complex.

Scheme 4.6 General procedure for the synthesis of the 1:1 lanthanum complexes of three dpa-based ligands.



The neutral (La(dpa) or La(cedpa)) or charged ([La(pedpa)]⁻) complexes were all found to be water soluble and were characterized by ¹H and ¹³C NMR spectroscopy, low and high resolution mass spectrometry, and – in the case of K[La(pedpa)] – ³¹P{¹H} NMR spectroscopy. Precisely matching elemental analyses were challenging to obtain due to the hygroscopic nature of the complexes. In all cases, the most useful tool in characterizing the formation of the metal complexes was ¹H NMR spectroscopy which – upon ligand chelation to lanthanum – showed a clear and well-defined upfield shift and diastereotopic splitting of the methylene protons adjacent to the central nitrogen (Figure 4.7 and Appendix). This occurs as the two 5-membered chelate rings formed in the binding cavity involving lanthanum, the central sp³ nitrogen, and the nitrogen atoms of a pyridine ring, pucker about the unconjugated methylene carbon atoms to reduce strain. The resulting system is skewed, and the non-equivalent hydrogen atoms on adjacent Py-CH₂-N chains couple to one another to give the diagnostic pattern shown.

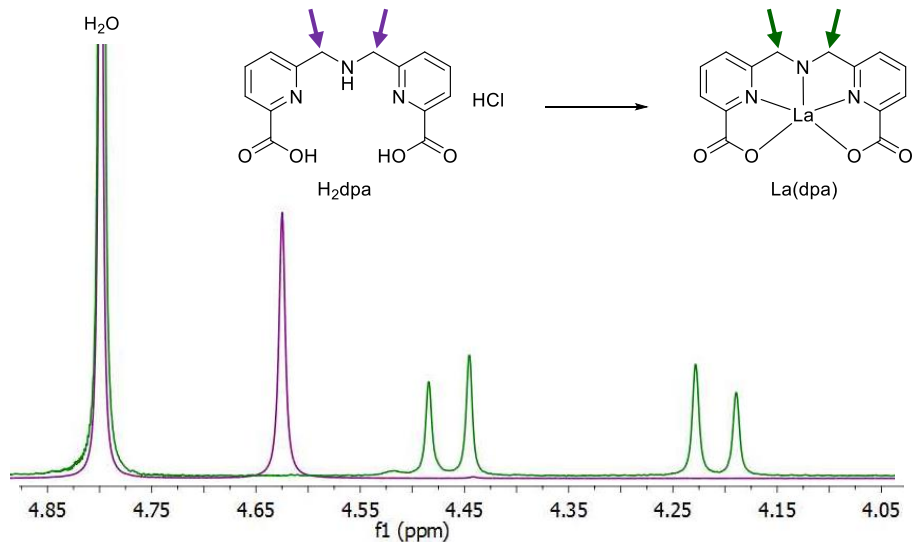


Figure 4.7 Portion of ¹H NMR spectrum showing the typical upfield shift and diastereotopic splitting of the methylene protons (marked) observed upon chelation of the dpa ligands to lanthanum (400 MHz, D₂O, 298 K). The full ¹H NMR spectra are presented in Appendix.

Table 4.2 Comparison of the chemical shifts (δ) and coupling constants (2J) of the backbone methylene protons in the lanthanum complexes of the three dpa ligands.

Complex	δ (H _a , ppm)	2J (Hz)	δ (H _b , ppm)	2J (Hz)
La(dpa)	4.45	16	4.19	16
La(cedpa)	4.16	16	4.01	16
La(pedpa) ⁻	4.15	15	3.87	15

The ^1H NMR spectra of the three lanthanum complexes each exhibit a similar diastereotopic splitting pattern, with sharp, well resolved peaks indicative of a single isomer in solution and no observable interconversion at room temperature. The methylene- H signals appear at approximately the same chemical shift in the three different complexes, and there is minimal variance in the values of the 2J coupling constants (Table 4.2). This invokes a high degree of solution-based structural similarity between the three complexes, and suggests that the binding of La(III) in the dpa cavity is not affected by functionalization of the backbone nitrogen group.

4.2.3.2 Crystal structure of [La₄(pedpa)₄(H₂O)₂]

As was highlighted in Chapter 2.4, crystals of an adequate size and quality for solid-state structural refinement by X-ray crystallography of coordinatively unsaturated lanthanide complexes can be difficult to obtain due to unusual geometries, variable coordination numbers, and propensity for Ln(III) to bind inner-sphere water molecules. Numerous attempts were made to grow crystals with the three compounds described above (as well as dpa complexes with other lanthanides); however, all were in vain with the exception of the 1:1 complex of La(III) with H₄pedpa. In this case, colourless prismatic crystals suitable for solid-state X-ray analysis were obtained by the slow diffusion of methanol into a concentrated solution of the premade K[La(pedpa)] complex in water.

The structure was solved by direct methods (Dr. Brian Patrick). Residual electron density was present in the lattice presumably due to solvent and counter-ion, but unfortunately none of these sites could be properly modeled as either water, methanol, or K^+ , likely due to disorder. As a result, a data set free of solvent/ions at those sites was generated using the PLATON/SQUEEZE program.¹⁰⁶ All non-hydrogen atoms were refined anisotropically, and all O-H hydrogen atoms were located in difference maps and refined isotropically. All other H atoms were placed in calculated positions.

The material crystallized as an lanthanum tetramer, with two asymmetric units (AU and AU') related to one another by inversion symmetry, and each containing two unique lanthanum centres (La1 and La2); two molecules of pedpa (pedpa1 and pedpa2); and one molecule of H_2O bound to La2 (Figure 4.8). La1 is 8-coordinate, forming bonds with the five inherent donor atoms (N_3O_2) from the binding cavity of pedpa1. The coordination sphere is completed by three phosphonate oxygen atoms: one from pedpa1, one from pedpa2, and one from pedpa1' (from the other asymmetric unit). A result of this third coordinating oxygen is the formation of an 8-membered ring bridging the asymmetric units, and containing La1, La1', and an O-P-O linker from pedpa1 and pedpa1'. La2 is 9-coordinate, with five sites similarly occupied by donor atoms from the dpa scaffold of pedpa2, and a phosphonate oxygen from the same unit. La2 also bonds two oxygen atoms from pedpa1, which both stem from the same picolate arm. The final coordination site occupied by a molecule of H_2O , which is the only well resolved solvent molecule found within the lattice, bound within the inner-sphere of La2 at a La-O distance of 2.501 Å, and stabilized by hydrogen bonding interactions to pedpa1. As is often the case with non-rigid complexes of the lanthanides, there is a lack of clear and well-defined coordinate geometry around either lanthanum centres; however, a curious point to note is the semblance between the two La(III) environments

shown here, and the two Ca(II) environments present in solid HAP (see Chapter 1.2), emphasizing the similarity between these two ions.

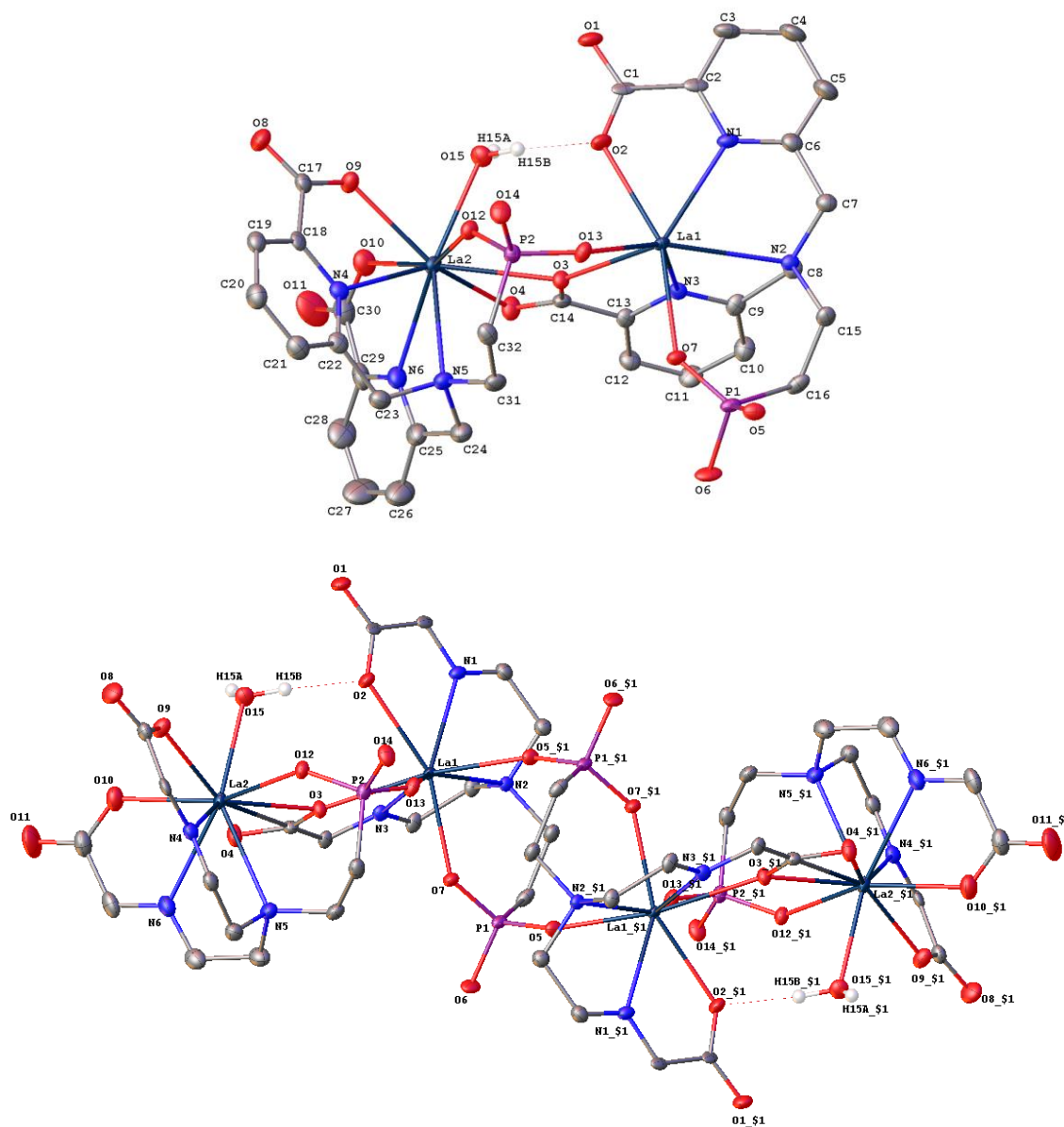


Figure 4.8 ORTEP diagram of the crystal structure of tetrameric $[La_4(pedpa)_4(H_2O)_2]$ solved by direct methods by Dr. Brian Patrick (UBC) and modeled without lattice solvent, showing the asymmetric unit (upper) and the complete unit cell (lower) consisting of two asymmetric units. All hydrogen atoms (with the exception of those on water bound to La2) omitted for clarity, as well as the C-H groups of the pyridine rings in the unit cell diagram.

Table 4.3 Crystallographic data.

La₄(pedpa)₄(H₂O)₂	
Formula	C ₆₄ H ₆₀ La ₄ N ₁₂ O ₃₀ P ₄
Formula weight	2156.76
Crystal system	Triclinic
Space group	<i>P</i> -1 (#2)
Lattice type	Primitive
Lattice parameters	<i>a</i> = 11.627(3) Å <i>α</i> = 78.25(2)° <i>b</i> = 12.924(5) Å <i>β</i> = 82.39(3)° <i>c</i> = 16.027(7) Å <i>γ</i> = 66.56(2)°
Lattice volume	2160(2) Å ³
<i>Z</i>	1
<i>D</i> _{calc'd}	1.658 g/cm ³
<i>F</i> (000)	1056.00
<i>μ</i> (MoK α)	20.94 cm ⁻¹
Reflections collected	41455
Unique reflections	12524
Reflections with <i>I</i> ≥ 2.00σ(<i>I</i>)	9249
R _{int} ; R ₁ ; wR ₂	0.035; 0.041; 0.088
GofF on <i>F</i> ²	1.01

Table 4.4 Selected bond lengths and angles.

Bond	Length (Å)	Angle	<i>θ</i> (°)
La1-N1	2.677(3)	N1-La1-N3	85.68(10)
La1-N2	2.863(3)	N4-La2-N6	83.60(11)
La1-N3	2.708(3)		
La2-N4	2.679(4)		
La2-N5	2.861(4)		
La2-N6	2.673(3)		
La2-O15	2.501(3)		

It is worth noting that – for both La1 and La2 – lanthanum does not sit flush within the dpa cavity of pedpa, but rather outside of it, with the ligand bent in such a way as to push the two picolinate arms towards each other (N^{Ar}-La-N^{Ar} *θ* < 90°, Figure 4.9) enforcing a facial binding mode, and the (CH₂)₂PO(O)₂ arm wrapping around the other side of the metal enabling bridging between La1 and La2. This shows that the dpa scaffold on its own is not well suited to the ionic radius of La(III), which is unsurprising given that typical Ln(III) chelating ligands (that are

designed to bind tightly and irreversibly) usually include much larger binding cavities and inherent coordination numbers of 8 or more;¹⁰⁷ however, this mismatch in size between metal and ligand can be construed as a positive feature of these systems, as an ideal target compound must be able to surrender the metal ion to bone mineral after it has been absorbed.

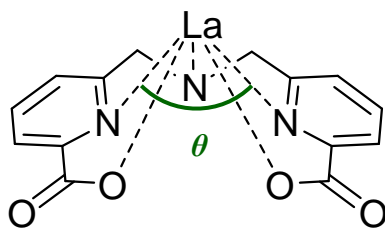


Figure 4.9 ChemDraw representation of the facial binding mode and acute N-La-N bond angle adopted by the dpa cavity in the solid-state structure of $[\text{La}_4(\text{pedpa})_4(\text{H}_2\text{O})_2]$.

Also worth highlighting are the La-N^f bond distances (La1-N2 = 2.863(3) Å; La2-N5 = 2.861(4) Å), which are both greater than the sum of the effective ionic radii for lanthanum and nitrogen in their respective coordination environments (La³⁺_{CN9} = 121.6 pm; N³⁻_{CN4} = 146.0 pm).¹⁰⁸ This implies that there is only a partial bonding interaction between these atoms, and that functionalization of the backbone nitrogen should not detract from the lanthanum binding properties of the dpa scaffold. Similar phenomena have been reported in which weak lanthanum(III)-tertiary amine interactions (of a similar distance apart) are stabilized by strong chelation across the rest of the molecule.¹⁰⁹ Furthermore, the diastereotopic splitting and shielding of the methylene hydrogens observed in the ¹H NMR spectrum of La(pedpa) also implies an interaction between these two atoms.

As was the case with La(dpp)₃, a cautious approach should be taken when attempting to extrapolate informative conclusions from the solid-state structure of a material that is ultimately intended to be used in solution (and more importantly *in vivo*). Nonetheless, the crystal structure presented here for the La(pedpa) tetramer provides a visually compelling insight into the nature of the interaction between La(III) and ligands based on the dpa motif, and enables well-informed guidance on the design of future compounds.

4.2.4 Speciation plots and thermodynamic stability constants of La(dpa) and La(pedpa)

Thermodynamic data of inorganic complexes in aqueous solution provide a powerful means by which to predict metal-ligand (ML) behaviour in biological systems. For example, speciation diagrams (akin to those presented in Section 2.3.2 for La(dpp)₃ and La(XT)) represent relative distribution of the species present across a range of pH values, and formation constants (K_{ML}) provide a measure of strength of the ML interaction. Furthermore, pM values can be calculated (which take into account ligand basicity) to give a measure of a ligand's ability to bind a metal ion under a specific set of conditions of interest (i.e. pH 7.4, $I = 0.16$ M). This value is calculated from the negative log of the free metal which remains uncomplexed ($pM = -\log [M^{n+}_{free}]$) in the presence of a ligand in 10-fold excess, and is considered of greater biological relevance than the formation constant equilibria.¹¹⁰

In these studies, which were carried out under the direction of Dr. Maria de Guadalupe Jaraquemada-Peláez (Ph.D. 2016, University of Cagliari, Italy), the speciation diagrams, formation constants, and pM values for H₂dpa and H₄pedpa with La³⁺, were determined. The aim was to establish: 1) the contribution to La-complex stability offered by the inclusion of the phosphonate moiety in H₄pedpa; and 2) a comparison between these systems and La(XT), for which an array

of thermodynamic data exists in the literature and has been shown to exhibit good *in vivo* stability.⁶⁸

First, the stepwise ($\log K_a$) and cumulative ($\log \beta$) protonation constants of the ligands alone were determined using potentiometric and NMR spectrometric titrations. These were carried out with a ligand concentration $[L] = 1.0 \times 10^{-3} \text{ M}$ at 298 K and $I = 0.16 \text{ M}$ (NaCl). The distribution diagrams of dpa and pedpa (Figure 4.10) were obtained by fitting potentiometric data using the HyperQuad2013¹¹¹ program, and the related protonation constants are presented in Table 4.5. For both species, the first K_a is assigned to the quaternization of the non-aromatic nitrogen, which is followed by the two carboxylate groups for dpa. These values aid in assigning the K_a for the carboxylate groups in pedpa, which are similar, and fall in between the two K_a values of the phosphonate group. Because the most acidic K_a of pedpa falls outside the ideal range for potentiometric titrations (pH 2 – 10), this was determined by observing the change in chemical shift in the $^{31}\text{P}\{^1\text{H}\}$ NMR spectrum at low pH, and overlaid on the same plot (see Appendix).

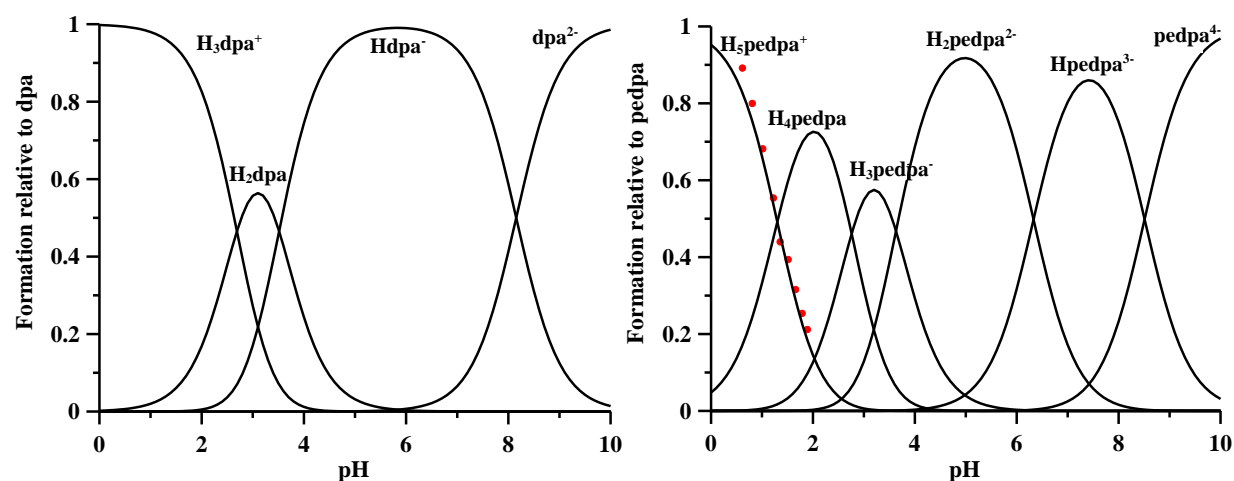


Figure 4.10 Speciation plots for dpa (left) and pedpa (right). Protonation constants are reported in Table 4.5. Relative $^{31}\text{P}\{^1\text{H}\}$ NMR chemical shifts as a function of pH are superimposed on the plot for pedpa (right) (see Appendix).

Table 4.5 Stepwise ($\log K_a$) and cumulative ($\log \beta$) protonation constants for dpa and pedpa determined by potentiometric titrations (298 K, $[L] = 1.0 \times 10^{-3}$ M, $I = 0.16$ M NaCl) performed by Dr. Jaraquemada-Peláez at UBC.



dpa				pedpa		
Species	$\log K_a$	$\log \beta$	Species	$\log K_a$	$\log \beta$	
K_{a1} Hdpa ⁻	8.15	8.15	Hpedpa ³⁻	8.51	8.51	
K_{a2} H ₂ dpa	3.52	11.67	H ₂ pedpa ²⁻	6.33	14.84	
K_{a3} H ₃ dpa ⁺	2.69	14.36	H ₃ pedpa ⁻	3.63	18.47	
K_{a4} -	-	-	H ₄ pedpa	2.76	21.23	
K_{a5} -	-	-	H ₅ pedpa ⁺	1.30 ^a	22.53	

^a Value determined by ³¹P{¹H} NMR titrations.

After obtaining these data, potentiometric titrations with La³⁺ and either ligand were performed. It was found that metal complexation began to occur at very low pH (1-3), and so ¹H NMR titrations within this range were required in order to determine stability constants associated with LaL formation. These were carried out by preparing a D₂O solution of approximately 1:1.5 La:L ratio, and collecting the ¹H NMR spectrum at various pD values, carefully adjusting with dilute DCl and NaOD (Figures 4.11 and 4.12, upper). The ratio of the integrals of the methylene protons associated with either the free ligand or the complexed form were then plotted against pH (pH = pD - 0.4),¹¹² and – using the Hyss and HypNMR2008 programs¹¹³ – the complex formation constants were obtained (Table 4.6). These were found to be in agreement with the models obtained using the HyperQuad2013 program¹¹¹ from potentiometric titrations in 1:1 La:L ratios for both La(dpa) and La(pedpa) (Figure 4.11 and 4.12, lower).

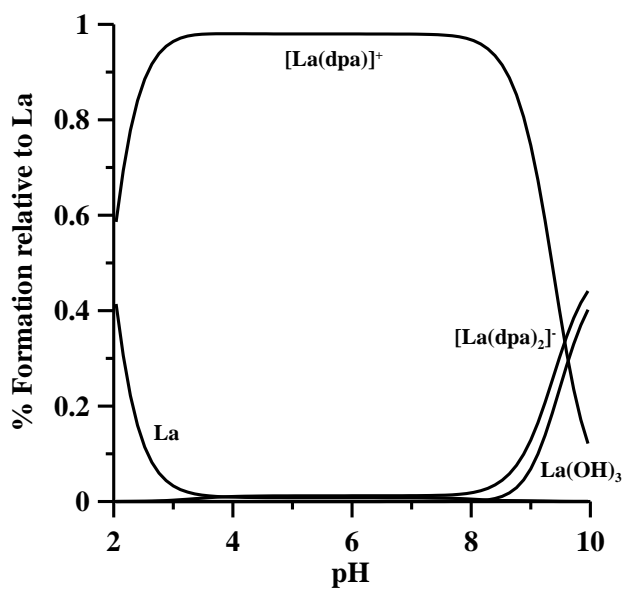
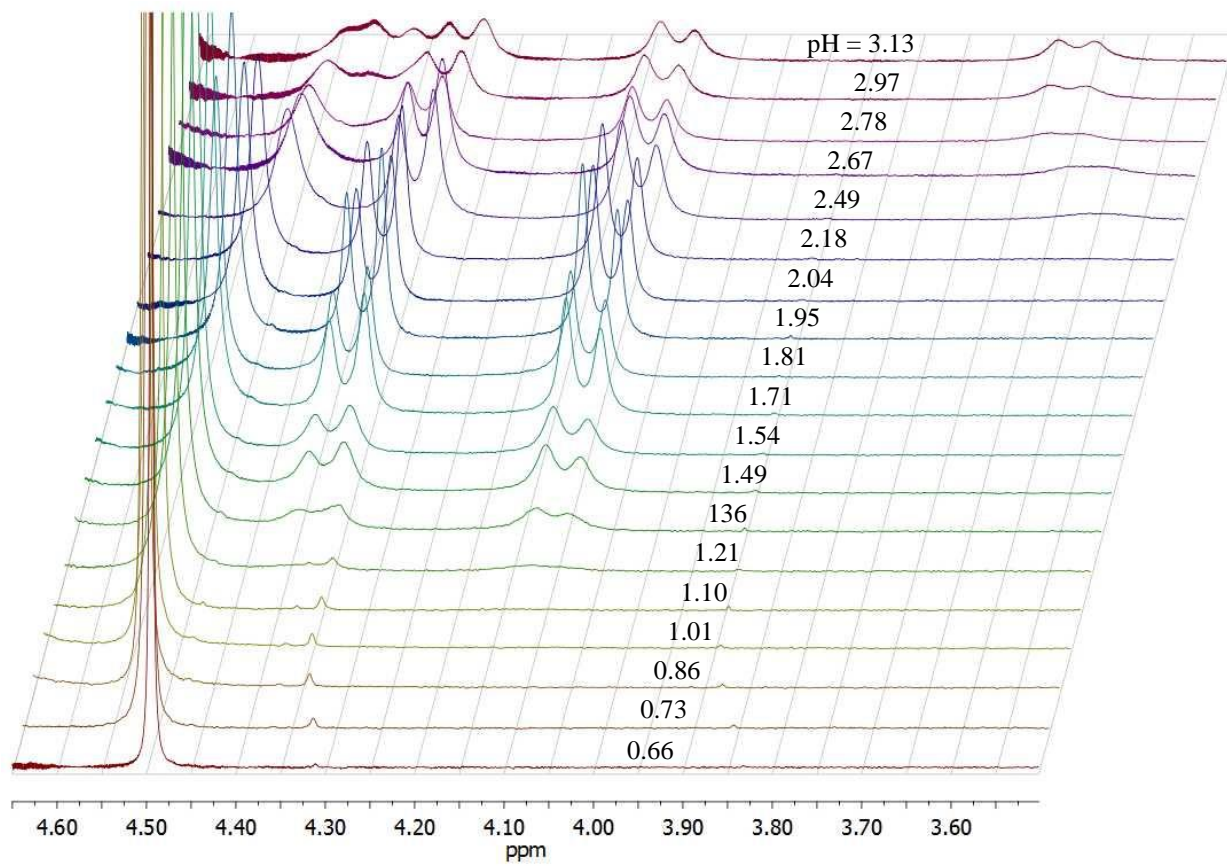


Figure 4.11 Upper: A portion of the ^1H NMR spectra for the La^{3+} -dpa system in D_2O (400 MHz, 298 K, $[\text{La}]:[\text{dpa}] \sim 1:1.6$). Lower: Speciation plot for the same system ($[\text{La}]:[\text{dpa}] = 1:1$, 298 K, $I = 0.16$ M NaCl).

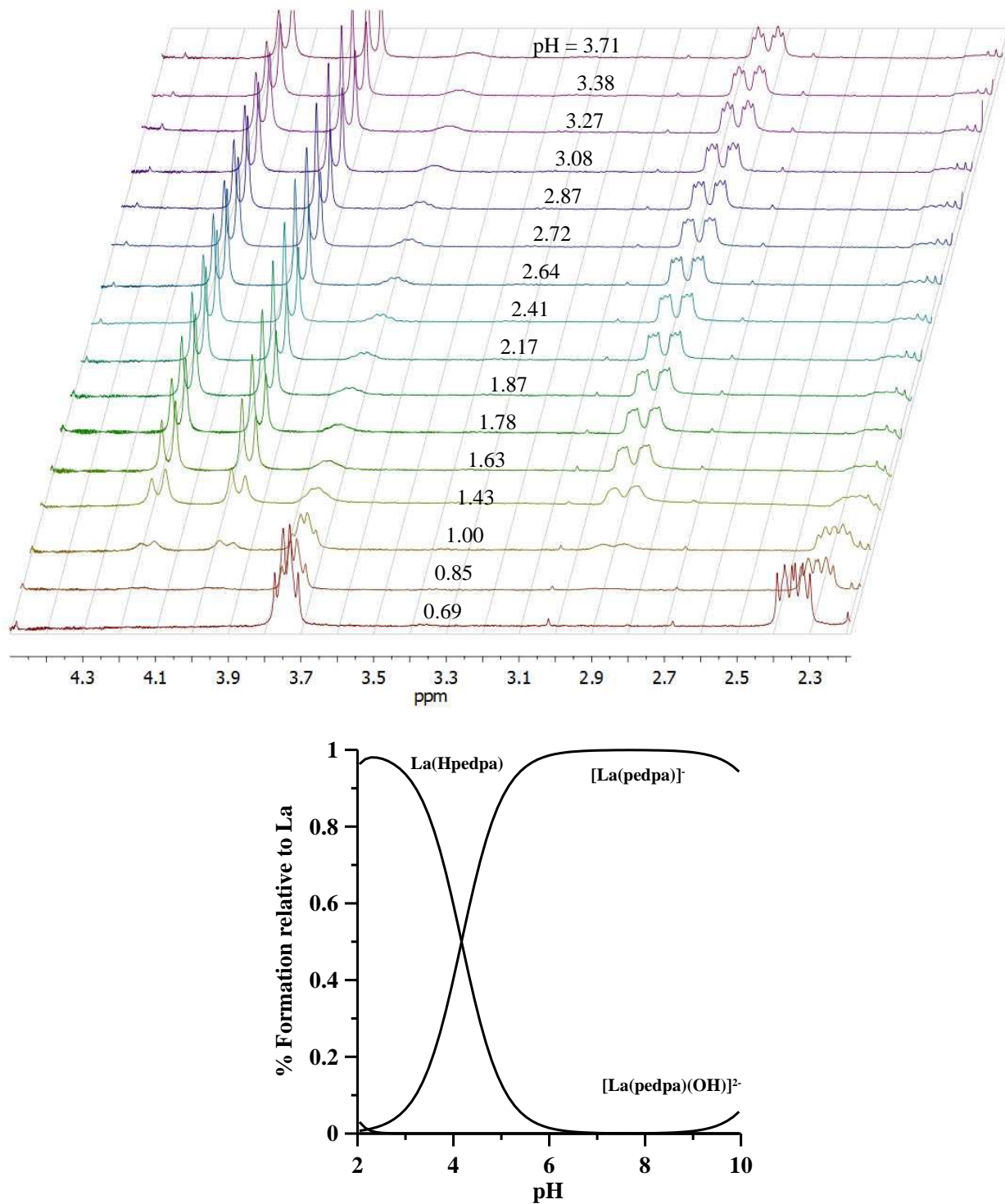
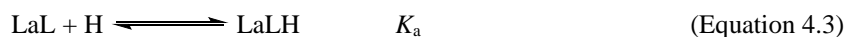


Figure 4.13 Upper: A portion of the ¹H NMR spectra for the La³⁺-pedpa system in D₂O (400 MHz, 298 K, [La]:[pedpa] ~ 1:1.4). Lower: Speciation plot for the same system ([La]:[pedpa] = 1:1, 298 K, *I* = 0.16 M NaCl).

Table 4.6 Comparison of the complex formation constants ($\log K_{\text{LaL}}$ and $\log \beta_{\text{LaHL}}$) and pLa values for lanthanum with dpa, pedpa, and XT (from ref. 68).

Model	dpa	pedpa	XT*
$\log K_{\text{LaL}}$	12.0 ^a	16.6 ^a	13.0(3)
$\log \beta_{\text{LaHL}}$	-	20.8 ^{a,b}	17.14(2)
pLa	14.17 ^c	16.41 ^c	12.1

^a Calculated based on ¹H NMR titrations. ^b Refined based on potentiometric titrations. ^c Calculated from $-\log [\text{La}^{3+}]$ in solution for total $[\text{L}] = 1 \times 10^{-5}$ M, $[\text{La}] = 1 \times 10^{-6}$ M at pH 7.4. *Values obtained from reference 68.



The thermodynamic stability constants in Table 4.6 are reported as K_{LaL} values (Equation 4.2) and cumulative β_{LaHL} values (derived in Equations 4.2 to 4.4). Because LaL complex formation occurs at low pH (<2) for both systems, ¹H NMR titrations were used to calculate these values. For the La^{3+} -dpa system, complex formation (δ 4.40; 4.10 ppm) begins at approximately pH 1.2 (Figure 4.12 upper), with the gradual disappearance of the methylene peak associated with the uncoordinated ligand (δ 4.50 ppm) across a broad pH range leading to a moderate $\log K_{\text{ML}}$ value (12.0). Once the complex is formed, the lack of further protons available for the 1:1 system to lose hinders the use of potentiometric titrations to further refine this value (Figure 4.12 lower); however, the emergence of new signals (δ 4.55; 3.70 ppm) in the 1:1.6 system in the ¹H NMR titrations above approximately pH 2.5 indicates the formation of a new species, presumed to be the 1:2 complex $\text{La}(\text{dpa})_2$. The potentiometric model at very basic pH (>10) fits this hypothesis, and a ¹H NMR spectrum of a 1:2 mixture La:dpa shows sharp signals exclusively at these chemical

shifts (Appendix); however, isolation and full characterization of this complex would be required in order to confirm its existence, and to calculate with confidence the associated LaL_2 formation constants.

For the La^{3+} -pedpa system, strong association and favourable complex formation ($\log K_{\text{LaL}} = 16.6$) is evidenced by the rapid disappearance of the methylene proton signals of the phosphonate-linker arm of the uncoordinated ligand (δ 3.75; 2.35 ppm), and the emergence of the sharp doublet of doublets associated with Py- CH_2 -N of the complex (δ 4.2; 4.0 ppm) as well as linker methylene signals (δ 2.9 ppm) above pH \sim 1.0 (Figure 4.13 upper). It is implicit from these spectra that the phosphonate moiety is involved in lanthanum binding from a low pH, and contributes significantly to the overall stability of the complex. In this case, stability constants could be refined by potentiometry due to the further loss of a proton from the neutral $\text{La}(\text{Hpedpa})$ species ($\text{p}K_{\text{a}}$ 4.17) as well as from a coordinated water molecule ($\text{p}K_{\text{a}}$ 11.2) leading to a hydroxo-complex (Figure 4.13 lower). The former occurrence allows refinement of a cumulative formation constant $\log \beta_{\text{LaHL}}$, enabling a more direct comparison to the stability constants reported for $\text{La}(\text{XT})$.⁶⁸

Overall, from the speciation diagrams in Figures 4.12 and 4.13 (lower), favourable lanthanum complexation occurs across a broad pH range for both dpa and pedpa. Certainly at physiologically relevant pH, the existence of a single 1:1 complex is encouraging, and suggests a high degree of thermodynamic stability in solution. The $\log K_{\text{LaL}}$ values obtained in Table 4.6 reflect this, and imply that pedpa forms a more stable complex with La^{3+} than XT ($\log K_{\text{LaL}} = 13.0$), which is in turn more stable than the dpa complex (following the logic that phosphinate and phosphonate moieties form strong associations with lanthanum). Finally, the pLa values for dpa and pedpa were calculated from $-\log [\text{La}^{3+}_{\text{free}}]$ ($[\text{La}^{3+}_{\text{total}}] = 10^{-6}$ M, $[\text{L}] = 10^{-5}$ M, pH 7.4), and

compared to XT (Table 4.6). Interestingly, in spite of being the less stable complex, the pLa for dpa (14.17) was found to be greater than that for XT (12.1). An explanation for this lies in the possibility for the 2:1 complex to form with dpa, which – in the presence of excess ligand – would deplete the concentration of free La^{3+} leading to a greater pLa value. Still, the greatest pLa was again found for pedpa (16.41), suggesting that this ligand possesses the most effective metal binding ability, as well as the being the most thermodynamically stable complex.

4.2.5 Lipophilicity measurements of dpa compounds and their lanthanum complexes

One of the most important properties to consider in the screening of potential drugs intended for oral administration is the lipophilicity – a concept introduced briefly in Section 1.5.3 – which gives a measure of a compound's affinity for a lipophilic environment and of the ability of a drug candidate to be absorbed across an intestinal membrane, which in turn can be used to predict oral bioavailability. Lipophilicity is often expressed as the log of the partition coefficient ($\log P_{o/w}$), where $P_{o/w}$ is simply derived from the ratio of distribution of the test compound in a biphasic system (equation 4.5), with the subscript denoting the identity of two immiscible solvents (in this case 1-octanol and water). Herein, we present the experimentally-determined (shake-flask method)¹¹⁴ $\log P_{o/w}$ values for the four dpa-based compounds (H_2dpa , H_3cedpa , H_4pedpa , and H_7alenpa), and the 1:1 lanthanum complexes of all but the last ligand, which remained elusive (Table 4.7). Because of the ionizability of the compounds, the water phase was buffered to pH 7.4 (50 mM HEPES) in an effort to imitate physiological conditions. Included for comparison is the $\log P_{o/w}$ value for alendronate,¹¹⁵ an oral treatment prescribed to osteoporosis patients which is approved despite suffering from extremely poor intestinal uptake (see Section 1.4.3).

$$\log P_{o/w} = \log ([\text{compound}]_{1\text{-octanol}} / [\text{compound}]_{\text{water}}) \quad (\text{Equation 4.5})$$

All four of the ligands that were tested exhibited $\log P_{o/w}$ values indicative of hydrophilic character (between approximately -2 and -3) – which is unsurprising given the inclusion of carboxylate and phosphonate groups – with the unfunctionalized H₂dpa exhibiting the least negative $\log P_{o/w}$ value of the free ligands. Nonetheless, all of these compounds show an increase in lipophilic character relative to alendronate, suggesting that they should all exhibit greater intestinal uptake compared to the approved drug. Moreover, directly comparing the partition coefficients for alendronate and H₇alenpa (which is synthesized in one step from alendronic acid) shows that replacing the highly polar primary amine with picolinate moieties increases the partition coefficient by over 2 orders of magnitude.

Table 4.7 Experimentally determined $\log P_{o/w}$ values.^a

Compound	N-R=	$\log P_{o/w}$ (Ligands)	$\log P_{o/w}$ (La ³⁺ complexes)
H ₂ dpa	N ^{-H}	-2.19 ± 0.16	-1.97 ± 0.11
H ₃ cedpa	N-CH ₂ -COOH	-3.01 ± 0.21	-2.01 ± 0.01
H ₄ pedpa	N-CH ₂ -CH ₂ -PO(OH) ₂	-2.38 ± 0.21	-1.32 ± 0.12
H ₇ alenpa	N-CH ₂ -CH ₂ -CH ₂ -C(OH)(PO(OH) ₂) ₂	-2.44 ± 0.11	No data
Alendronate [†]	N/A	-4.49	N/A

^a Shake-flask method; $\log P_{o/w} = \log ([]_{\text{n-octanol}} / []_{\text{HEPES}})$; pH 7.4; n = 3; concentrations by UV-Vis absorbance.

† Experimental value obtained from ref. 115.

Of greater significance are the $\log P_{o/w}$ values for the lanthanum complexes, which all show an expected increase in lipophilic character as the polar hydroxyl groups of the ligands are tied up upon metal chelation. Encouragingly, the greatest change in partition coefficient due to La^{3+} complexation (and the least negative $\log P_{o/w}$ value obtained in this set of experiments) was observed for $\text{La}(\text{pedpa})$, indicating that this compound (which in previous experiments demonstrated good thermodynamic stability and bone targeting ability) is likely to exhibit the greatest enhancement in oral bioavailability compared to alendronate.

It is worth noting that, although an increase in lipophilicity was demonstrated for all compounds tested relative to alendronate, none of the partition coefficients fell within the range that is considered ideal for optimum oral uptake ($-0.5 < \log P_{o/w} < 5$, according to Lipinski's guidelines);⁶⁴ however, as was highlighted in Section 1.5.3, an ideal system for exploring the potential use of lanthanum as an osteoporosis treatment need only exhibit partial GI uptake, and in this regard, $\log P_{o/w}$ values just outside of the stated range may prove to be sufficient.

4.3 Conclusions

Four compounds based on a *N,N*-dipicolinic acid (dpa) scaffold were successfully synthesized and characterized. The synthetic strategy for obtaining these compounds centered around a double alkylation of a primary amine synthon containing the desired functional group. Functionality included carboxylate (H_3cedpa), phosphonate (H_4pedpa), and bisphosphonate (H_7alenpa) moieties, as well as the unfunctionalized equivalent (H_2dpa). Solution depletion studies with these compounds and HAP showed that only the phosphonate- and bisphosphonate-containing compounds (H_2pedpa and H_7alenpa , respectively) demonstrated an attractive interaction with bone

mineral, with the latter exhibiting fast and measurable binding kinetics under the conditions of the experiment.

The lanthanum complexes of all but H₇alenpa were also synthesised, producing stable 1:1 metal-ligand complexes shown by ¹H NMR spectroscopy to be present as single static isomers in solution. Crystals of the 1:1 complex of La(III) with H₄pedpa suitable for solid-state X-ray analysis were obtained, which showed the material as a bridged lanthanum tetramer with two water molecules included in the lattice (La₄(pedpa)₄(H₂O)₂). Speciation diagrams and formation constants for H₂dpa and H₄pedpa with lanthanum were acquired by potentiometric titrations and compared to literature values for H₅XT, which showed that the inclusion of a phosphonate moiety in the ligand scaffold (H₄pedpa) improved lanthanum complex stability – as well as metal scavenging ability (pLa) – relative to both the non-phosphonate containing ligand (H₂dpa) and the current lead compound from previous studies (H₅XT). Finally, lipophilicity measurements in the form of partition coefficients (log *P*_{o/w}) of the four free ligands and three lanthanum complexes were experimentally determined using the shake-flask method, which showed that La(pedpa) was likely to exhibit the greatest intestinal absorption of all the compounds tested.

4.4 Experimental

4.4.1 Materials and reagents

Solvents used in all experiments were of ACS grade or higher and obtained from Sigma-Aldrich or Fisher Scientific. HPLC grade solvents were used in all purification steps. Water used in all synthetic procedures was deionized (DI, 15 MΩ-cm) and obtained from an Elga Purelab Option water purifier. Deuterated solvents for NMR spectroscopy were purchased from Cambridge Isotope Laboratories. Concentrated hydrochloric acid (37%) and ammonium hydroxide (30%)

solutions and solid sodium hydroxide, potassium hydroxide, ammonium chloride, and potassium carbonate were purchased from Fisher Scientific or Sigma-Aldrich. Starting materials **1** (dimethyl pyridine-2,6-dicarboxylate), **4** (2-nitrobenzenesulfonamide), **7** (glycine ethyl ester hydrochloride), **9** (diethyl vinylphosphonate), and **12** (alendronic acid) were obtained from commercial sources and used without further purification, as were the reagents sodium borohydride, phosphorous tribromide, and thiophenol. Lanthanum nitrate hexahydrate was purchased from Alfa Aesar. Analytical thin-layer chromatography (TLC) plates used were aluminum-backed ultrapure silica gel 60 Å of 250 µm thickness (Merck, Germany).

Water used in all analytical experiments was of high purity (MQ, 18.2 MΩ-cm) and obtained from an Elga Purelab Ultra water purifier. Buffered solutions of pH 7.4 and $I = 0.16$ M were prepared from solid 4-(2-hydroxyethyl)-1-piperazineethanesulfonic acid (HEPES) (Fisher Scientific) and trace metal grade sodium chloride (Sigma-Aldrich) at desired concentrations and temperatures using an online buffer recipe calculator (©Rob Beynon, University of Liverpool).¹¹⁶ Synthetic hydroxyapatite was purchased from Sigma-Aldrich and was analyzed in the manner outlined in Section 2.4.2. Sodium deuterioxide (30% wt. in D₂O) and deuterium chloride (35% wt. in D₂O) for NMR titrations were purchased from Sigma-Aldrich as was 1-octanol for log $P_{o/w}$ experiments. Lanthanum ion solutions for potentiometric titrations were prepared from the atomic absorption (AA) standard solution (Sigma-Aldrich, 1021 µg/mL La in 1% wt. HNO₃).

4.4.2 Instruments

All column chromatography was performed using an automated CombiFlash Rf machine (Teledyne ISCO) with pre-packed solid-phase cartridges. Low resolution mass spectra, high resolution mass spectra, and elemental analyses were carried out in the manner outlined in Section

2.4.1.2. NMR spectroscopy was carried out at room temperature using either a Bruker AV-300 or a Bruker AV-400 III HD spectrometer and processed using MestReNova. $^{31}\text{P}\{^1\text{H}\}$ NMR spectra were referenced externally to H_3PO_4 . The X-ray crystal structure of $\text{La}_4(\text{pedpa})_4(\text{H}_2\text{O})_2$ was solved by Dr. Brian Patrick using a Bruker APEX DUO diffractometer and Bruker SAINT software. Ultraviolet-visible (UV-Vis) spectra were collected on a Varian Vary 100 Bio UV-Vis spectrometer. Potentiometric titrations were performed by Dr. Maria de Guadalupe Jaraquemada Peláez using a Metrohm Titrand 809 equipped with a Ross combination pH electrode and a Metrohm Dosino 800 automatic burette. Data were collected using PC Control (Version 6.0.91, Metrohm). Temperature control was maintained using a Julabo water bath (25.0 ± 0.1 °C). The potentiometric titration data were treated by the programs Glee¹¹⁷ and HyperQuad2013.¹¹¹

4.4.3 Synthesis of the dpa-containing compounds

4.4.3.1 Methyl 6-(bromomethyl) picolinate (3) (Scheme 4.1)

Methyl 6-(hydroxymethyl)picolinate (2): Dimethyl-2,6-pyridine dicarboxylate (**1**) (25.2 g, 126 mmol) was taken up in a 7:3 DCM/MeOH mixture (750 mL) and NaBH_4 (5.68 g, 155 mmol) was gradually added over the course of 30 minutes at 0 °C. The reaction mixture was allowed to warm to room temperature and a clear pink colour evolved over the course of 2.5 h. After this time the reaction was quenched with NH_4Cl solution (50% w/w, 250 mL), and the organic portion of the biphasic mixture was collected. The aqueous phase was washed several times with DCM (6 x 100 mL) and the organic fractions were combined and evaporated to give a white solid **2**, which was purified by recrystallization from a minimum volume of EtOAc (17.0 g, 102 mmol, 79%). LC-MS positive ion mode (m/z): 168.3 $[\text{M} + \text{H}]^+$, 190.3 $[\text{M} + \text{Na}]^+$. ^1H NMR (CDCl_3 , 300 MHz, RT): δ

8.05 (d, 1H); 7.86 (t, 1H); 7.54 (d, 1H); 4.87 (d, 2H); 4.01 (s, 3H), 3.37 (s, 1H). ^{13}C NMR (CDCl_3 , 75 MHz, RT): δ 165.4; 160.6; 146.7; 137.6; 123.9; 123.5; 64.6; 52.7.

Methyl 6-(bromomethyl) picolinate (3): **2** (16.4 g, 98 mmol) was taken up in CHCl_3 (300 mL), cooled to 0 °C and stirred. Liquid PBr_3 (10.2 mL, 107 mmol) was added dropwise which caused the evolution of a bright yellow colour. The reaction mixture was allowed to warm to room temperature, and was re-cooled to 0 °C prior to quenching with a saturated K_2CO_3 solution (150 mL). Water (200 mL) was added followed by extraction of the organic product with DCM (6 x 100 mL). The combined organic fractions were dried (MgSO_4), filtered, and evaporated, and the crude products were purified by column chromatography (silica gel 220 g, 20-60% EtOAc in hexane) to give **3** as a white crystalline solid (22.1 g, 96 mmol, 98%). LC-MS positive ion mode (m/z): 230.2, 232.2 $[\text{M} + \text{H}]^+$. ^1H NMR (CDCl_3 , 300 MHz, RT): δ 8.09 (d, 1H); 7.89 (t, 1H); 7.71 (d, 1H); 4.67 (d, 2H); 4.04 (s, 3H). ^{13}C NMR (CDCl_3 , 75 MHz, RT): δ 165.4; 160.6; 146.7; 137.6; 123.9; 123.5; 64.6; 52.7.

4.4.3.2 6,6'-[Azanediylbis(methylene)] dipicolinic acid (H_2dpa) (Scheme 4.2)

Dimethyl 6,6'-[(2-nitrobenzenesulfonyl)azanediyl]bis(methylene) dipicolinate (5): To a stirred solution of 2-nitrobenzenesulfonamide (**4**) (6.37 g, 31.5 mmol) in CH_3CN (150 mL) containing K_2CO_3 (16.0 g) was added **3** (15.5 g, 67.4 mmol), and the reaction mixture was heated to 60 °C. After 24 h, the reaction mixture was quenched with water (100 mL) and washed with DCM (3 x 50 mL). The combined organic extracts were dried (MgSO_4), filtered, and evaporated, and the resulting crude solid was separated from unreacted starting material by column chromatography (silica gel 120 g, 40-100% EtOAc in hexane). The product **5** was obtained as an off-white solid

(11.8 g, 23.5 mmol, 75%). LC-MS positive ion mode (m/z): 523.3 $[M + Na]^+$, 539.3 $[M + K]^+$. 1H NMR ($CDCl_3$, 300 MHz, RT): δ 8.28 (d, 1H); 7.96 (d, 2H); 7.76 (d, 2H); 7.68 (m, 5H); 4.89 (s, 4H); 3.97 (s, 3H). ^{13}C NMR ($CDCl_3$, 100 MHz, RT): δ 165.3; 156.3; 148.1; 147.5; 137.8; 133.6; 133.3; 131.9; 131.3; 125.6; 124.2; 124.1; 53.3; 52.9.

Dimethyl 6,6'-[azanediybis(methylene)] dipicolinate (6): Thiophenol (2.70 mL, 26.3 mmol) was added dropwise to a stirred solution of **5** (12.0 g, 23.9 mmol) in THF (150 mL) containing K_2CO_3 (10.0 g) and heated to 70 °C, causing a bright yellow colour to evolve. After 3 days residual base was removed by centrifugation, and washed three times with THF. The combined supernatants were evaporated, and the resulting crude yellow oil was purified by column chromatography (40 g alumina, 0-5% MeOH in DCM). The product **6** was obtained as an off-white solid (5.29 g, 16.7 mmol, 70%). LC-MS positive ion mode (m/z): 316.4 $[M + H]^+$. 1H NMR ($CDCl_3$, 300 MHz, RT): δ 8.04 (d, 2H); 7.83 (t, 2H); 7.67 (d, 2H); 4.12 (s, 4H); 4.01 (s, 6H); 2.68 (br s, NH). ^{13}C NMR ($CDCl_3$, 100 MHz, RT): δ 165.6; 158.3; 147.6; 137.8; 126.1; 124.0; 53.8; 52.9.

6,6'-[Azanediybis(methylene)] dipicolinic acid hydrochloride (H₂dpa·HCl): **6** (1.0 g, 3.2 mmol) was taken up in 6 M HCl (15.0 mL) and stirred and heated to 110 °C for 12 h. The solvent was evaporated, and the crude residue was dissolved in a minimum volume of water and precipitated by the dropwise addition of acetone. The white solid product was collected by filtration on a fine frit, washed several times with cold acetone, and freeze-dried overnight to give H₂dpa as the HCl salt (0.98 g, 95%). LC-MS positive ion mode (m/z): 288.3 $[M + H]^+$. HR-ESI-MS Calc'd (found) for $C_{14}H_{14}N_3O_4$: 288.0984 (288.0988). 1H NMR (D_2O , 400 MHz, RT): δ 8.11 (d, 2H); 8.05 (t, 2H); 7.68 (d, 2H); 4.62 (s, 4H). ^{13}C NMR (D_2O , 100 MHz, RT): δ 167.9; 150.6; 147.3; 139.7; 127.4;

125.1; 50.69. Anal. Calc'd (found) for C₁₄H₁₅ClN₃O₄: C, 51.94 (51.97); H, 4.36 (4.36); N, 12.98 (12.81). Colourless needles suitable for single-crystal X-ray diffraction analysis were achieved by dissolving H₂dpa.HCl in the minimum volume of a 1:1 water/methanol mixture and cooling to 2°C (Dr. Lisa Murphy, UBC). See Appendix.

4.4.3.3 6,6'-{[(Carboxymethyl)azamediy]bis(methylene)} dipicolinic acid (H₃cedpa) (Scheme 4.3)

Dimethyl 6,6'-{[(ethylethanoate)azamediy]bis(methylene)} dipicolinate (8): To a stirred suspension of glycine ethyl ester hydrochloride (**7**) (1.06 g, 7.6 mmol) in CH₃CN (10 mL) containing K₂CO₃ (4.0 g) was added **3** (3.67 g, 15.9 mmol), and the reaction mixture was heated to 60 °C. After 12 h, the reaction mixture was quenched with water (50 mL) and washed with DCM (3 x 50 mL). The combined organic extracts were dried (MgSO₄), filtered, and evaporated, and the resulting crude solid was separated from unreacted starting material by column chromatography (silica gel 40 g, 0-10% MeOH in DCM). The product **8** was obtained as a white solid (2.56 g, 6.4 mmol, 84%). LC-MS positive ion mode (*m/z*): 440.3 [M + K]⁺. ¹H NMR (CDCl₃, 300 MHz, RT): δ 8.03 (d, 2H); 7.87 (m, 4H); 4.19 (q, 2H); 4.11 (s, 4H); 4.02 (s, 6H); 3.49 (s, 2H); 1.28 (t, 3H). ¹³C NMR (CDCl₃, 100 MHz, RT): δ 173.1; 165.4; 155.7; 148.2; 138.1; 125.4; 123.9; 63.0; 61.2; 55.4; 52.3; 12.4.

6,6'-{[(Carboxymethyl)azamediy]bis(methylene)} dipicolinic acid hydrochloride (H₃cedpa·HCl): **8** (510 mg, 1.3 mmol) was dissolved in 6 M HCl (13.0 mL) and stirred and heated to 110 °C for 12 h. The solvent was removed to give a pale yellow residue, from which the product was precipitated with acetone and collected on a fine frit. The white solid product was washed

several times with cold acetone and freeze dried overnight to give H₃cedpa as the HCl salt (440 mg, 1.2 mmol, 91%). LC-MS positive ion mode (*m/z*): 346.2 [M + H]⁺. HR-ESI-MS Calc'd (found) for C₁₆H₁₅N₃O₆: 345.0961 (345.0963). ¹H NMR (D₂O, 400 MHz, RT): δ 8.09 (m, 4H); 7.77 (d, 2H); 4.71 (s, 4H); 4.20 (s, 2H). ¹³C NMR (D₂O, 75 MHz, RT): δ 171.0; 166.0; 151.2; 146.2; 141.9; 128.4; 125.3; 58.5; 56.6. Anal. Calc'd (found) for C₁₆H₁₆ClN₃O₆: C, 50.34 (50.41); H, 4.22 (4.35); N, 11.01 (10.70). Colourless prismatic single crystals suitable for X-ray diffraction analysis were obtained from the gradual precipitation of H₃cedpa.HCl from a concentrated methanolic solution at room temperature (Dr. Caterina Ramogida, UBC). See Appendix.

4.4.3.4 6,6'-{[(2-Phosphonoethyl)azanediyl]bis(methylene)} dipicolinic acid (H₄pedpa) (Scheme 4.4)

Dimethyl 6,6'-{[(diethyl ethylphosphonate)azanediyl]bis(methylene)} dipicolinate (11): Diethyl vinylphosphonate (**9**) (2.34 g, 14.3 mmol) was dissolved in water (120 mL) and added dropwise over the course of several hours to a cooled (0 °C) ammonium hydroxide solution (120 mL, 30% w/w) with vigorous stirring. After allowing the reaction mixture to warm to room temperature overnight, residual ammonia and water were removed under high vacuum to give diethyl (2-aminoethyl)phosphonate (**10**) as a clear viscous oil which was used without purification. **10** (1.42 g, 7.8 mmol if assumed pure) was then taken up in CH₃CN (50 mL) with K₂CO₃ (4.0 g) suspended and stirred and heated to 60 °C. **3** (3.80 g, 16.5 mmol) was added, and after 12 h the reaction mixture was quenched with water (50 mL) and extracted into DCM (3 x 50 mL). The combined organic extracts were dried (MgSO₄), filtered, and evaporated, and the residual yellow oil was purified by column chromatography (silica gel 24 g, 100% EtOAc followed by 0-15% MeOH in DCM). The product **11** was obtained as a clear oil (2.0 g, 4.2 mmol, 54%). LC-MS positive ion

mode (m/z): 480.4 $[M + H]^+$. 1H NMR ($CDCl_3$, 300 MHz, RT): δ 8.01 (t, 2H); 7.81 (m, 4H); 4.04 (m, 14H); 2.96 (dd, 2H); 2.10 (dt, 2H); 1.25 (t, 6H). $^{31}P\{^1H\}$ NMR ($CDCl_3$, 162 MHz, RT): δ 32.7.

6,6'-{[(2-Phosphonoethyl)azanediyl]bis(methylene)} dipicolinic acid hydrochloride

(H₄pedpa·HCl): Concentrated (12 M) HCl (10.0 mL) was added to **11** (1.0 g, 2.1 mmol) and the reaction mixture was heated to 110 °C and stirred. After 12 h, solvent was removed by evaporation, and residual HCl was co-evaporated several times with small volumes of water. This resulted in a sticky white solid, which was washed several times with cold acetone and then lyophilized overnight to yield the HCl salt of H₄pedpa as an light brown solid (744 mg, 1.7 mmol, 83%).

LC-MS positive ion mode (m/z): 396.3 $[M + H]^+$. HR-ESI-MS Calc'd (found) for C₁₆H₁₉N₃O₇P: 396.0961 (345.0956). 1H NMR (D_2O , 400 MHz, RT): δ 7.99 (d, 2H); 7.94 (t, 2H); 7.59 (d, 2H); 4.78 (s, 4H); 3.97 (dd, 2H); 2.35 (dt, 2H). ^{13}C NMR (D_2O , 100 MHz, RT): δ 167.1; 149.7; 146.5; 139.7; 128.1; 125.2; 58.3; 52.7; 23.5, 22.2 (d). $^{31}P\{^1H\}$ NMR (D_2O , 162 MHz, RT): δ 16.6. Anal. Calc'd (found) for C₁₆H₁₉ClN₃O₇P: C, 44.51 (44.28); H, 4.44 (4.64); N, 9.73 (9.40). Colourless rod-shaped single crystals suitable for X-ray diffraction analysis were obtained from the slow diffusion of acetone into a concentrated aqueous solution of H₄pedpa.HCl at room temperature. See Appendix.

4.4.3.5 6,6'-{[(4-Hydroxy-4,4-diphosphonobutyl)azanediyl]bis(methylene)} dipicolinic acid (H₇alenpa) (Scheme 4.5)

6,6'-{[(4-Hydroxy-4,4-diphosphonobutyl)azanediyl]bis (methylene)} dipicolinic acid

hydrochloride (H₇alenpa·HCl): Alendronic acid (**12**) (144 mg, 0.58 mmol) was suspended in water (3 mL), and with stirring the pH was raised to ~12 by the addition of 1 M NaOH, which

caused **12** to dissolve. Compound **3** (400 mg, 1.74 mmol) was taken up in THF (1 mL) and added to the aqueous solution, which caused an immediate drop in pH and the evolution of a faint pink colour. The pH was periodically readjusted to ~12 with 1 M NaOH over the course of the following 72 h, after which time the solvent was removed to give a sticky white solid. The residue was purified by column chromatography (8 g C18 reverse phase, 0-100% MeOH in H₂O containing 0.1% HCl) to give the product H₇alenpa as the HCl salt (103 mg, 0.19 mmol, 32%). LC-MS negative ion mode (*m/z*): 518.1 [M – H]⁻. HR-ESI-MS Calc'd (found) for C₁₈H₂₄N₃O₁₁P₂: 520.0886 (520.0879). ¹H NMR (D₂O, 400 MHz, RT): δ 7.71 (m, 4H); 7.41 (d, 2H); 3.90 (s, 4H); 2.70 (t, 2H); 2.00 (br, 2H); 1.90 (br, 2H). ¹³C NMR (D₂O, 75 MHz, RT): δ 173.0; 157.8; 152.5; 137.8; 126.0; 122.0; 78.1, 76.3, 74.5 (t); 60.0; 57.1; 33.7; 21.2. ³¹P{¹H} NMR (D₂O, 121 MHz, RT): δ 19.6. Anal. Calc'd (found) for C₁₈H₂₄ClN₃O₁₁P₂: C, 38.90 (39.00); H, 4.35 (4.63); N, 7.56 (7.56).

4.4.4 Solution depletion studies

All time points were performed in triplicate. Samples containing 10.0 mg of HAP were incubated and agitated (37 °C, 220 rpm) with 0.9 mL HEPES (50 mM, pH 7.4 at 37 °C, *I* = 0.16 M NaCl) in 1.5 mL Eppendorf tubes for 24 h. Stock solutions (1 mM) of each of the four dpa-containing compounds were prepared in buffer from their HCl salts. At the outset of the experiment, 100 μL of either H₂dpa, H₃cedpa, H₄pedpa, or H₇alenpa solution was added to the HAP suspension and incubated and agitated for a set period of time. When the desired time point was reached, the sample tubes were centrifuged for 1 minute, and the supernatant carefully extracted by syringe and filtered through a 22 μm frit. An aliquot (0.3 mL) of the supernatant was taken and diluted to 3.0 mL with HEPES buffer and analyzed by UV-Vis spectrometry. Compound concentrations were

determined using the Beer-Lambert relationship. See Appendix for molar extinction coefficients (ϵ) and absorbance maxima (λ_{max}).

4.4.5 General synthesis of La(III)-dpa complexes (Scheme 4.6)

H₂dpa·HCl, H₃cedpa·HCl, or H₄pedpa·HCl (100 mmol) and La(NO₃)₃·6H₂O (43 mg, 100 mmol) were dissolved in water (2.0 mL) and 1 M KOH was added very gradually at room temperature until a pH of between 8 and 10 was reached. The solvent was partially removed under vacuum, and the products were precipitated by the addition of a few drops of MeOH followed by acetone (3-4 mL), collected by filtration, and washed several times with cold acetone. Drying overnight by lyophilisation gave the lanthanum complexes as white or off-white solids.

La(dpa)·xH₂O: LC-MS positive ion mode (m/z): 424.1 [M + H]⁺. HR-ESI-MS Calc'd (found) for C₁₄H₁₁¹³⁹LaN₃O₄: 423.9813 (423.9815). ¹H NMR (D₂O, 400 MHz, RT): δ 8.00 (t, 2H); 7.91 (d, 2H); 7.58 (d, 2H); 4.39 (d, 2H); 4.13 (d, 2H). ¹³C NMR (D₂O, 75 MHz, RT): δ 173.0; 158.0; 150.9; 140.6; 125.4; 123.6; 53.8.

La(cedpa)·xH₂O: LC-MS positive ion mode (m/z): 481.1 [M + H]⁺; 520.0 [M + K]⁺. HR-ESI-MS Calc'd (found) for C₁₆H₁₃¹³⁹LaN₃O₆: 481.9868 (481.9866). ¹H NMR (D₂O, 400 MHz, RT): δ 7.93 (t, 2H); 7.82 (d, 2H); 7.50 (d, 2H); 4.18 (d, 2H); 4.03 (d, 2H); 3.51 (s, 2H). ¹³C NMR (D₂O, 75 MHz, RT): δ 179.4; 172.6; 156.7; 151.2; 140.9; 125.9; 123.8; 62.1; 61.6.

K[La(pedpa)]·xH₂O: LC-MS positive ion mode (m/z): 570.0 [M + H]⁺; negative ion mode (m/z): 530.0 [M - K]⁻. HR-ESI-MS Calc'd (found) for C₁₆H₁₄¹³⁹LaN₃O₇P: 529.9633 (529.9630). ¹H NMR

(D₂O, 300 MHz, RT): δ 8.06 (m, 4H); 7.64 (d, 2H); 4.18 (d, 2H); 3.90 (d, 2H); 2.82 (dt, 2H); 1.83 (dt, 2H). ¹³C NMR (D₂O, 75 MHz, RT): δ 173.0; 157.1; 151.6; 140.8; 126.6; 123.8; 59.9; 53.3; 24.9. 23.2 (d). ³¹P{¹H} NMR (D₂O, 162 MHz, RT): δ 20.7.

4.4.6 Solution thermodynamics

Potentiometry: All data were collected in triplicate. The titration apparatus consisted of a 10 mL water-jacketed glass vessel maintained at 298 K. Nitrogen gas, purified through a 10% NaOH solution to exclude any CO₂, was passed through the solution prior to and during the titrations. The ionic strength was maintained at 0.16 M using NaCl. Prior to each titration, the electrode was calibrated using a standard HCl solution. Calibration data were analyzed by standard computer calculations to obtain calibration parameters E_0 and pK_w . Equilibrium times for titrations were 10 minutes for pK_a titrations and 15 minutes for metal complex titrations. Carbonate-free solutions of the titrant (NaOH aq.) were prepared by dilution of 0.1 moles of NaOH (analytical standard) with freshly boiled MQ water (800 mL) under a stream of nitrogen. The solution was standardized against freshly recrystallized potassium hydrogen phthalate. Lanthanum ion solutions were prepared by dilution of the atomic absorption (AA) standard. The exact amount of acid present in the La standard was determined by titration of an equimolar solution of La(III) and Na₂H₂EDTA using a Gran plot.¹¹⁸ Ligand and metal concentrations were in the range of 0.8 to 1.0 mM for potentiometric titrations. Determination of the acid dissociation constants was achieved by the titration of 1.0 mM ligand solutions with CO₂-free NaOH at 25 °C and 0.16 M NaCl.

NMR: The first pK_a from the phosphonate group of pedpa was determined by ³¹P{¹H} NMR titrations. 10 mM solutions of the ligand in D₂O were prepared at different pH levels, adjusting

with dilute NaOD or DCl. The pD values were measured *via* electrode (Mettler Toldedo) and converted to pH using the deuterium isotopic relation $\text{pH} = \text{pD} - 0.4$.¹¹² The pK_a was calculated using the HypNMR2008 and Hyss programs.¹¹³ Complex formation constants of La(dpa) and La(pedpa) were determined by ^1H NMR titrations. Spectra were collected of La-ligand solutions in approximately 1:1.5 ratio in D_2O at 298 K at various pD levels, measured *via* electrode immediately prior to collecting the spectra and converted to pH.¹¹² The data were processed and complex formation constants calculated using the HypNMR2008 and Hyss programs.¹¹³

4.4.7 Determination of octanol-water partition coefficients

The shake-flask method¹¹¹ was used to experimentally determine the $\log P_{o/w}$ values for four ligands (H_2dpa , H_3cepda , H_4pedpa , and H_7alenpa) and three lanthanum complexes (La(dpa), La(cedpa), and La(pedpa)). All measurements were run in triplicate. The aqueous (50 mM HEPES, pH 7.4 at 25 °C, $I = 0.16$ M) and 1-octanol solvents were pre-saturated with one another prior to use. In a 1.5 mL Eppendorf tube was added 1-octanol (0.750 mL) and 1.0 mM either ligand or metal complex aqueous solution (0.750 mL). Samples were vortexed manually (1.0 minute), inverted on an auto-mixer (5.0 minutes), and centrifuged (1.0 minute, 6000 rpm). The upper and lower layers were carefully separated, and an aliquot (0.500 mL) of either the 1-octanol or HEPES layer was diluted to 5.0 mL with ethanol or aqueous buffer, respectively. Each layer was analyzed by UV-Vis spectrometry, applying the Beer-Lambert law to determine either ligand or metal-ligand complex concentration (ϵ and λ_{max} values in Appendix).

Chapter 5: Conclusions, ongoing studies, and future directions

5.1 Conclusions

An array of chelating ligands – which have been designed to form stable complexes with trivalent lanthanum – are at various stages of testing to assess their ability to enhance the oral uptake of La(III), and complement the metal ion's intrinsic *in vivo* bone targeting properties. Two of these complexes, La(dpp)₃ and La(XT), emerged as lead compounds from previous work within our group, and in Chapter 2 a thorough investigation into the thermodynamic and kinetic interactions between the two complexes and hydroxyapatite (HAP – an established model for bone mineral), was conducted. It was found by ITC and solution depletion studies that, under simulated physiological conditions, the bidentate 3-hydroxy-4-pyridinone system (Hdpp) did not noticeably interfere with lanthanum's natural tendency to bind to HAP; however, this system's lack of thermodynamic stability suggested that the complex was unlikely to maintain its intended *tris-metal* configuration *in vivo*. Conversely, the phosphinate-containing compound H₅XT binds lanthanum tightly at physiological pH and temperature, but a convoluted energetics profile between the ligand, the metal, and bone mineral hindered the extraction of meaningful thermodynamic and kinetic data.

Of greater significance from a biological standpoint are the results presented in Chapter 3, in which the two drug candidates were the subjects of a series of intravenous and oral biodistribution studies in healthy rats. From these results, it was clear that lanthanum was actively incorporated into and retained by bone tissue irrespective of the chelated ligand system. This was evidenced by preferential La(III) uptake in regions of the bone which remodel more rapidly (knee), and by comparable levels of La(III) detected in the femurs of animals which had differing IV dosing regimes. The first distinct and observable differences between the two systems (in terms of

in vivo behaviour) were witnessed in a short-term (4-week) oral study, in which the post-experiment femur lanthanum levels were 3 to 4 times greater for animals that had been dosed with La(XT) *versus* those dosed with La(dpp)₃. This is believed to be a direct consequence of the relative thermodynamic stabilities of two complexes (emphasized in Chapter 2), as well as a possible contribution to bone targeting from the phosphinate moiety in XT. In moving forward from these studies, we can conclude that La(XT) is a more viable candidate than La(dpp)₃ in terms of potential new treatments for osteoporosis, and henceforth will be considered the primary lead compound in future pre-clinical and clinical trials.

In Chapter 4 are outlined the synthesis, characterization, and preliminary testing of four compounds (H₂dpa, H₃cedpa, H₄pedpa, and H₇alenpa) based on a dipicolinic acid (dpa) scaffold, with differing functionalities designed to influence bone targeting and lanthanum binding. The design mantra for this series of compounds was to draw upon favourable characteristics of Hdpp (in terms of tunability) and H₅XT (in terms of increased denticity). The 1:1 lanthanum complexes of three of these chelating ligands (all but H₇alenpa) were successfully isolated and characterized, and from the testing undertaken so far (HAP binding kinetics, lanthanum binding, and lipophilicity measurements) the La(III) complex of the monophosphonate-functionalized H₄pedpa gave the most consistently favourable results. This includes a measurable attractive interaction between the ligand and HAP, high thermodynamic stability of the 1:1 La³⁺ complex under physiological conditions, and a partition coefficient that implies the greatest oral uptake of the complexes tested. There is work still to be done with this series of compounds before a lead compound can be truly verified (including cell permeability and cytotoxicity); however, thus far La(pedpa) appears to be the most likely candidate for progressing into pre-clinical trials.

5.2 Ongoing studies

5.2.1 Expanding the dpa series (part I): Adding lipophilic functionality

The four iterations of the dpa ligand scaffold presented in Chapter 4 were designed to span a range of bone targeting and lanthanum binding ability. The partition coefficients that were measured in Section 4.2.5 were indicative of compounds that were likely to exhibit low *in vivo* absorption, with the highest log $P_{o/w}$ value measured for La(pedpa)⁻ (log $P_{o/w}$ = -1.32 ± 0.12 at pH 7.4 and 37 °C) which – while a significant improvement on currently approved oral drugs for osteoporosis – falls short of what is considered the optimal range for intestinal uptake.⁶⁴ In effort to expand the dpa series to include more lipophilic functionality, the di-(4-methoxy)picolinate (d-MeO-pa) derivatives were targeted (Figure 5.1), taking advantage of the 4-position on the pyridine ring as a derivatization point unlikely to impact lanthanum chelation.

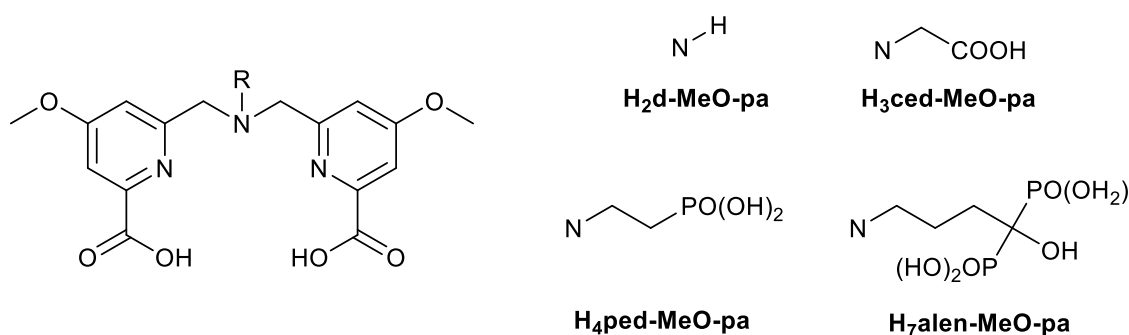
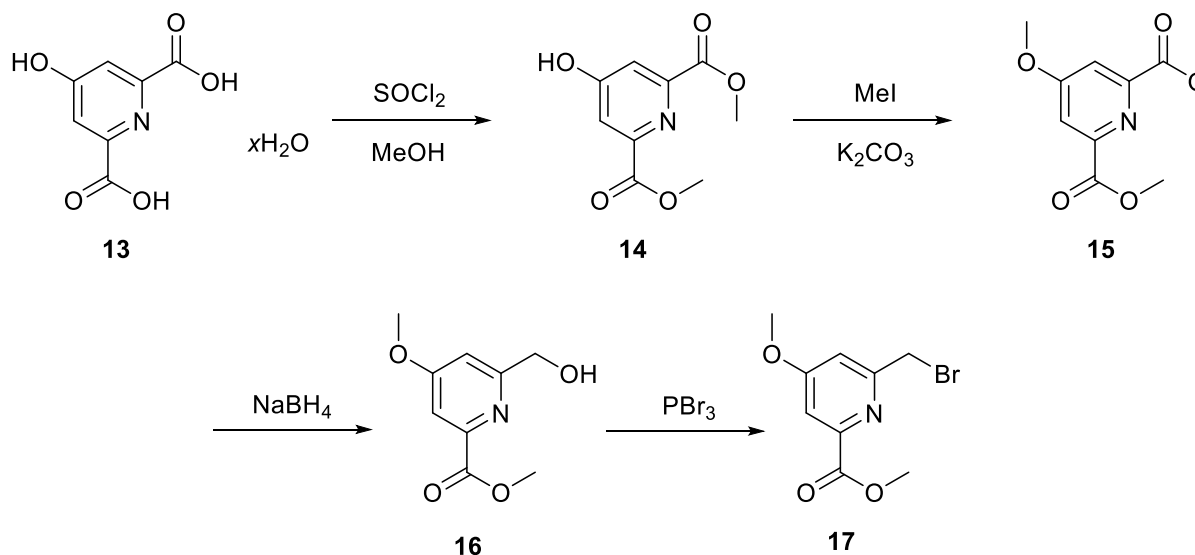


Figure 5.1 A proposed expansion to the dpa scaffold – d-MeO-pa – incorporating lipophilic methoxy moieties.

There are a number of synthetic challenges that must be overcome if this ligand set is to be realized. Firstly, the 4-methoxy analog of the starting material **1** (see Scheme 4.1, Section 4.2.1) is not commercially available. It can be synthesized in over two steps from chelidamic acid hydrate (**13**) – which is readily available (Sigma Aldrich) – followed by a similar mono-reduction and

bromination procedure (Scheme 5.1);⁹² however, this inevitably reduces the cumulative yield of the final ligands. Current work within our group is focussed on optimizing these conditions.

Scheme 5.1 Previously reported synthetic route to the alkylating agent methyl (6-bromomethyl)-4-methoxypicolinate (**17**). Reported cumulative yield: 31%.⁹²



The second major challenge arises in the ester deprotection step, which is the final step required to access the ligands after alkylating the desired primary amine synthon. It was found that, under the strong acidic conditions that were applied to deprotect the dpa ligands (Scheme 4.2 to 4.4, Section 4.2.1), the backbone OMe groups were either partially or fully demethylated. Particularly in the case of the phosphonate group, which is not susceptible to basic deprotection, finding a method which selectively removes the methyl esters without affecting the methoxy groups proved challenging. These ligands remain ongoing synthetic targets for this project.

5.2.2 Spatial mapping of La in bone by laser ablation ICP-MS

In Section 3.5 are presented the first results from K-edge subtraction (KES) imaging of lanthanum in the lower lumbar section of a rat that was treated with La(XT) by IV dose. This technique enabled spatial resolution of the metal ion distributed in bone tissue, which in future experiments could give insight into the mechanism of action of a potential drug. The major limitation of this method is the need for a synchrotron beam source.

A more readily available and less expensive technique that could also allow quantitative elemental mapping with good sensitivity is laser ablation (LA) ICP-MS, which in the past has been used to detect the concentration and location of lanthanides in cross sections of fossilized human bones.¹¹⁹ An advantage of using laser methods *versus* solution ICP-MS is the ability to directly analyze solid samples, negating the need for lengthy digestion procedures, precisely weighed solutions, and scrupulously clean glassware. Mounting fresh bone samples for LA ICP-MS is relatively straightforward, and Figure 5.2 shows an exposed cross-section of a rat femur (not treated with a lanthanum compound) fixed in an epoxy resin puck – manufactured under the guidance of Dr. Richard Friedman (PCIGR, Earth and Ocean Sciences, UBC) – and suitable for LA ICP-MS analysis.

The most important factor in obtaining accurate quantifiable data from LA ICP-MS is the solid calibration standard, which must match the matrix of the analyte material as closely as possible, as well as contain a known concentration of the element one wishes to measure. This is a frequent limitation of LA ICP-MS, and particularly for bone – which can exhibit matrix variations depending on source, age, and state-of-health – a lack of suitable Certified Reference Materials (CRMs) hinders the ability to obtain quantitative results.^{120,121}

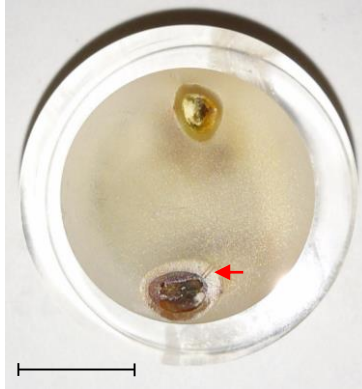


Figure 5.2 An epoxy-mounted rat femur suitable for analysis by LA ICP-MS. The puck was manufactured by cleaning the bones manually of soft flesh, followed by fixing in freshly-made epoxy and allowing hardening for 24 hours. The bone surface was then prepared by sanding, followed by mechanical polishing with progressively finer polishing gels (6 μm , 3 μm , and 1 μm) leaving a shiny exposed flat surface. The red arrow shows the path traced by the laser during LA ICP-MS analysis, and gives an indication of the spatial resolution that could be obtained.

In this regard, an ongoing side-project – currently being undertaken in conjunction with Rhy MacMillan (Ph.D. candidate, Geological Sciences, EOS, University of British Columbia) – is the development of a matrix-matched standard for detecting lanthanum concentration and spatial distribution in samples of fresh mammalian bone. In a first-attempt at this, bone meal pellets spiked with known concentrations of lanthanum were prepared by the pressurized pelletization of powdered bone meal (NIST Standard Reference Material 1486) which had been treated with aqueous solutions of known lanthanum concentrations and thoroughly evaporated. It was found that, although solution ICP-MS confirmed accurate La concentrations within the powdered bone meal, laser ablation of the pellets themselves caused substantial crater sizes inconsistent with those formed on samples of bone. This suggests that pelletization of the bone meal SRM alone is insufficient to generate matrix-matched standards for solid bone samples, and that in future attempts some additive may be required which enables this method to be applied.

5.2.3 Ongoing *in vivo* studies

The experiments presented in Chapter 3 detail the *in vivo* distribution of lanthanum following the IV or oral administration of either La(dpp)₃ or La(XT) in different dosing regimes. The most important result was the difference noted in femur uptake between the two compounds from the 4-week oral study, which showed that La(XT) was the more favourable candidate of the lead compounds; however, it is apparent that a great deal more biological work needs to be done, particularly given the complexity of bone. In progressing from these studies, ongoing work is focussed on establishing the pharmacokinetic parameters (akin to those presented in Chapter 3, Table 3.1) which govern the biodistribution of La(XT) from both oral and IV administrations. These data will facilitate the precise calculation of oral bioavailability as a percentage uptake, and enable the first true comparison between the uptake of lanthanum carbonate, and that of our specifically designed metal-ligand complex. Also included in this study will be an assessment of the fate of the ligand itself, which was not addressed during previous experiments.

Following this, approval has been granted for a 6-month oral study of La(XT) in OVX rats (a model for osteoporosis) and sham-operated rats (control groups). The experiment will consist of 4 treatment groups ($n = 8$): 1 x IV dose group ($1 \text{ mg kg}^{-1} \text{ week}^{-1}$) and 3 x oral dose groups (50 , 100 , and $200 \text{ mg kg}^{-1} \text{ day}^{-1}$) of La(XT) in OVX rats; and 5 control groups: non-treated OVX rats; non-treated sham-operated rats; and 3 x lanthanum carbonated treated OVX rats (50 , 100 , and $200 \text{ mg kg}^{-1} \text{ day}^{-1}$). Oral doses will be administered *via* water supply. Animal body weight will be monitored weekly and blood will be collected at routine intervals during the study. In addition to La³⁺ levels, serum creatinine, phosphorous, and calcium levels will be measure, as well as serum bone turnover markers pyridinoline and osteocalcin. Calcein green (a fluorochromatic bone label) will be twice administered (at 21 days and 7 days) prior to euthanization which will enable

fluorescence microscopy analysis on bone tissue to assess osseous growth and histology. Bone architectural analysis and La^{3+} mapping will be performed by XAS (K-edge subtraction) and micro-CT. The mechanical properties of bone will also be tested. Soft tissues (liver, spleen, kidney, heart, lung brain, and small intestine) and bone (femurs, vertebrae) will be collected and analyzed for lanthanum content by ICP-MS, and – crucially – histological studies will be performed on the kidney, liver, and spleen to assess any toxicological effects of the drug. Excreted materials will also be assessed for lanthanum content to enable mass balance calculations.

All ongoing and future animal studies are being carried out under the direction of Dr. Jacqueline Cawthray (Wasan Research Group, College of Pharmacy and Nutrition, University of Saskatchewan, SK) with compounds synthesized by our group.

5.3 Future studies

5.3.1 Further *in vitro* experiments with La(XT) the dpa compounds

As was alluded to at the end of Section 5.1, the steps required in progressing the dpa series from physical experiments (with non-living tissues) to pre-clinical trials should focus on cell-based studies (i.e. cell viability and cell permeability). Cell viability measurements pertaining to a particular compound are usually given as either half-maximal inhibitory concentration (IC_{50}) values, or half-maximal effective concentration (EC_{50}) values, depending on whether the drug is a repressor or an agonist of cellular activity, respectively. Previously, with the pyridinone complexes and La(XT), only the IC_{50} values with an MG-63 cell-line (which possesses many of the features of osteoblasts)¹²² were determined.^{67,69} The results were reassuring, in that negligible cytotoxicity was observed with any of the compounds tested; however, given the proposed simultaneous suppressive/promotive effect of lanthanum on osteoclasts and osteoblasts,

respectively (see Section 1.5.1),⁵² a more thorough *in vitro* investigation – both with the current lead compound (La(XT)) and with the dpa complexes – is warranted.

Establishing both the IC₅₀ and EC₅₀ values of drug candidates towards osteoblast and osteoclast cell lines would enable assessment of the most effective bone forming concentrations. Furthermore, some studies have called into question the relevance of MG-63 cells in representing the osteoblastic phenotype.¹²³ Protocols have been published which outline the isolation and culture of human osteoblasts and osteoclasts, as well as assessing their biological activity (formation and resorption assays);^{124,125} however, there are significant challenges associated with these techniques that would almost certainly require specialist collaboration. *In vitro* experiments of this type therefore remain a prominent goal for future work on this project.

In addition to cell viability tests, cell uptake studies with the dpa complexes should be performed. These studies will give a measure of the drug's ability to cross an intestinal membrane, and the results are predicted to follow a similar trend to the log $P_{o/w}$ values determined in Chapter 4. The human epithelial cell line Caco-2 is a well established model for drug absorption,¹²⁶ and was used in experiments that established both La(dpp)₃ and La(XT) as early lead compounds (see Section 2.1). Therefore, it is reasonable to propose that the same model should be used to assess the dpa complexes in future studies.

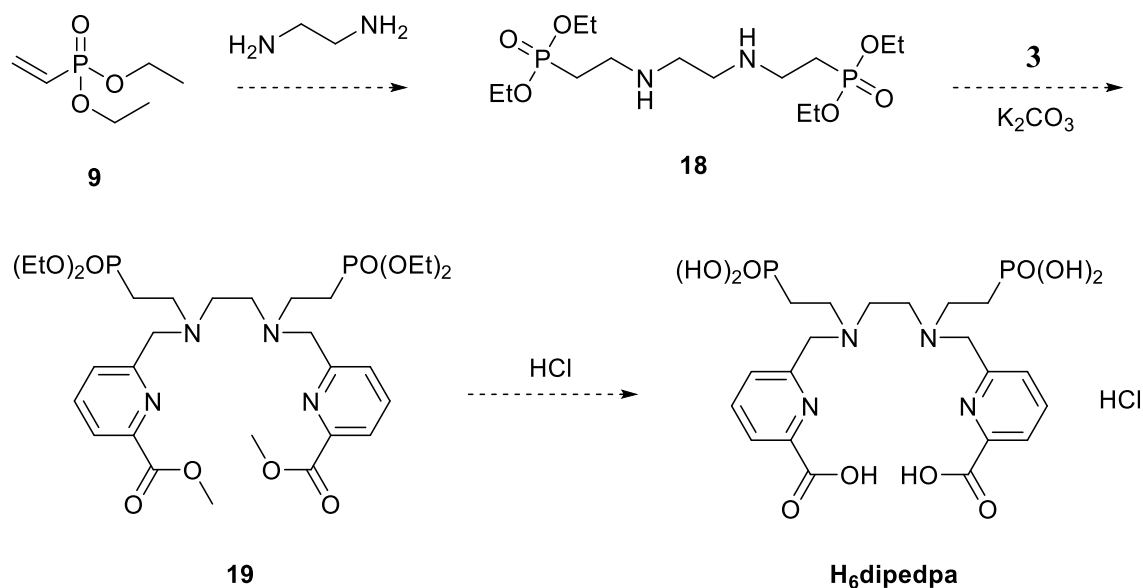
5.3.2 Expanding the dpa series part (II): A larger binding cavity

The most challenging aspect of this project is the lack of a clearly-defined set of parameters which dictate the desired properties of an ideal metal-ligand complex. On the one hand, the system must possess the necessary thermodynamic stability to survive *in vivo* physical conditions and avoid lanthanum transchelation with endogenous binders; on the other, the chelating ligand must not

inhibit the metal's natural tendency to target and bind with bone mineral. A proposed design feature to overcome this point is to incorporate ligand functionality which also targets bone (phosphonate or bisphosphonate moieties); however, this does not correlate well with the other purpose of the ligand, which is to improve the oral uptake of lanthanum. Finally, synthetic accessibility must be taken into consideration, especially when moving towards pre-clinical trials.

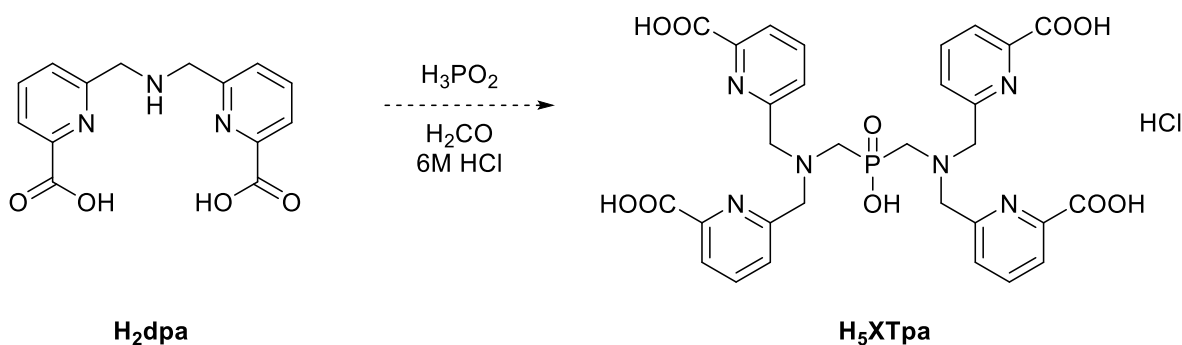
Clearly, there is a vast number of possibilities that could be explored in the quest for the most ideal candidate (which balances all the desired properties), but as was emphasized in the case of $\text{La}(\text{XT})$ versus $\text{La}(\text{dpp})_3$, *in vivo* stability is one of the most crucial considerations. With this in mind, the synthetic routes to two compounds ($\text{H}_6\text{dipedpa}$ and H_5XTdpa) – which invoke greater denticity than the current dpa family – are proposed (Scheme 5.2 and Scheme 5.3).

Scheme 5.2 Proposed synthetic route to $\text{H}_6\text{dipedpa}$.



H₆dipedpa incorporates the H₂dedpa scaffold (Figure 4.2), and is closely related to the ⁸⁹Zr chelating ligand H₆phospa,⁹⁶ but is accessible in fewer steps *via* the proposed route (Scheme 5.2). H₅XTdpa is the expected product of replacing iminodiacetic acid with H₂dpa, which also possesses the necessary secondary amine functionality required to undergo a one-pot Mannich reaction with hypophosphorous acid, and bridge a phosphinate group (Scheme 5.3). If successfully synthesized, these ligands could prove useful not only in La³⁺ chelation, but in the binding of other metals and radiometals of interest.

Scheme 5.3 Proposed synthetic route to H₅XTdpa.



5.3.3 Other potential ligands

In addition to targeting novel compounds, there are number of chelating ligands present throughout the literature which have the potential to deliver lanthanum to bone. Some possibilities are presented in Figure 5.3. These ligands have all been previously reviewed for their binding properties with various metals, and for most part are analogues of established ligands in which carboxylate groups have been replaced by phosphonates, in a direct effort to improve the stability of their Ln(III) complexes.^{127,128} H₈EDTMP was already discussed in Section 1.3.2 as a ligand for

^{153}Sm in treating bone metastases;¹⁹⁻²² H_{10}DTPP is patented for use with ^{111}In as a bone-seeking gamma imaging agent;¹²⁹ and H_8CDTP and H_8DMPDTP include functionality conducive to both lanthanum binding and increased lipophilicity.^{128,130} The synthetic accessibility and stability of the lanthanum complexes would need to be assessed in order to establish their viability for delivering La^{3+} to bone.

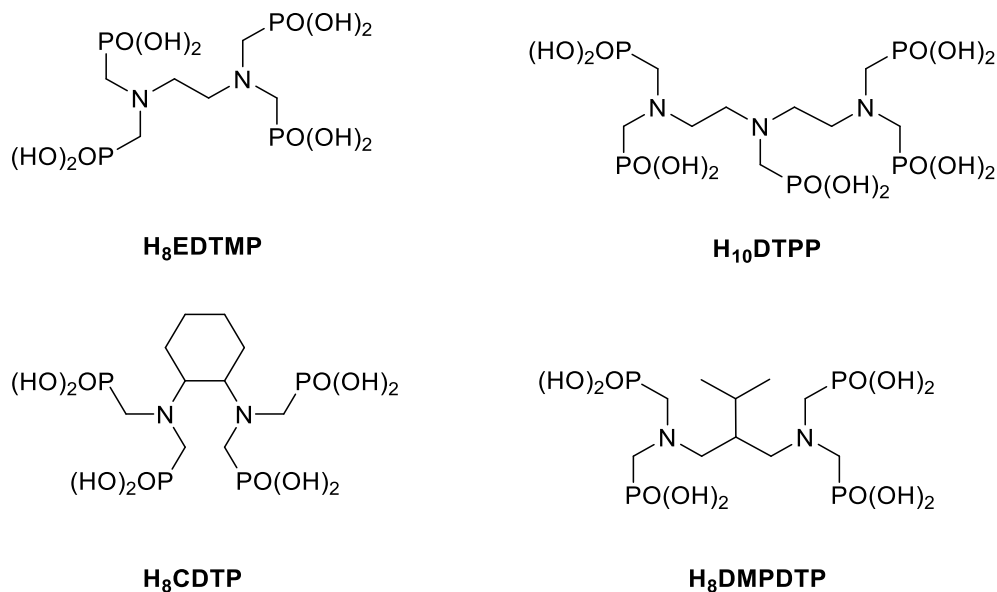


Figure 5.3 Literature examples of possible chelators for La^{3+} ions. H_8EDTMP = ethylenediamine tetrakis(methylene phosphonic acid);²⁰ H_{10}DTPP = diethylenetriamine pentakis(methylene phosphonic acid);¹²⁹ H_8CDTP = 1,6-cyclohexyldiamine tetrakis(methylene phosphonic acid);¹²⁸ H_8DMPDTP = 1,3-diamino-2-isopropylpropane tetrakis(methylene phosphonic acid).¹³⁰

References

1. M. J. Glimcher, in *Metabolic Bone Disease and Clinically Related Disorders*, ed. L. V. Avioli and S. M. Krane, Academic Press, San Diego, 1998, 3rd edn, ch. 2, pp. 26-50.
2. D. J. Hadjidakis and I. I. Androulakis, *Women's Health and Disease: Gynecologic, Endocrine, and Reproductive Issues*, Annals of the New York Academy of Science, 2006, vol. 1092, pp. 385-396.
3. National Osteoporosis Foundation, <http://nof.org/articles/5> (accessed February 16, 2016).
4. M. Vallet and S. H. Ralston, *J. Cell. Biochem.* **2016**, *117*, 289.
5. P. J. Marie, O. Fromigué and D. Modrowski, in *Bone Cancer: Primary Bone Cancers and Metastases*, ed. D. Heymann, Elsevier, Amsterdam, 2015, 2nd edn, ch. 4, pp. 39-54.
6. K. H. Thompson and C. Orvig, *Science* **2003**, *300*, 936.
7. C. Güner, V. Aliyev, D. Atamtürk, I. Duyar and T. Soylemezoglu, *Euras. J. Anthropol.* **2011**, *2*, 27.
8. M. I. Kay, R. A. Young and A. S. Posner, *Nature* **1964**, *204*, 1050; E. D. Eanes and A. S. Posner, *Biological Calcification: Cellular and Molecular Aspects*, ed. H. Schraer, Springer US, New York, 1970, ch. 1, pp. 1-26.
9. C. C. Ribeiro, I. Gibson and M. A. Barbosa, *Biomaterials* **2006**, *27*, 1749.
10. T. J. Webster, E. A. Massa-Schlueter, J. L. Smith and E. B. Slamovich, *Biomaterials* **2004**, *25*, 2111.
11. J. F. Cawthray, A. L. Creagh, C. A. Haynes and C. Orvig, *Inorg. Chem.* **2015**, *54*, 1440.
12. S. P. Fricker, *Chem. Soc. Rev.* **2006**, *35*, 524.
13. D. G. Karraker, *J. Chem. Educ.* **1970**, *47*, 424.

14. L. I. Ardanova, E. I. Get'man, S. N. Loboda, V. V. Prisedsky, T. V. Tkachenko, V. I. Marchenko, V. P. Antonovich, N. A. Chivireva, K. A. Chebishev and A. S. Lyashenko, *Inorg. Chem.* **2010**, *49*, 10687.
15. G. J. Behets, S. C. Verberckmoes, L. Oste, A. R. Bervoets, M. Salomé, A. G. Cox, J. Denton, M. E. De Broe and P. C. D'Haese, *Kidney Int.* **2005**, *67*, 1830.
16. C. Vidaud, D. Bourgeois and D. Meyer, *Chem. Res. Toxicol.* **2012**, *25*, 1161.
17. H. L. Abrams, R. Spiro and N. Goldstein, *Cancer* **1950**, *3*, 74.
18. R. E. Coleman, *Cancer Treat. Rev.* **2001**, *27*, 165.
19. W. F. Goeckeler, B. Edwards, W. A. Volkert, R. A. Holmes, J. Simon and D. Wilson, *J. Nucl. Med.* **1987**, *28*, 495.
20. W. F. Goeckeler, D. E. Troutner, W. A. Volkert, B. Edwards, J. Simon and D. Wilson, *Nucl. Med. Biol.* **1986**, *13*, 479.
21. J. F. Eary, C. Collins, M. Stabin, C. Vernon, S. Petersdorf, M. Baker, S. Hartnett, S. Ferency, S. J. Addison, F. Applebaum and E. E. Gordon, *J. Nucl. Med.* **1993**, *34*, 1031.
22. I. G. Finlay, M. D. Mason and M. Shelley, *Lancet Oncol.* **2005**, *6*, 392.
23. Y. Yang, M. J. Pushie, D. L. Cooper and M. R. Doschak, *Mol. Pharmaceutics* **2015**, *12*, 4108.
24. S. Nilsson, R. H. Larsen, S. D. Fosså, L. Balteskard, K. W. Borch, J.-E. Westlin, G. Salberg and Ø. S. Bruland, *Clin. Cancer Res.* **2005**, *11*, 4451.
25. P. M. Anderson, V. Subbiah and E. Rohren, in *Current Advances in Osteosarcoma*, ed. E. S. Kleinerman, Springer International, Switzerland, 2014, vol. 804, part IV ch. 3, pp. 291-304.

26. C. Parker, S. Nilsson, D. Heinrich, S. I. Helle, J. M. O'Sullivan, S. D. Fosså, A. Chodacki, P. Wiechno, J. Logue, M. Seke, A. Widmark, D. C. Johannessen, P. Hoskin, D. Bottomley, N. D. James, A. Solberg, I. Syndikus, J. Kliment, S. Wedel, S. Boehmer, M. Dall'Oglio, L. Franzén, R. Coleman, N. J. Vogelzang, C. G. O'Bryan-Tear, K. Staudacher, J. Garcia-Vargas, M. Shan, Ø. S. Bruland and O. Sartor, *N. Engl. J. Med.* **2013**, *369*, 213.
27. O. K. Hjelstuen, *Analyst.* **1995**, *120*, 863.
28. F. D. C. Guerra, A. A. S. Tavares and J. M. R. S. Tavares, *Med. Phys.* **2014**, *41*, 114101.
29. Osteoporosis Canada: Osteoporosis Facts and Statistics, <http://www.osteoporosis.ca/> (accessed February 18, 2016); National Osteoporosis Foundation: What is Osteoporosis, <http://nof.org/articles/7> (accessed March 23, 2016).
30. S. L. Kates, O. S. Kates, D. A. Mendelson, *Injury* **2007**, *38*, 17.
31. R. Rizzoli, H. Bischoff-Ferrari, B. Dawson-Hughes and C. Weaver, *Women's Health* **2014**, *10*, 599.
32. P. Sambrook, Osteoporosis B. Pathology and Pathophysiology, in *Primer on the Rheumatic Diseases*, eds. J. H. Klippel, J. H. Stone, L. J. Crofford and P. H. White, Springer, New York, 2008, pp. 584-586.
33. D. Greenblatt, *Pharmacotherapy* **2005**, *25*, 574.
34. F. Grodstein, M. J. Stampfer, G. A. Colditz, W. C. Willett, J. E. Manson, M. Joffe, B. Rosner, C. Fuchs, S. E. Hankinson, D. J. Hunter, C. H. Hennekens and F. E. Speizer, *N. Engl. J. Med.* **1997**, *336*, 1769.
35. S. Zhang, G. Gangal and H. Uludağ, *Chem. Soc. Rev.* **2007**, *36*, 507.
36. H. L. Benford, J. C. Frith, S. Auriola, J. Mönkkönen and M. J. Rogers, *Mol. Pharmacol.* **1999**, *56*, 131.

37. Osteoporosis Canada: Bisphosphonates, <http://www.osteoporosis.ca/osteoporosis-and-you/drug-treatments/bisphosphonates/> (accessed March 5, 2016).
38. M. R. McClung, *Endocrinol. Metab. Clin. N. Am.* **2003**, *32*, 253.
39. M. J. Favus, *N. Engl. J. Med.* **2010**, *363*, 2027.
40. K. A. Kennel and M. T. Drake, *Mayo Clin. Proc.* **2009**, *84*, 632.
41. M. Whitaker, J. Guo, T. Kehoe and G. Benson, *N. Engl. J. Med.* **2012**, *366*, 2048.
42. W. Querido, A. L. Rossi and M. Farina, *Micron* **2016**, *80*, 122.
43. B. Abrahamsen, E. L. Grove and P. Vestergaard, *Osteoporos. Int.* **2014**, *25*, 757.
44. F. Drago, L. Cogorno, F. Broccolo, G. Ciccarese and A. Parodi, *Osteoporos. Int.* **2016**, *27*, 1261.
45. P. Musette, J.-M. Kaufman, R. Rizzoli, P. Cacoub, M. L. Brandi and J.-Y. Reginster, *Ther. Adv. Musculoskel. Dis.* **2011**, *3*, 31.
46. S. J. P. Damment and I. Webster, *J. Am. Soc. Nephrol.* **2003**, *14*, 204A.
47. M. Pennick, K. Dennis and S. J. P. Damment, *J. Clin. Pharmacol.* **2006**, *47*, 738.
48. G. Block, *Semin. Dial.* **2002**, *15*, 315.
49. E. Slatopolsky, C. Weerts, S. Lopez-Hilker, K. Norwood, M. Zink, D. Windus and J. Delmez, *N. Engl. J. Med.* **1986**, *315*, 157.
50. P. C. D'Haese, G. B. Spasovski, A. Sikole, A. Hutchison, T. J. Freemont, S. Sulkova, C. Swanepoel, S. Pejanovic, L. Djukanovic, A. Balducci, G. Coen, W. Sulowicz, A. Ferreira, A. Torres, S. Curic, M. Popovic, N. Dimkovic and M. E. De Broe, *Kidney Int.* **2003**, *63*, S73.
51. F. Fernandez-Gavarron, T. Huque, J. L. Rabinowitz and J. G. Brand, *Bone Miner.* **1988**, *3*, 283.

52. N. D. Atherton, J. W. Totten and M. D. Gaitonde, WO Pat., WO2002000227 A2, 2002.
53. G. J. Behets, G. Dams, S. R. Varcouteren, S. J. Damment, R. Bouillon, M. E. De Broe and P. C. D'Haese, *J. Am. Soc. Nephrol.* **2004**, *15*, 2219.
54. X. Wang, L. Yuan, J. Huang, T.-L. Zhang and K. Wang, *J. Cell. Biochem.* **2008**, *105*, 1307.
55. Y. L. Shi, L. W. Wang, J. Huang, B. D. Gou, T.-L. Zhang and K. Wang, *J. Cell. Biochem.* **2009**, *108*, 1184.
56. Z. Dawei, Z. Jinchao, C. Yao, Y. Mengsu and Y. Xinsheng, *Prog. Nat. Sci.* **2007**, *17*, 618.
57. U.S. Food and Drug Administration: Drug Approval Package for Fosrenol (Lanthanum Carbonate) Tablets (Administrative Document(s) and Correspondence), http://www.accessdata.fda.gov/drugsatfda_docs/nda/2004/21-468_Fosrenol.cfm (accessed March 11, 2016).
58. S. J. von Resenberg and U. A. Wehr, *J. Anim. Physiol. Anim. Nutr.* **2012**, *96*, 855.
59. Drugs.com: Fosrenol Side Effects, <http://www.drugs.com/sfx/fosrenol-side-effects.html> (accessed March 11, 2016).
60. S. P. Fricker, *Dalton Trans.* **2007**, 4903.
61. C. M. Giandomenico, M. J. Abrams, B. A. Murrer, J. F. Vollano, M. I. Rheinheimer, S. B. Wyer, G. E. Bossard and J. D. Higgins III, *Inorg. Chem.* **1995**, *34*, 1015.
62. S. M. Meier, M. Hanif, Z. Adhireksan, V. Pichler, M. Novak, E. Jirkovsky, M. A. Jakupec, V. B. Arion, C. A. Davey, B. K. Keppler and C. G. Hartinger, *Chem. Sci.* **2013**, *4*, 1837.
63. K. H. Thompson, J. Lichter, C. LeBel, M. C. Scaife, J. H. McNeill and C. Orvig, *J. Inorg. Biochem.* **2009**, *103*, 554.

64. C. A. Lipinski, F. Lombardo, B. W. Dominy and P. J. Feeney, *Adv. Drug Deliv. Rev.* **2001**, *46*, 3.
65. M.-Q. Zhang and B. Wilkinson, *Curr. Opin. Biotechnol.* **2007**, *18*, 478.
66. F.-Y. Chen, Z.-J. Gu, J.-W. Yi, X. Xu, P. Kulkarni and Q. Tang, *New J. Chem.* **2016**, *40*, 2644.
67. C. A. Barta, K. Sachs-Barrable, J. Jia, K. H. Thompson, K. M. Wasan and C. Orvig, *Dalton Trans.* **2007**, 5019.
68. L. Xu, S. J. Rettig and C. Orvig, *Inorg. Chem.* **2001**, *40*, 3734.
69. Y. Mawani, J. F. Cawthray, S. Chang, K. Sachs-Barrable, D. M. Weekes, K. M. Wasan and C. Orvig, *Dalton Trans.* **2013**, *42*, 5999.
70. K. H. Thompson, C. A. Barta and C. Orvig, *Chem. Soc. Rev.* **2006**, *35*, 545.
71. R. A. Yokel, *Coord. Chem. Rev.* **2002**, *228*, 97.
72. M. A. Santos, M. Gil, L. Gano and S. Chaves, *J. Biol. Inorg. Chem.* **2005**, *10*, 564.
73. S. M. Cohen, J. Xu, E. Radkov and K. N. Raymond, *Inorg. Chem.* **2000**, *39*, 5747; D. M. J. Doble, M. Melchior, B. O'Sullivan, C. Siering, J. Xu, V. C. Pierre and K. N. Raymond, *Inorg. Chem.* **2003**, *42*, 4930.
74. C. C. Bisi, *J. Inorg. Nucl. Chem.* **1970**, *32*, 2899; N. K. Dutt and U. U. M. Sarma, *J. Inorg. Nucl. Chem.* **1975**, *37*, 1801; S. Ahmed, J. Burgess, B. Hurman and S. A. Parsons, *Polyhedron* **1994**, *13*, 23; V. Monga, B. O. Patrick and C. Orvig, *Inorg. Chem.* **2005**, *44*, 2666.
75. J. E. Ladbury and B. Z. Chowdhry, *Chem. Biol.* **1996**, *3*, 791.
76. I. Jelesarov and H. R. Bosshard, *J. Mol. Recognit.* **1999**, *12*, 3.
77. W. O. Nelson, T. B. Karpishin, S. J. Rettig and C. Orvig, *Inorg. Chem.* **1988**, *27*, 1045.

78. V. Monga, B. O. Patrick and C. Orvig, *Inorg. Chem.* **2005**, *44*, 2666.
79. B. L. Ellis, A. K. Duhme, R. C. Hider, M. Bilayet Hossain, S. Rizvi and D. van der Helm, *J. Med. Chem.* **1996**, *39*, 3659.
80. A. Datta and K. N. Raymond, *Acc. Chem. Res.* **2009**, *42*, 938.
81. S. Mukherjee, C. Huang, F. Guerra, K. Wang and E. Oldfield, *J. Am. Chem. Soc.* **2009**, *131*, 8374.
82. RSC Periodic Table: <http://www.rsc.org/periodic-table> (accessed May 11, 2016).
83. P. Dulski, *Fresenius J. Anal. Chem.* **1994**, *350*, 194.
84. S. J. P. Damment and M. Pennick, *Toxicol. Lett.* **2007**, *171*, 69; S. J. P. Damment and M. Pennick, *Clin. Pharmacokinet.* **2008**, *47*, 553.
85. M. J. Pushie, I. J. Pickering, M. Korbas, M. J. Hackett and G. N. George, *Chem. Rev.* **2014**, *114*, 8499.
86. J. Anné, N. P. Edwards, R. A. Wogelius, A. R. Tumarkin-Deratzian, W. I. Sellers, A. van Veelen, U. Bergmann, D. Sokaras, R. Alonso-Mori, K. Ignatyev, V. M. Egerton and P. L. Manning, *J. R. Soc. Interface* **2014**, *11*, 20140277.
87. F. Peyrin, *Osteoporos. Int.* **2009**, *20*, 1057
88. J. Huang, T.-L. Zhang, S.-J. Xu, R.-C. Li, K. Wang, J. Zhang and Y.-N. Xie, *Calcif. Tissue Int.* **2006**, *78*, 241.
89. E. W. Price and C. Orvig, *Chem. Soc. Rev.* **2014**, *43*, 260.
90. E. Boros, C. L. Ferreira, J. F. Cawthray, E. W. Price, B. O. Patrick, D. W. Wester, M. J. Adam and C. Orvig, *J. Am. Chem. Soc.* **2010**, *132*, 15726.
91. C. F. Ramogida, J. Pan, C. L. Ferreira, B. O. Patrick, K. Rebullar, D. T. T. Yap, K.-S. Lin, M. J. Adam and C. Orvig, *Inorg. Chem.* **2015**, *54*, 4953.

92. E. Boros, C. L. Ferreira, B. O. Patrick, M. J. Adam and C. Orvig, *Nucl. Med. Biol.* **2011**, 38, 1165.
93. E. Boros, C. L. Ferreira, D. T. T. Yap, R. K. Gill, E. W. Price, M. J. Adam and C. Orvig, *Nucl. Med. Biol.* **2012**, 39, 785.
94. E. W. Price, B. M. Zeglis, J. F. Cawthray, C. F. Ramogida, N. Ramos, J. S. Lewis, M. J. Adam and C. Orvig, *J. Am. Chem. Soc.* **2013**, 34, 12707; E. W. Price, J. F. Cawthray, M. J. Adam and C. Orvig, *Dalton Trans.* **2014**, 43, 7176.
95. G. A. Bailey, E. W. Price, B. M. Zeglis, C. L. Ferreira, E. Boros, M. J. Lacasse, B. O. Patrick, J. S. Lewis, M. J. Adam and C. Orvig, *Inorg. Chem.* **2012**, 51, 12575.
96. E. W. Price, B. M. Zeglis, J. S. Lewis, M. J. Adam and C. Orvig, *Dalton Trans.* **2014**, 43, 119.
97. E. Boros, Y.-H. S. Lin, C. L. Ferreira, B. O. Patrick, U. O. Häfeli, M. J. Adam and C. Orvig, *Dalton Trans.* **2011**, 40, 6253.
98. A. M. Nonat, P. H. Fries, J. Pécaut and M. Mazzanti, *Chem. Eur. J.* **2007**, 13, 8489.
99. A. M. Nonat, C. Gateau, P. H. Fries, L. Helm and M. Mazzanti, *Eur. J. Inorg. Chem.* **2012**, 2049.
100. C. Marchal, Y. Filinchuk, D. Imbert, J.-C. G. Bünzli and M. Mazzanti, *Inorg. Chem.* **2007**, 46, 6242.
101. E. V. Mateeva, P. V. Petrovskii and I. L. Odinet, *Tetrahedron Lett.* **2008**, 49, 6129.
102. V. Kubiček, J. Kotek, P. Hermann and I. Lukeš, *Eur. J. Inorg. Chem.* **2007**, 333.
103. R. Torres Martin de Rosales, C. Finucane, S. J. Mather and P. J. Blower, *Chem. Commun.* **2009**, 4847.
104. R. D. Ross, L. E. Cole and R. K. Roeder, *J. Nanopart. Res.* **2012**, 14, 1175.

105. G. Rodan, A. Reszka, E. Golub, R. Rizzoli, *Curr. Med. Res. Opin.* **2004**, 20(8).
106. P. van der Sluis and A. L. Spek, *Acta Cryst.* **1990**, A46, 194.
107. G. E. Moore, J. Xu, C. J. Jocher, E. J. Werner and K. N. Raymond, *J. Am. Chem. Soc.* **2006**, 128, 10648.
108. C.-H. Huang and Z. Bian, in *Rare Earth Coordination Chemistry: Fundamentals and Applications*, ed. C.-H. Huang, John Wiley & Sons, New York, 2011, ch. 1, pp. 19-20.
109. P. H. Smith, Z. E. Reyes, C.-W. Lee and K. N. Raymond, *Inorg. Chem.* **1988**, 27, 4154.
110. C. Paul-Roth and K. N. Raymond, *Inorg. Chem.* **1994**, 34, 1408.
111. HyperQuad2013: Equilibrium Constants from Potentiometric Data, <http://www.hyperquad.co.uk/HQ2013.htm> (Accessed May 17, 2016).
112. A. K. Covington, M. Paabo, R. A. Robinson and R. G. Bates, *Anal. Chem.* **1968**, 40, 700.
113. L. Alderighi, P. Gans, A. Ienco, D. Peters, A. Sabatini and A. Vacca, *Coord. Chem. Rev.* **1999**, 184, 311.
114. OECD Test 107: Partition Coefficient (n-octanol/water): Shake Flask Method, in *OECD Guidelines for the Testing of Chemicals; Section 1: Physical-Chemical Properties*, OECD publishing, 1995, pp. 1-4.
115. G. Ananchenko, J. Novakovic and A. Tikhomirova, in *Profiles of Drug Substances, Excipients and Related Methodology*, ed. H. G. Brittain, Academic Press, San Diego, 2013, 1st edn, vol. 38, ch. 1, p. 5.
116. A recipe calculator for thermodynamically correct buffers for pH control, <https://www.liverpool.ac.uk/buffers/buffercalc.html> (Accessed April 28, 2016).
117. P. Gans and B. O'Sullivan, *Talanta* **2000**, 51, 33.
118. F. Rossotti and H. Rossotti, *J. Chem. Educ.* **1965**, 42, 375.

119. A. E. Koenig, R. R. Rogers and C. N. Trueman, *Geology* **2009**, *37*, 511.
120. D. J. Bellis, K. M. Hetter, J. Jones, D. Amarasiriwardena and P. J. Parsons, *J. Anal. Spectrom.* **2006**, *21*, 948.
121. USGS: New Reference Materials in Production, http://crustal.usgs.gov/geochemical_reference_standards/RM_development.html (Accessed May 3, 2016).
122. D. Lajeunesse, C. Frondoza, B. Schoffield and B. Sacktor, *J. Bone Miner. Res.* **1990**, *5*, 915.
123. J. Clover and M. Gowen, *Bone* **1994**, *15*, 585.
124. A. Gartland, R. M. Rumney, J. P. Dillon and J. A. Gallagher, *Methods Mol. Biol.* **2012**, *806*, 337.
125. E. W. Bradley and M. J. Oursler, *Methods Mol. Biol.* **2008**, *455*, 19.
126. P. Artursson and J. Karlsson, *Biochem. Biophys. Res. Commun.* **1991**, *175*, 880.
127. I. Lukeš, J. Kotek, P. Voktíšek and P. Hermann, *Coord. Chem. Rev.* **2001**, *216*, 287.
128. J. Galezowska and E. Gumienna-Kontecka, *Coord. Chem. Rev.* **2012**, *256*, 105.
129. G. Subramanian, J. G. MacAfee (Research Corporation). US Pat. 4017595 A, April 12, 1977.
130. J. Galezowska, R. Janicki, A. Mondry, R. Burgada, T. Bailly, M. Lecouvey and H. Kozłowski, *Dalton Trans.* **2006**, 4384.

Appendices

^1H NMR spectra for Hdpp and H₅XT

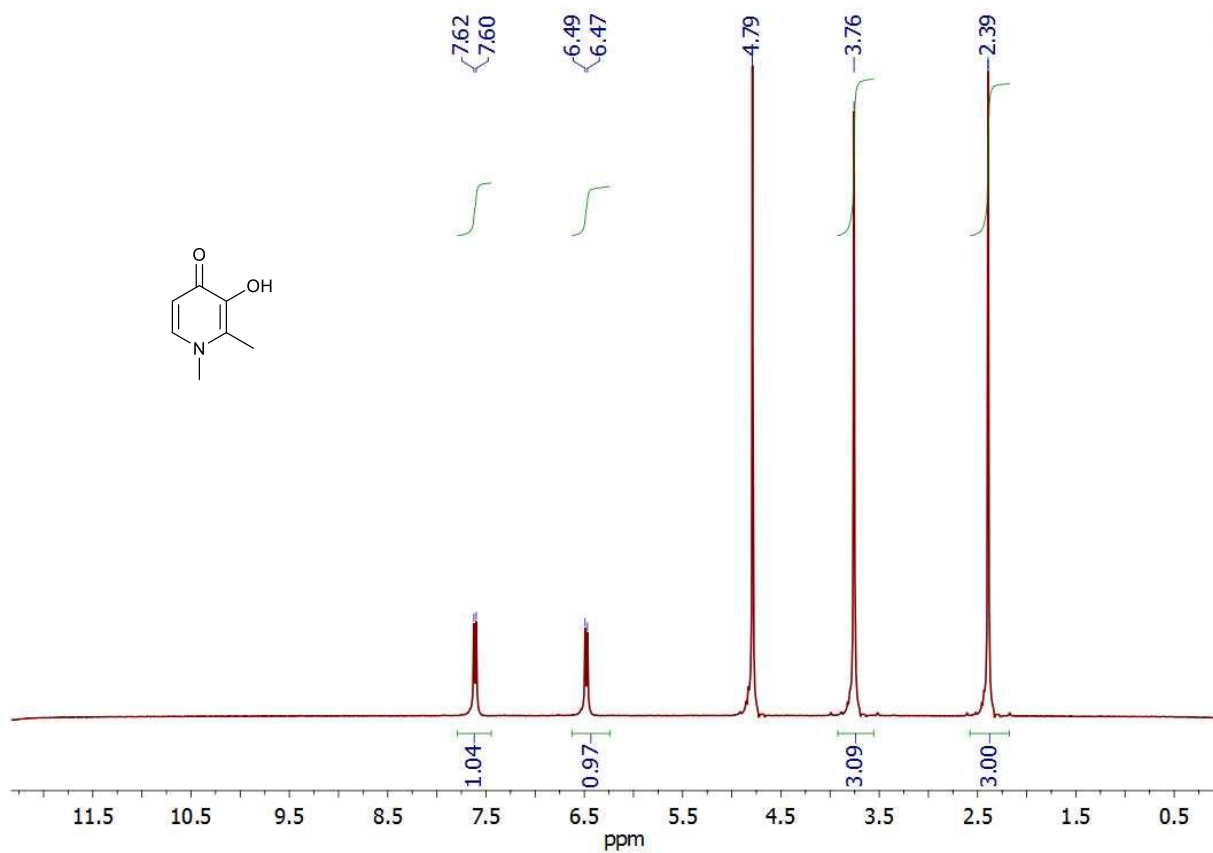


Figure A.1 ^1H NMR spectrum for Hdpp (D_2O , 298 K, 300 MHz).

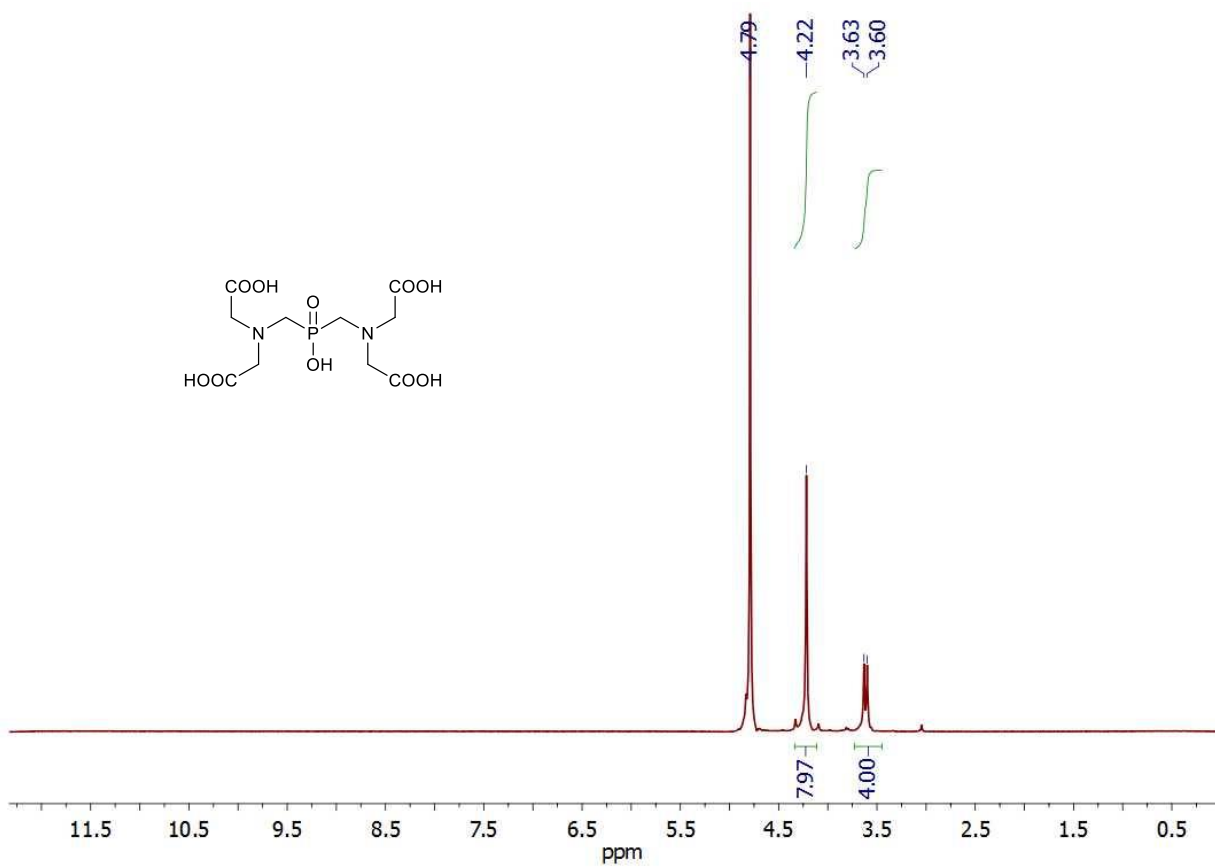
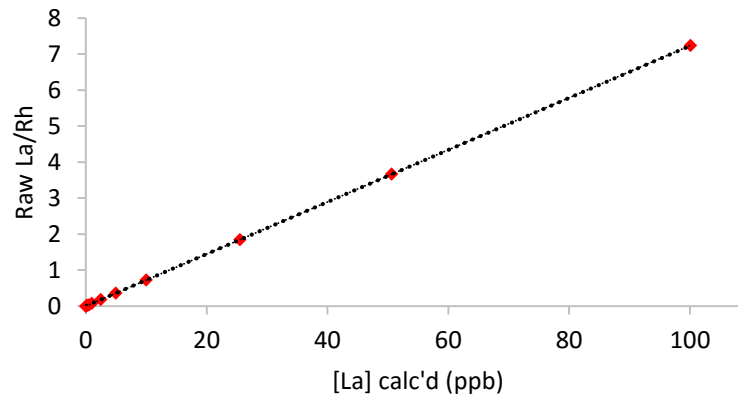


Figure A.2 ¹H NMR spectrum for H₅XT (D₂O, 298 K, 300 MHz).

Lanthanum ICP-MS calibration plot



Element	Mass	R ²	Rh ratio	Blank	DL	BEC	Units
La	139	0.999989	0.723236	0.003441	0.000593	0.004759	ppb

Figure A.3 A typical ICP-MS calibration plot for lanthanum with 10 ppb rhodium as an internal standard.

X-ray crystal structures of dipicolinic acid ligands

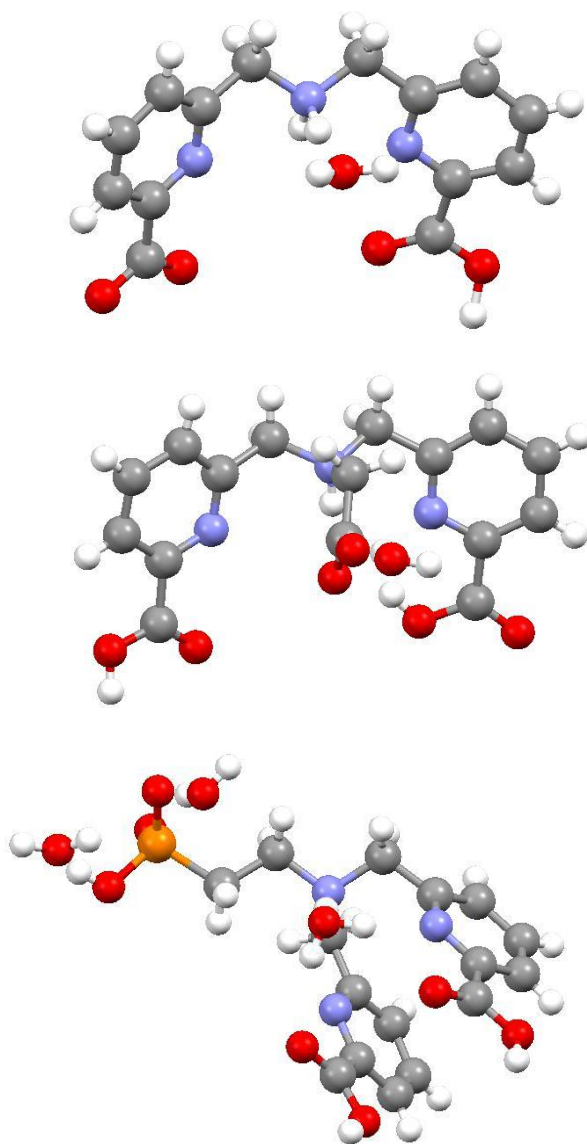


Figure A.4 Solid-state X-ray structures for crystals of H₂dpa·H₂O, obtained by Dr. Lisa Murphy (upper), of H₃cedpa·H₂O, obtained by Dr. Caterina Ramogida (middle), and of H₄pedpa·3H₂O (lower). All measurements were made on a Bruker X8 APEX II diffractometer, and the data were collected and integrated using Bruker SAINT software. The structures were solved by Dr. Brian Patrick by direct methods. All non-hydrogen atoms were refined anisotropically. All N-H and O-H hydrogen atoms were located in difference maps and refined isotropically. All other hydrogen atoms were placed in calculated positions. Crystallographic data is presented in Table A.1.

Table A.1 Crystallographic data.

	H₂dpa·H₂O	H₃cedpa·H₂O	H₄pedpa·3H₂O
Formula	C ₁₄ H ₁₅ N ₃ O ₅	C ₁₆ H ₁₇ N ₃ O ₇	C ₁₆ H ₂₄ N ₃ O ₁₀ P
Formula weight	305.29	363.32	449.35
Crystal system	Triclinic	Monoclinic	Monoclinic
Space group	<i>P</i> -1 (#2)	<i>P</i> 2 _{1/n} (#14)	<i>P</i> 2 _{1/n} (#14)
Lattice type	Primitive	Primitive	Primitive
Lattice parameters	<i>a</i> = 7.361(1) Å <i>b</i> = 12.812(2) Å <i>c</i> = 15.475(2) Å <i>α</i> = 73.422(7)° <i>β</i> = 89.813(8)° <i>γ</i> = 81.366(9)°	<i>a</i> = 8.0530(6) Å <i>b</i> = 13.8608(10) Å <i>c</i> = 13.8522(11) Å <i>α</i> = 90° <i>β</i> = 93.471(2)° <i>γ</i> = 90°	<i>a</i> = 7.1253(7) Å <i>b</i> = 21.309(2) Å <i>c</i> = 13.744(1) Å <i>α</i> = 90° <i>β</i> = 103.853(3)° <i>γ</i> = 90°
Lattice volume	1381.8(3) Å ³	1543.4(2) Å ³	2026.2(3) Å ³
<i>Z</i>	4	4	4
<i>D</i> _{calc'd}	1.467 g/cm ³	1.564 g/cm ³	1.473 g/cm ³
<i>F</i> (000)	640.00	760.00	944.00
<i>μ</i> (MoK α)	1.13 cm ⁻¹	1.25 cm ⁻¹	1.96 cm ⁻¹
Reflections collected	20108	21149	29364
Unique reflections	5001	4522	5480
Reflections with <i>I</i> ≥ 2.00σ(<i>I</i>)	3504	4025	4305
R _{int} ; R ₁ ; wR ₂	0.074; 0.112; 0.211	0.026; 0.040; 0.098	0.035; 0.040; 0.092
GofF on <i>F</i> ²	1.04	1.05	1.02

^1H NMR spectra for H_2dpa and $\text{La}(\text{dpa})$

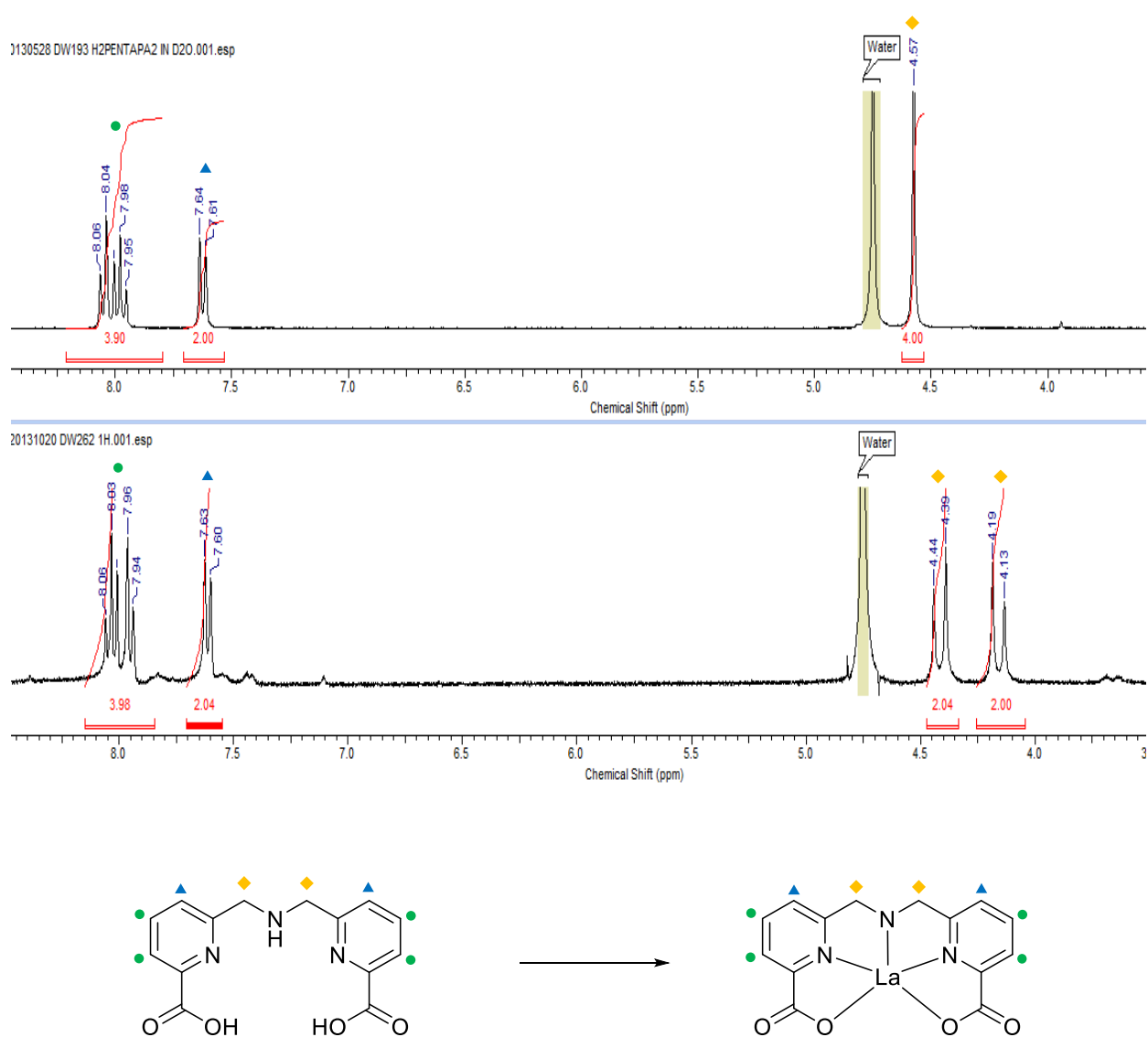


Figure A.5 ^1H NMR spectra for H_2dpa (upper) and $\text{La}(\text{dpa})$ (lower) in D_2O (300 MHz) at ambient temperature.

^1H NMR spectra for H_3cedpa and $\text{La}(\text{cedpa})$

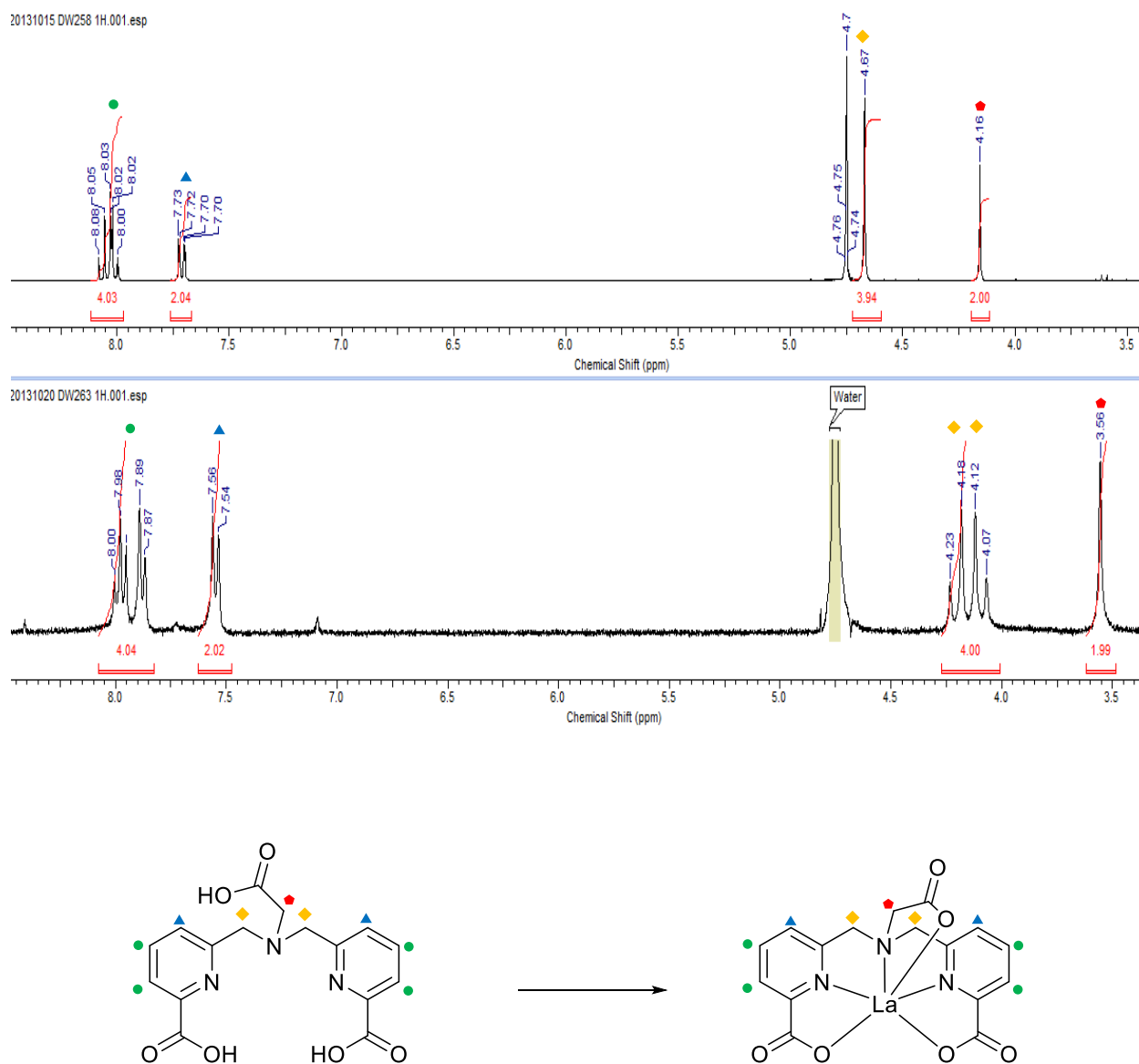


Figure A.6 ^1H NMR spectra for H_3cedpa (upper) and $\text{La}(\text{cedpa})$ (lower) in D_2O (300 MHz) at ambient temperature.

^1H NMR spectra for H_4pedpa and $\text{La}(\text{pedpa})^-$

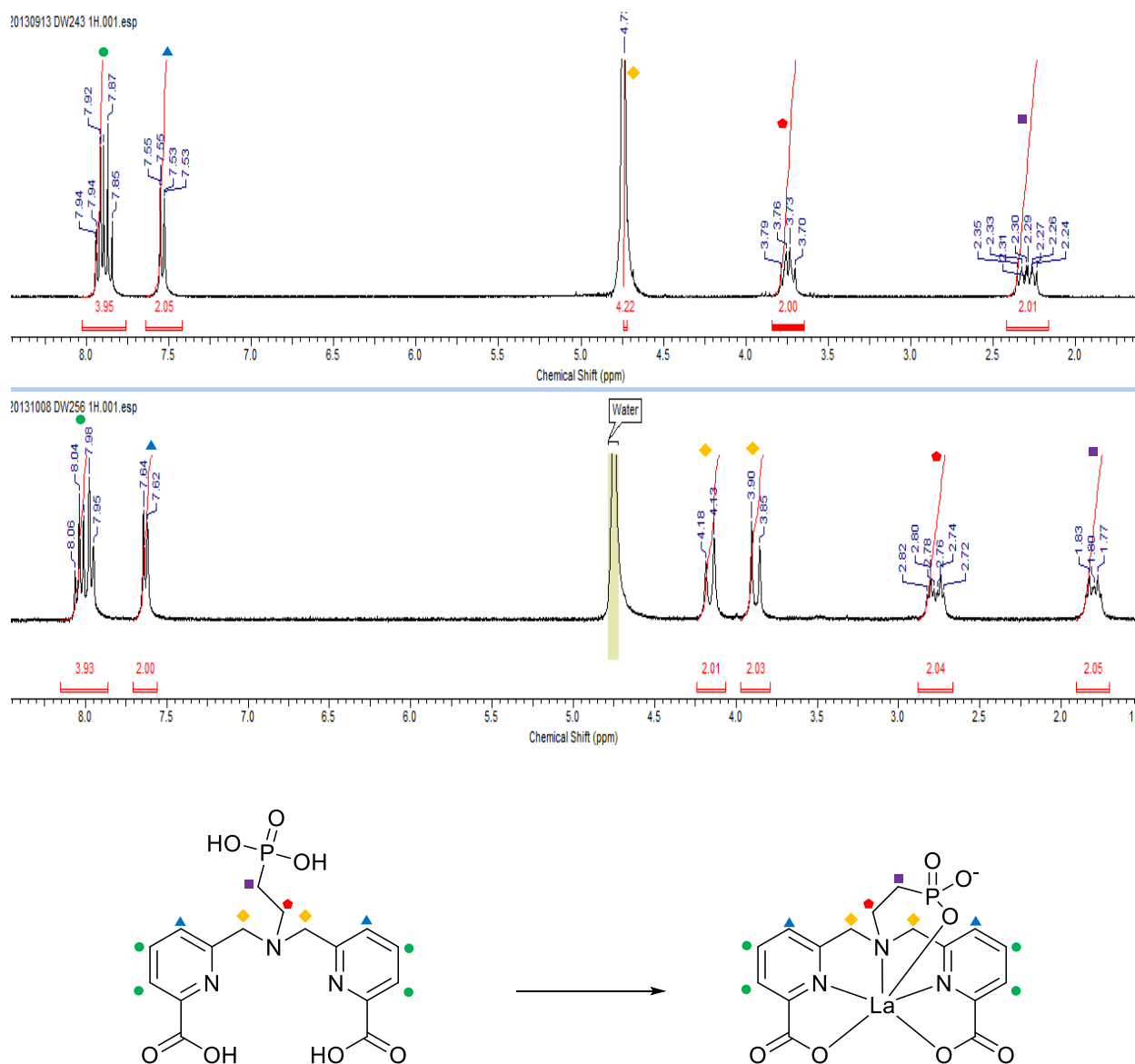


Figure A.7 ^1H NMR spectra for H_3pedpa (upper) and $\text{La}(\text{pedpa})^-$ (lower) in D_2O (300 MHz) at ambient temperature.

H₄pedpa pH-dependent ³¹P{¹H} NMR spectra

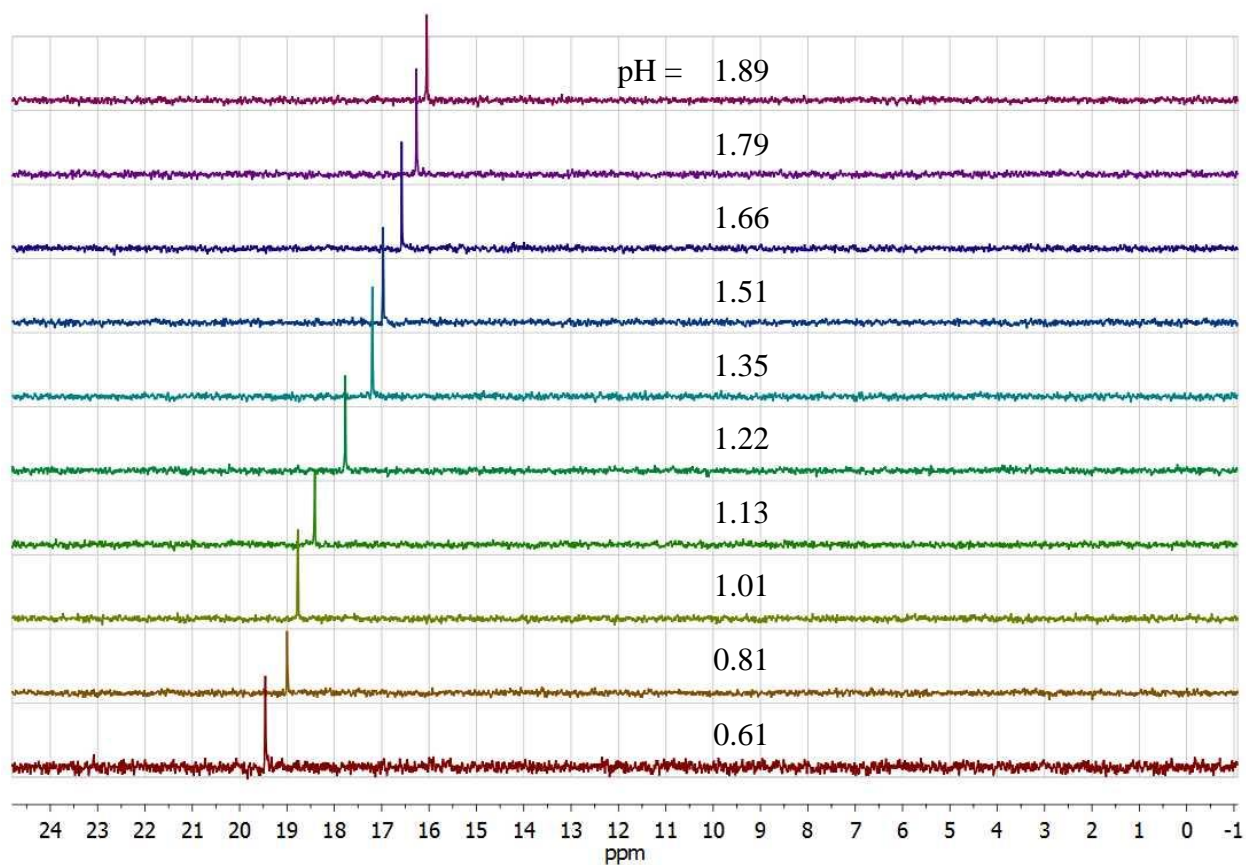


Figure A.8 The ³¹P{¹H} NMR spectra (298 K, 162 MHz) for H₄pedpa recorded at various pH levels and used to calculate the first p*K*_a for the compound (Figure 4.10) using the HypeNMR2008 and Hyss programs.¹¹³

^1H NMR spectrum for $\text{La}(\text{dpa})_2$

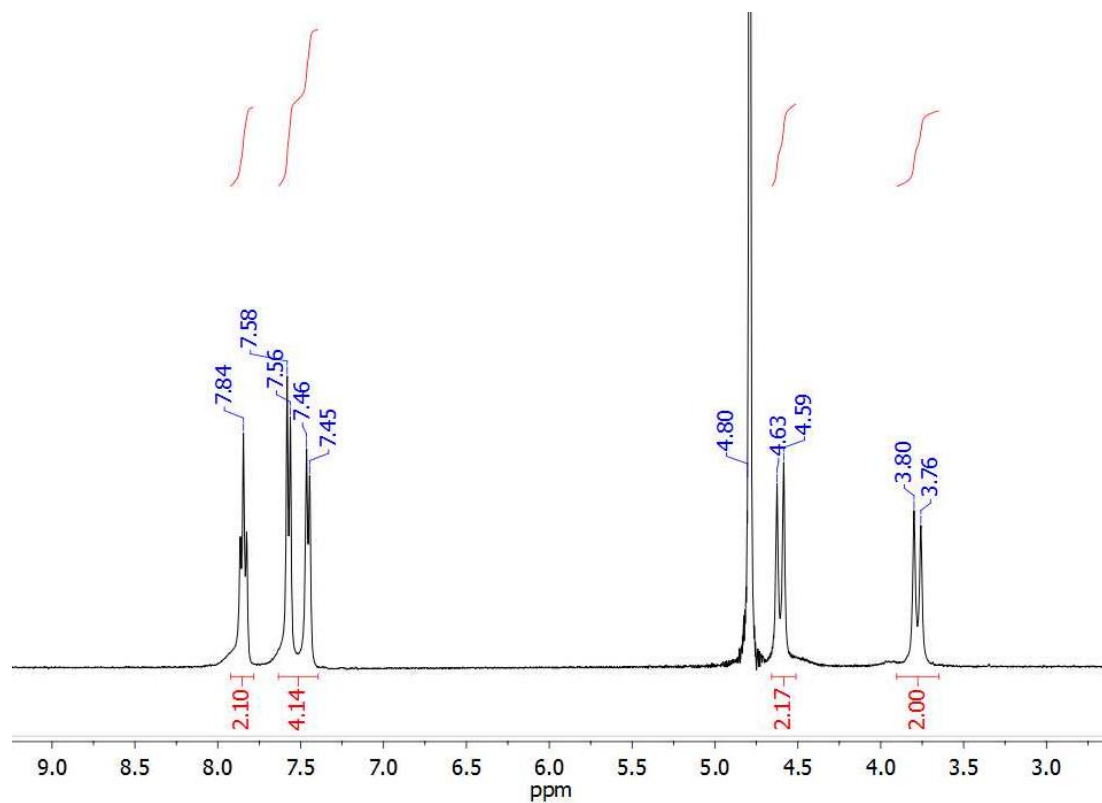


Figure A.9 ^1H NMR spectrum of a 2:1 mixture dpa:La in D_2O at pH 12.3 (400 MHz) at 298 K.

Molar extinction coefficients of dpa ligands and La complexes

Table A.2 Experimentally measured molar extinction coefficients (ϵ) and absorbance maxima (λ_{\max}) for all compounds for which concentration was determined by UV-Vis. Measurements were performed at ambient temperature in a background solution of HEPES buffer (50 mM, $I = 0.16$ M) at a path length of 1 cm.

Ligand or complex	λ_{\max} (nm)	ϵ (mM ⁻¹ cm ⁻¹)
H ₂ dpa	268	8.5624
H ₃ cedpa	269	8.0905
H ₄ pedpa	270	7.3095
H ₇ alenpa	270	7.7079
La(dpa)	272	6.1436
La(cedpa)	272	5.8198
La(pedpa)	272	6.0723